Elements of AlGaN-Based Light Emitters

Martin Stattin

Photonics Laboratory
Department of Microtechnology and Nanoscience (MC2)
Chalmers University of Technology
Göteborg, Sweden, 2013

Elements of AlGaN-Based Light Emitters

Martin Stattin

Göteborg, April 2013

Photonics Laboratory
Department of Microtechnology and Nanoscience (MC2)
Chalmers University of Technology, SE-412 96 Göteborg, Sweden
Phone: +46 (0) 31 772 1000

Front cover illustration: Two of the three different AlGaN-based light emitters that are the topic of this thesis. Above left: A blue vertical cavity surface emitting laser. Below right: A near-infrared quantum cascade laser.

Elements of AlGaN-Based Light Emitters

Martin Stattin

Photonics Laboratory

Department of Microtechnology and Nanoscience (MC2)

Chalmers University of Technology, SE-412 96 Göteborg, Sweden

Abstract

The III-nitrides have enabled a range of optoelectronic devices and associated applications of great industrial and societal importance. However, the full potential of the III-nitrides remains to be explored. In this thesis, different important elements of AlGaN-based light emitters have been developed to allow for improvements of deep-ultraviolet (DUV) light emitting diodes (LEDs), blue vertical cavity surface emitting lasers (VCSELs), and near-infrared (NIR) quantum cascade lasers (QCLs).

AlGaN is unique among the wide-bandgap semiconductors in that both p- and n-type conductivity can be achieved. However, effective p-type doping remains difficult, in particular for high-Al content AlGaN. Here we report on progress towards lower resistivity Mg-doped $Al_{0.85}Ga_{0.15}N$, which will benefit the development of DUV-LEDs. A resistivity of 7 kΩ·cm was achieved. We also report on the use of transferred double layer metal-free graphene as a transparent contact on p-GaN for uniform current injection, which could benefit the development of surface emitting LEDs and VCSELs emitting in the blue-green. The graphene transparent contact was shown to momentarily sustain a current density of 1 kA/cm^2, which is close to the threshold current density of state-of-the-art blue VCSELs.

The large conduction band offset of AlN/GaN quantum wells may enable the wavelength range of QCLs to be extend to the NIR, potentially even covering the telecom wavelength of 1550 nm where a QCL could provide e.g. chirp free modulation. A particular challenge for AlGaN-based short wavelength QCLs is the design of a low loss waveguide that also allows for efficient current injection and extraction. We have therefore developed two such waveguide designs, one employing a dielectric cladding and an off-center metal contact in a ridge configuration and a second employing a ridge waveguide with a ZnO upper cladding and an AlN lower cladding for mode confinement, and investigated their performance characteristics. We also show, both experimentally and theoretically, that the temperature dependence of the intersubband transition energy in AlN/GaN QWs designed for short wavelength absorption/emission is very weak (15 μeV/K), which suggests that AlGaN-based telecom QCLs could operate without active temperature control.

Keywords: III-nitride, AlGaN, graphene, light emitting diode, vertical cavity surface emitting laser, quantum cascade laser, deep-ultraviolet, visible, near-infrared

List of Papers

This thesis is based on the following appended papers:

[I] A. Kakanakova-Georgieva, D. Nilsson, **M. Stattin**, U. Forsberg, Å. Haglund, A. Larsson, and E. Janzén, "Mg-doped $Al_{0.85}Ga_{0.15}N$ layers grown by hot-wall MOCVD with low resistivity at room temperature," *Physica Status Solidi RRL*, vol. 4, no. 11, pp. 311-313, Sept. 2010.

[II] K. Berland, **M. Stattin**, R. Farivar, D. M. S. Sultan, P. Hyldgaard, A. Larsson, S. M. Wang, and T. G. Andersson, "Temperature stability of intersubband transitions in AlN/GaN quantum wells," *Applied Physics Letters*, vol. 97, no. 4, 043507, July 2010.

[III] **M. Stattin**, K. Berland, P. Hyldgaard, A. Larsson, and T. G. Andersson, "Waveguides for nitride based quantum cascade lasers," *Physica Status Solidi C*, vol. 8, no. 7-8, pp. 2357-2359, May 2011, also presented at the *International Workshop on Nitride Semiconductors 2010 (IWN2010)*, Tampa (FL), USA, Poster HP1.15, Sept. 2010.

[IV] **M. Stattin**, J. Bengtsson, and A. Larsson, "ZnO/AlN clad waveguides for AlGaN-based quantum cascade lasers," to appear in *Japanese Journal of Applied Physics*, also presented at the *International Workshop on Nitride Semiconductors 2012 (IWN2012)*, Sapporo, Japan, Poster ThP-OD-35, Oct. 2012.

[V] **M. Stattin**, C. Lockhart de la Rosa, J. Sun, A. Yurgens, and Å. Haglund, "Metal-free graphene as transparent electrode for GaN-based light-emitters," to appear in *Japanese Journal of Applied Physics*, also presented at the *International Workshop on Nitride Semiconductors 2012 (IWN2012)*, Sapporo, Japan, Poster ThP-OD-34, Oct. 2012.

Other publications by the author:

[A] T. Ive, K. Berland, **M. Stattin**, F. Fälth, P. Hyldgaard, A. Larsson, and T. G. Andersson, "Design and fabrication of AlN/GaN heterostructures for intersub-band technology," *Japanese Journal of Applied Physics*, vol. 51, 01AG07, Jan. 2012.

[B] E. Hashemi, J. Gustavsson, J. Bengtsson, **M. Stattin**, G. Cosendey, N. Grand-jean, and Å Haglund, "Engineering the lateral optical guiding in gallium nitride-based vertical-cavity surface-emitting laser cavities to reach the lowest threshold gain," to appear in *Japanese Journal of Applied Physics*.

Acknowledgement

During my time as a PhD-student I have had the privilege to work on three different projects regarding to III-nitride optoelectronics. This has allowed me to collaborate with many talented researchers, and to gain experience in essentially all parts of device fabrication. For letting me do this and for his help and advice on the way I would like to thank my examiner and main supervisor professor Anders Larsson. I would also like to thank my co supervisors Åsa Haglund, for sharing her experience in the cleanroom related aspects of device fabrication, and Tommy Ive, for teaching me about epitaxial growth using molecular beam epitaxy.

From the blue vertical cavity surface emitting laser project apart from my supervisors I would also like to thank the collaborators Ehsan Hashemi, Johan Gustavson and Jörgen Bengtsson. Additionally for their help with graphene/p-GaN contacts I thank Jie Sun, Cesar de la Rosa and August Yurgens, especially Jie and Cesar who grew and transferred the graphene. I would also like to thank Gatien Cosendey in the group of Nicolas Grandjean at EPFL for providing the p-GaN and LED structures used for the transparent contact evaluation.

I would like to thank the deep ultraviolet light-emitter project partners at Linköping University, mainly, Erik Janzén, Annelia Kakanakova-Georgieva, Anne Henry, Urban Forsberg and Daniel Nilsson, for interesting meetings and discussions, especially Daniel who has grown most of the samples deserves thanks. I would also like to express my gratitude to Benjamin Kögel who helped me with some of the cleanroom work.

I would also like to thank the many collaborators in the quantum cascade laser project, mainly, Thorvald G. Andersson, Per Hyldgaard, Shu-Min Wang, Rashid Farivar, Kristian Berland, D. M. S. Sultan, and Fredrik Fält for our many meetings and good discussions. I would especially like to thank the master thesis student Sultan for his help with the measurements for paper II and the PhD-students: Kristian, for his theoretical simulation work and many interesting discussions, and Rashid, for growth and material characterization.

I am also grateful for having had access to excellent cleanroom facilities with knowledgable staff providing excellent tool uptime and support. Also Carl-Magnus

Kihlman, whose metal workshop skills has been instrumental in the construction of my measurement setups, is worthy of thanks.

I also thank the rest of the people at the photonics laboratory for providing a pleasant work environment, especially my fellow PhD-student colleagues in the optoelectronics group for the many stimulating discussions and moral boosting sideline activities. Göran, Carl, Petter, Erik, Huan, Yuxin, David, Tobias and Ehsan I thank you all.

Luckily there has also been times spent away from the lab, for this I would like to thank my non-work friends for many pleasant evenings, dinner parties, skiing and climbing journeys, and generally good times.

Finally I thank my parents, Urban and Agneta, and my sister, Camilla, for an excellent upbringing and for their support and encouragement during my years at Chalmers.

<div align="right">Martin Stattin</div>

Göteborg
April 2013

List of Acronyms

AFM   atomic force microscopy [30, 49, 52]

CAPS   cavity phase-shift [58]

CH   crystal-hole [9]

CMP   chemical mechanical polishing [25]

CTLM   circular transmission line method [53, 54]

CVD   chemical vapor deposition [27, 45]

CW   continous-wave [2, 24, 25, 34, 35, 65]

DBR   distributed Bragg reflector [24, 25, 28–32, 49, 50, 65]

DFB   distributed feedback [39]

DUV   deep ultraviolet [2, 3, 12, 15, 17, 18, 20, 46, 63, 64]

EBL   electron blocking layer [21]

EL   electro-luminescence [18, 35, 66]

EQE   external quantum efficiency [17–21, 63]

FEA   free electron absoption [26, 31, 38]

FP   Fabry-Pérot [58, 60, 62]

FTIR   Fourier transform infrared [58]

FWHM   full width at half maximum [50]

HH   heavy-hole [9, 13]

HVPE   hydride vapor phase epitaxy [12, 19, 42, 63]

IE   injection efficiency [17]

IQE   internal quantum efficiency [17–19, 63]

IR   infrared [5, 33]

ISB   intersubband [33–35, 58, 66, 67]

ITO indium-tin-oxide [11, 26–28, 65]

LD laser diode [1, 2, 6, 12, 13, 15, 17, 19, 23, 26, 30, 32, 34, 35, 63, 64]

LED light emitting diode [1–3, 5, 6, 12, 13, 15–21, 24, 26, 27, 32, 46, 56, 63, 64]

LEE light extraction efficiency [17, 18, 63, 64]

LEEBI low-energy electron-beam irradiation [2]

LH light-hole [9, 13]

LO longitudinal-optical [35]

MBE molecular beam epitaxy [12, 29, 32, 43, 44]

MO metal-organic [43, 44]

MOCVD metal-organic chemical vapor deposition [10–12, 21, 25, 29, 32, 43, 44, 54, 67]

NIR near-infrared [2, 3, 39, 60, 66]

PEC photoelectrochemical [25]

PL photoluminescence [11, 17, 20, 66]

PLD pulsed laser deposition [12]

PVT physical vapor transport [12, 19, 42, 63]

QCL quantum cascade laser [2, 3, 33–37, 39, 66–68]

QW quantum well [1, 2, 5, 9, 13, 18–20, 24, 25, 29, 31, 33–37, 50, 58, 64, 67]

RIE reactive-ion etching [25, 32, 65]

RT room temperature [2, 11, 19, 21, 24, 25, 34, 35, 65]

SEM scanning electron microscopy [29, 30, 49]

SL superlattice [11]

SPSL short period superlattice [25, 29–31, 50]

TCO transparent conductive oxide [24, 26–29, 32, 65]

TDD threading dislocation density [18–20, 63]

TE transverse electric [6, 19]

TEM transmission electron microscopy [18]

TLM transmission line method [53, 56]

TM transverse magnetic [6, 38]

UV ultraviolet [12, 15–18, 44, 63]

VCSEL vertical cavity surface emitting laser [2, 3, 6, 23–27, 29, 32, 56, 65]

WPE wall-plug efficiency [18, 34]

XRD X-ray diffraction [49, 50]

Table of Contents

Chapter 1

Introduction

With the advent of the blue high-brightness GaN-based light emitting diode (LED) merely 20 years ago a new source of light dawned [1], the energy-efficient white LED lamp. Such lamps are currently used to replace the incandescent light bulbs that have to a large extent been outlawed in the European Union [2]. The white light is generated by a blue LED with a yellow emitting phosphor coating. Presently, the Hg containing compact fluorescent lamps are the key competitor to LEDs for energy-efficient illumination. Although Hg-based lamps are cheaper to manufacture they have shorter lifetimes, longer turn-on times and contain hazardous materials (Hg). They are also roughly half as energy efficient compared to a recently announced LED-based lamp capable of over 200 lm/W [3]. Another important application for the III-nitrides are the blue-violet (405 nm) laser diodes (LDs) that have enabled the Blu-ray Disk™ high density optical storage technology.

Currently, there is a large interest in extending the high-efficiency and high-brightness wavelength range, from the blue to both longer and shorter wavelengths. For the longer wavelengths, the motivation is to cover the so called green-gap, where the efficiency is worse than for blue and red LEDs. Efficient green LEDs could be used in combination with blue and red LEDs to create even more efficient white light-emitters, since this avoids energy being lost in the phosphor conversion process currently used. There is also an interest in developing green LDs for use in, e.g., pico-projectors. Green LDs are difficult to manufacture for the same reasons as green LEDs, the reasons being the low In incorporation in InGaN quantum wells (QWs) at conventional growth temperature and increased efficiency droop at longer wavelengths [4].

Similar efficiencies as for blue LEDs have been demonstrated at wavelengths down

to 365 nm, which corresponds to the bandgap of GaN. To reach shorter wavelengths, the InGaN alloys in the QWs are replaced with AlGaN alloys. This, in combination with high dislocation densities reduces efficiency significantly. The shortest wavelength LED that has been demonstrated was an AlN homojunction LED with emission at 210 nm [5]. However, the primary target for the shorter wavelength range is the so-called germicidal wavelength, 265 nm, where efficient long-lifetime LEDs could replace the bulky, toxic, short lived, and fragile Hg-based gas-discharge lamps that are currently used in water purification and disinfection systems. For deep ultraviolet (DUV)-LEDs a power efficiency of 7.8% at 278 nm has been demonstrated [6]. Short wavelength LDs are also of interest, primarily for photo-lithography and photochemical curing. AlGaN-based LDs have reached wavelengths as short as 336 nm [7].

The III-nitrides are also being investigated for use in other device technologies where they have potential to increase the wavelength and operational temperature range from what is possible with other III-V semiconductors. The vertical cavity surface emitting lasers (VCSELs) is one such device topology, where III-nitrides could be used to be used to make inexpensive blue and green lasers with high optical beam quality. Although both blue and green emission has been demonstrated [8], there is still a need for significant development to improve both efficiency and yield. Such lasers could be used in high-resolution printers, read-out-heads for optical data storage and for bio-medical applications.

Quantum cascade lasers (QCLs) could also benefit from the III-nitrides. Currently, mid- and far-infrared QCLs are mainly used for gas and molecular analysis systems. The large conduction band offset and large remote valley separation offered by the III-nitrides could extend the wavelength range into the near-infrared (NIR). Currently, the lower lower limit is 2.6 μm [9]. Possibly, even telecom wavelengths (1.55 μm), could be reached where the QCL could potentially reduce temperature dependence of the emission wavelength and allow chirp-free modulation. The large phonon energy could potentially also allow room temperature (RT) THz QCLs, for use in security imaging systems. To date no III-nitride QCL has been demonstrated.

Work on blue light emitters using GaN was initiated in the 1960s at RCA [10]. After a few years they successfully created blue emitters using metal-insulator-semiconductor structures but were unable to create the p-type GaN needed for efficient LEDs. Even though they were trying the current standard p-dopant Mg already in 1972, the much needed p-GaN remained elusive. It was not until 1989 that p-type GaN was achieved. Then it was discovered that the passive Mg acceptors were activated by low-energy electron-beam irradiation (LEEBI) [11]. Using this method, a pn-junction LED was demonstrated [11]. The LEEBI activation was successful but not really suitable for mass production. In 1992, S. Nakamura at Nichia developed high-temperature annealing as a post growth treatment to activate the Mg acceptors [12]. His work regarding the passivation of the Mg acceptors by H atoms made controlled p-doping possible. At the end of 1993, the first commercial blue GaN LEDs were introduced by Nichia [1]. With continued rapid development of GaN based light emitters, a blue continous-wave (CW) RT LD was manufactured in 1995 [13].

2

In this thesis, different important elements of light emitters in AlGaN-based semi-conductors have been explored to allow for improvements of DUV-LEDs, blue VCSELs, and NIR-QCLs. The outline is as follows. In the next chapter the general properties of AlGaN semiconductors will be discussed. The following chapter is dedicated to the intricacies of DUV emitters. This is followed by a chapter concerning blue VCSELs. Then a chapter focusing on QCLs follows. Some of the methods used for fabricating and characterizing devices are then presented in the aptly named chapters *"Epitaxial Growth and Device Processing Methods"* and *"Characterization Techniques"*. Before presenting the appended papers, an outlook with future prospects for light emitters in III-nitride based materials is given.

Chapter 2

Aluminium Gallium Nitride

The wide bandgap AlGaN material system has properties that make it suitable for many optoelectronic applications. By including InGaN QWs, the energy efficient blue-LEDs that have enabled white light LEDs used for e.g. general illumination. In this chapter the material properties will be described in more detail.

2.1 Optical Properties

Both GaN and AlN have a wide bandgap, corresponding to wavelengths shorter than visible. Bulk crystals are transparent but with a deep amber tint giving them a gemstone like appearance. The tint is due to impurities incorporated during crystal growth.

In Figure 2.1, the bandgap energy, E_g, for the different III-nitride alloys is plotted with respect to the lattice parameter a_0. It can be seen that with sufficient In incorporation, the bandgap can be reduced to cover the whole visible spectrum and even reach into the infrared (IR). Furthermore, the bandgap is direct for all compositions, allowing for efficient light emitters.

The real and imaginary parts of the ordinary refractive index for AlN, GaN and one intermediate alloy are plotted in Figure 2.2 as a function of photon energy. Since AlN, GaN and their alloys are positively uniaxially birefringent [14], they have an extraordinary refractive index that is larger than the ordinary refractive index. Photons with polarization parallel to the optical axis will experience the extraordinary refractive index.
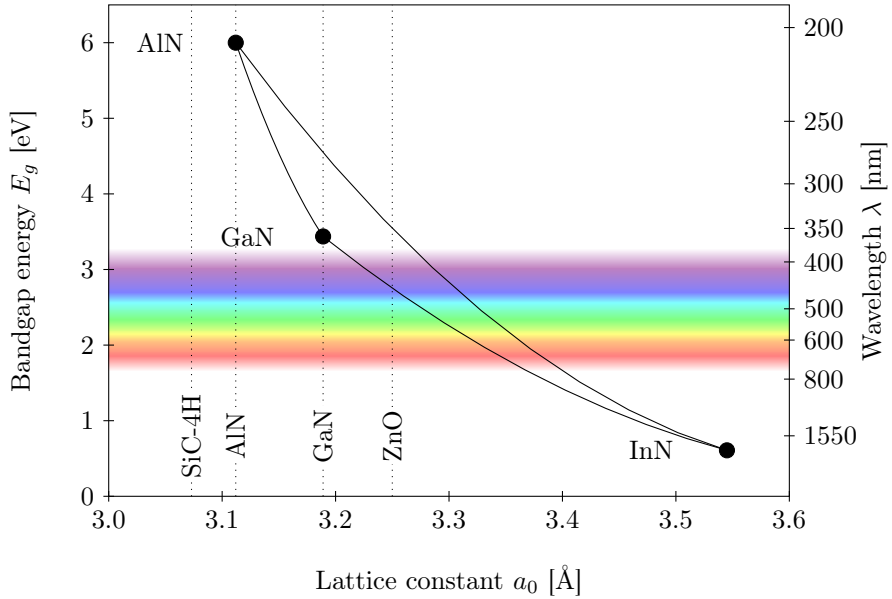
Figure 2.1: Bandgap energy as function of the lattice constant a_0 for the III-nitrides at room temperature using material parameters from [15]. The bandgap is direct for all material compositions. The dotted lines correspond to the lattice constants of some substrates. The large lattice mismatch of the often used sapphire substrate ($a_0 = 4.765$ Å [16]) causes it to lie outside of the graph. Notably, the $Al_{0.18}In_{0.82}N$ alloy is lattice matched to GaN and is thereby enabling some interesting applications [17].

The optical birefringence can influence the polarization properties of LEDs and LDs. Most edge emitting AlGaN-based LDs are oriented such that the optical axis is parallel to the substrate normal. Then the birefringence has little effect. With the laser waveguide oriented along the optical axis, the emitted light is polarized either parallel (transverse magnetic (TM)) or perpendicular (transverse electric (TE)) to the surface normal. However, lasers oriented with the optical axis at an angle to the surface normal can lase at modes polarized parallel or perpendicular to the optical axis [18, 19]. Orienting the LD parallel to the projection of the optical axis avoids this complication. For VCSELs, the optical birefringence can be used to lock the polarization in this otherwise circular symmetric device. This has been demonstrated on substrates with the optical axis oriented perpendicular to the surface normal [20].

6
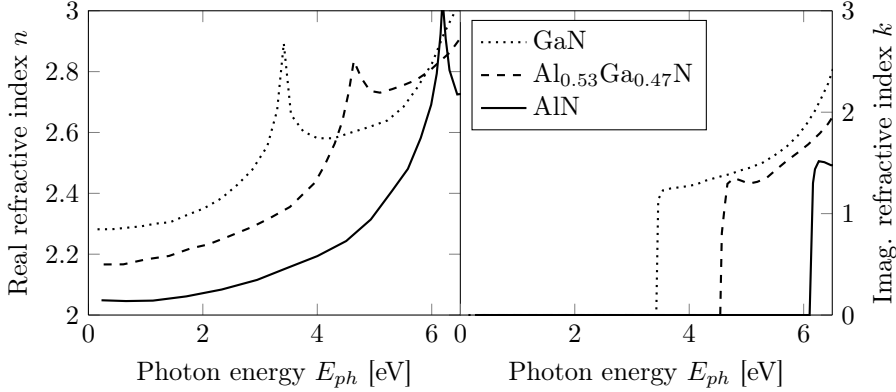
Figure 2.2: The real, n, and imaginary, k, part of the ordinary refractive index for GaN, Al$_{0.53}$Ga$_{0.47}$N and AlN as function of the photon energy, E_{ph}. Data from [21].

2.2 Crystal Structure

The birefringence that was described in Section 2.1 stems from the for AlGaN thermo-dynamically stable wurtzite crystal structure. The hexagonal unit cell of the wurtzite crystal structure is shown in Figure 2.3. The previously mentioned optical axis can here be identified as the crystallographic c-axis, which is normal to the (0001) c-plane. Two other important crystal planes, the (11$\bar{2}$0) a- and the (10$\bar{1}$0) m-plane, and the two lattice constants, a_0 and c_0, are also highlighted.

Although not entirely obvious from the figure, the wurtzite structure is both non-centrosymmetric and polar. The polarity induces strong electrical fields in structures grown on the polar c-plane. As will be discussed in Section 2.6, polarization fields do not appear in structures grown on the non-polar a- and m-planes.

The polarization field ($\vec{P}^{tot}$) is oriented along the c-axis of the crystal. It can be divided in a spontaneous ($\vec{P}^{sp}$) and a piezoelectric polarization ($\vec{P}^{pz}$) component: $\vec{P}^{tot} = \vec{P}^{sp} + \vec{P}^{pz}$ [C/m^2]. The spontaneous polarization is related to the material composition in the crystal lattice and its value can be found in Table 2.1. The piezo-electric polarization is induced by the strain that results from the lattice mismatch in a heterostructure.

It is also possible for the III-nitrides to crystalize in the non-polar zincblende structure. However, such crystals are metastable and reorganize to the stable wurtzite structure at elevated temperatures. While the absence of polarization fields can be advantageous, the inherent metastability makes growth and processing of zincblende III-nitrides quite challenging.
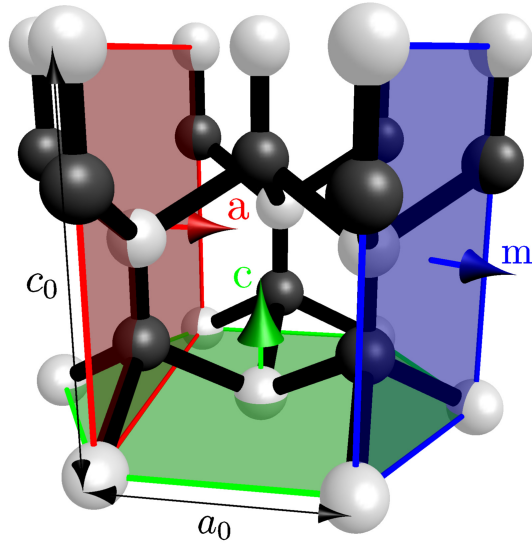
Figure 2.3: Wurtzite crystal structure. The black atoms represent the Al/Ga sublattice and the white atoms the N sublattice. The black lines represent the covalent bonds between the atoms. The three most important crystal planes are indicated: green c-plane (0001), red a-plane (11$\bar{2}$0) and blue m-plane (10$\bar{1}$0).

It should also be noted that the crystal has two faces when it is grown on the c-plane. They are the Ga/Al and the N terminated faces. Normally, growth is performed on the metal terminated face but can in principle also take place on the N terminated face.

2.3 Bandstructure

The crystal structure is reciprocated in the electronic bandstructure that shares the hexagonal symmetry of the wurtzite structure. A complete bandstructure calculation requires a fairly sophisticated theoretical model. For most device applications, only the electronic states in the vicinity of the conduction and valence band edges need to be taken into consideration. For this the $\mathbf{k} \cdot \mathbf{p}$ method can be used. In the most accurate form, an 8×8 Hamiltonian is used to describe the conduction and valence bands and their dependence on crystal strain and alloy composition. The full model is outside of the scope of this work but is described in [15].

Table 2.1: Basic material parameters for GaN and AlN.

Parameter	GaN	AlN	Unit	Ref
E_g (300 K)	3.437	6.00	eV	[15]
a_0 (300 K)	3.189	3.112	Å	[15]
c_0 (300 K)	5.185	4.982	Å	[15]
$m_{e\parallel}^*$ (300 K)	0.21	0.32	m_0	[15]
$m_{e\perp}^*$ (300 K)	0.20	0.30	m_0	[15]
P_{sp}	-0.034	-0.090	C/m^2	[15]
E_{Mg}	130	500	meV	[22–24]
E_{Si}	15	180	meV	[25, 26]

For AlN, GaN and InN, the conduction band minima lies at the Γ-point in the reciprocal space map of the crystal. This is also where the valence band has its maximum, making the III-nitrides direct bandgap semiconductors. Three different bands lie near the valence band maximum and they differ in both energy and symmetry of the electron wavefunction. For GaN, the heavy-hole (HH) band has the largest energy. Below it lies the light-hole (LH) band and even lower in energy is the crystal-hole (CH) band. In bulk GaN crystals the energy separation between the valence bands is quite small (27 meV). For AlN, the CH band has the highest energy, more than 200 meV above the HH and LH bands. For InN, the energy bands and energy states are not well known. Quite recently, in 2001, the InN bandgap was revised from ≈ 2 eV to the currently accepted value of ≈ 0.7 eV [15].

The asymmetric crystal-structure causes the electron masses to differ in directions parallel ($m_\parallel^*$) and perpendicular ($m_\perp^*$) to the c-plane. This also holds true for the holes. For instance, the in-plane LH and HH masses differ, with the LH being the lightest, while they are fairly similar perpendicular to the c-plane [15].

Formation of heterostructures is required for almost all device designs. With heterostructures, the instantaneous transition between different alloy compositions allow the formation of QWs in both conduction and valence bands. Since the heterojunctions in III-nitrides are of type I, the QWs will overlap spatially. For the III-nitrides, the determination of the conduction (Δ_{CBO}) and valence (Δ_{VBO}) band offsets is complicated by the strong strain induced and spontaneous polarization fields. Theory even suggests that the offsets differ depending on the order of the materials in the heterojunction, that is if AlN is grown lattice mismatched to GaN ($\Delta_{VBO} = 0.2$ eV) or if GaN is grown lattice mismatched to AlN ($\Delta_{VBO} = 0.85$ eV) along the c-axis [15, 27]. The remaining bandgap difference appears in the conduction band with Δ_{CBO} values of 2.36 eV for AlN on GaN and 1.71 eV for GaN on AlN. As an example, the valence band offset for Al$_x$Ga$_{1-x}$N QWs embedded in AlN is shown in Figure 2.4 [28].

9
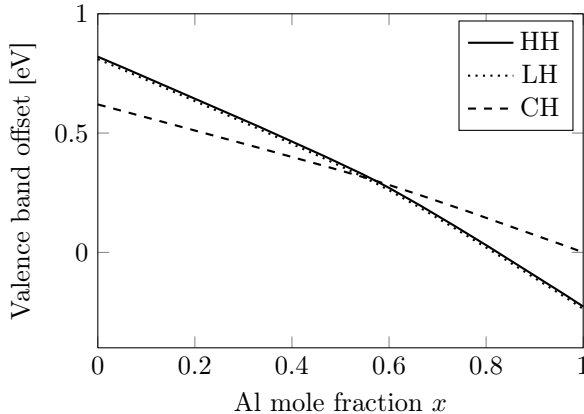
Figure 2.4: The valence-band offset for $Al_xGa_{1-x}N$ QWs compressively strained to c-plane AlN [28].

2.4 Doping

GaN is fairly unique among the wide bandgap semiconductors in that it can be made to have both n- and p-type conductivity. It is known that such conductivity control becomes more difficult to achieve for semiconductors with wider bandgaps [29]. This can be attributed to a larger ionization energy for dopants making it difficult to overcome the intrinsic impurity and defect related background carrier concentration. For GaN and AlGaN, the two most common dopants are Si donors and Mg acceptors. These are also the dopants of choice for AlN where n-type conductivity has been achieved, although with significantly larger resistivity than for n-GaN [30, 31]. However, p-type conduction becomes difficult to achieve as the Al mole fraction increases [32]. Still, p-type conductivity has been demonstrated even for AlN, although with a very low hole concentration of 10^{10} cm^{-3} [5]

H passivation causes problems for the p-type doping of GaN. The H used during metal-organic chemical vapor deposition (MOCVD) growth gets incorporated in the semiconductor, creating Mg-H complexes [33]. Nakamura showed that H can be removed by thermal annealing in a N_2-ambient at temperatures above 700 °C [12, 34]. Such high temperature annealing is also performed on Mg-doped AlN and AlGaN to reduce the H concentration and increase the conductivity in a similar manner.

The p-doping difficulty is also caused by the increase in ionization energy for the Mg-dopant with increasing Al mole fraction. Theoretical work to find an acceptor with lower ionization energy has suggested Be as being a shallower acceptor than Mg

[35], but more recent work [22] finds the ionization energy of Mg to be lower. Using photoluminescence (PL), the measured ionization energy of Be-acceptors was found to be about 80-150 meV smaller than the Mg-acceptor ionization energy in AlN [36]. As the Be-doped AlN was highly resistive, no electrical measurement of the ionization energy could be performed to support the conclusions from the PL measurements. In [22] it was found that the ionization energy of Mg-O complexes is smaller than the Mg ionization energy, suggesting that O co-doping could lead to larger hole concentrations.

Another method to increase the p-type conductivity utilizes the strong internal polarization fields. By altering the material composition, a superlattice (SL) structure is formed where the valence band edge periodically exceeds the Fermi level, thereby reducing the ionization energy for the acceptors [37]. The period length of the $In_{0.13}Ga_{0.87}N/Al_{0.2}Ga_{0.8}N$ SL was 16 nm. With an acceptor concentration of $1 \cdot 10^{19}$ cm^{-3}, the carrier concentration increased by an order of magnitude compared to bulk GaN.

In Paper I we obtained a resistivity of 7 kΩ·cm for Mg-doped $Al_{0.85}Ga_{0.15}N$ by growth using a hot-wall MOCVD reactor, see Section 6.1.2. Although this is a fairly high resistivity when compared to other materials, it is quite low considering the large Al mole fraction. For $Al_{0.7}Ga_{0.3}N$, a RT resistivity of around 10 kΩ·cm was previously shown [38, 39], indicating the applicability of the hot-wall-MOCVD growth technique for growth of p-doped AlGaN.

In Table 2.1, the ionization energies for Si (E_{Si}) and Mg (E_{Mg}) dopants in GaN and AlN are presented. The ionization energies in GaN are lower than in AlN, making doping easier. Still, p-GaN conductivity is low compared to other semiconductors. Therefore, a transparent contact is sometimes required on AlGaN-based light emitters for uniform injection of holes in the recombination or gain region. Although indium-tin-oxide (ITO) can be used it is difficult to form an ohmic p-GaN/ITO contact. Recently, graphene has emerged as a material with similar sheet resistance and transparency as ITO. In Paper V we have investigated the use of metal-free graphene as transparent electrode for GaN based light emitters.

2.5 Substrates

Most of the growth of AlGaN for device applications has been done on sapphire substrates due to their relatively low cost and large temperature stability. The large lattice mismatch between sapphire ($a_0 = 4.765$ Å) [16] and GaN ($a_0 = 3.189$ Å) [40] makes the substrate a seemingly poor choice. However, it is possible to grow GaN template layers with moderate dislocation densities on sapphire. Due to the lattice mismatch, the GaN crystal is rotated 30 degrees compared to the sapphire substrate. The cleavage planes of the GaN layers are, therefore, not aligned to those of the sapphire substrate, which makes cleaving of high quality laser facets problematic [41].

Several other substrates are better suited for growth of III-nitrides with respect to the lattice matching. SiC is a mature substrate, with 100 mm diameter wafers of good quality available [42]. It is also possible to obtain SiC substrates with GaN templates with low dislocation densities.

ZnO is a substrate closely lattice matched to GaN of which large wafers can be produced [43]. Since n-type ZnO substrates with good conductivity exist, and also have the same crystal structure as GaN, they seem to be an ideal substrate. Unfortunately, ZnO substrates are unstable at the growth temperatures and chemistries that are common for MOCVD and hydride vapor phase epitaxy (HVPE) growth of high quality GaN [44]. However, growth of GaN layers on ZnO substrates has been demonstrated at low temperature using MOCVD with DMHy as the N source [44], at room temperature with pulsed laser deposition (PLD) [45], and by using low temperature molecular beam epitaxy (MBE) growth [46].

Growth of AlN and GaN bulk crystals from which native substrates can be produced is also possible. Such substrates are preferable over templates since dislocation densities are orders of magnitude lower. The growth of GaN bulk crystals has received a lot of attention since it has potential to improve performance of blue LEDs and LDs. AlN substrates from AlN bulk crystals would primarily be used for high performance DUV-LEDs, but potentially also for LDs.

A method that can produce high quality GaN substrates is ammonothermal growth [47]. The technique is scalable with autoclave size and currently 50 mm diameter polar wafers are demonstrated [48]. Semi-insulating, p- and n-doped polar GaN substrates are also demonstrated. Recently, larger crystals have also allowed 26×26 mm non-polar substrates [49]. C-plane (polar) wafers with 38 mm diameter and m-plane (non-polar) 10×10 mm wafers are advertised [50].

For AlN, physical vapor transport (PVT), a sublimation-recondensation technique, is the preferred growth method. The method is similar to that used for SiC growth and has been used to grow bulk crystals large enough to produce wafers with 50 mm diameter [51]. However, PVT growth of AlN suffers from significant impurity concentrations. In [52], for instance, both the O and C concentration in the grown AlN crystals are close to $1 \cdot 10^{19}$ cm^{-3} in most parts of the $\approx 15 \times 15 \times 15$ mm boule. Continued development has made 25 mm diameter ultraviolet (UV) transparent true bulk c-plane AlN substrates with low defect densities commercially available [53].

In both AlN and GaN bulk crystal growth, the size of the boule is dependent on the size of the seed crystal. In each iteration of the crystal growth the seed size can increase so with continued commercial interest substrate size can be expected to increase in the coming years.

2.6   Polarization Fields in Heterostructures

The strong polarization fields that are present in the III-nitrides were described in Section 2.2. They are a major detriment to the radiative recombination efficiency for c-plane LEDs and LDs. The effect of these fields can be reduced by growth on non-polar and semi-polar crystal planes. However, the polar c-plane is still the prevalent growth plane for AlGaN based emitters.

The effect of the fields for c- and m-plane growth is shown in Figure 2.5a. The material composition change required for forming the QWs gives rise to a strong electrical field in QWs grown on the c-plane. This field separates the electron and hole wavefunctions in the QW and thereby reduces the radiative recombination probability. To increase the wavefunction overlap, narrow QWs are used in c-plane LEDs.

With growth on the non-polar a- or m- planes, the polarization induced field lies in the plane of the QWs and does not separate the electron and hole wavefunctions in the direction of carrier confinement. The strain also affects the bandstructure differently for growth on different crystal planes. In Figure 2.5b it can be seen that the strain has caused a reduction of the bandgap and a splitting of the LH and HH valence bands in the QW for growth on the m-plane compared to the case of growth on the c-plane.

For green-LEDs, the use of semi-polar growth planes such as $(20\bar{2}1)$ and $(11\bar{2}2)$ is considered. For such planes, the polarization in the QWs is equal or close to equal to that in the barriers. The internal field induced by the polarization will then tend to zero, and charge separation is avoided [54, 55]. The advantage of semi-polar growth is that the incorporation of In in the QWs, required for green emission, is improved compared to growth on non-polar planes [56].

(a) c-plane.

(b) m-plane.
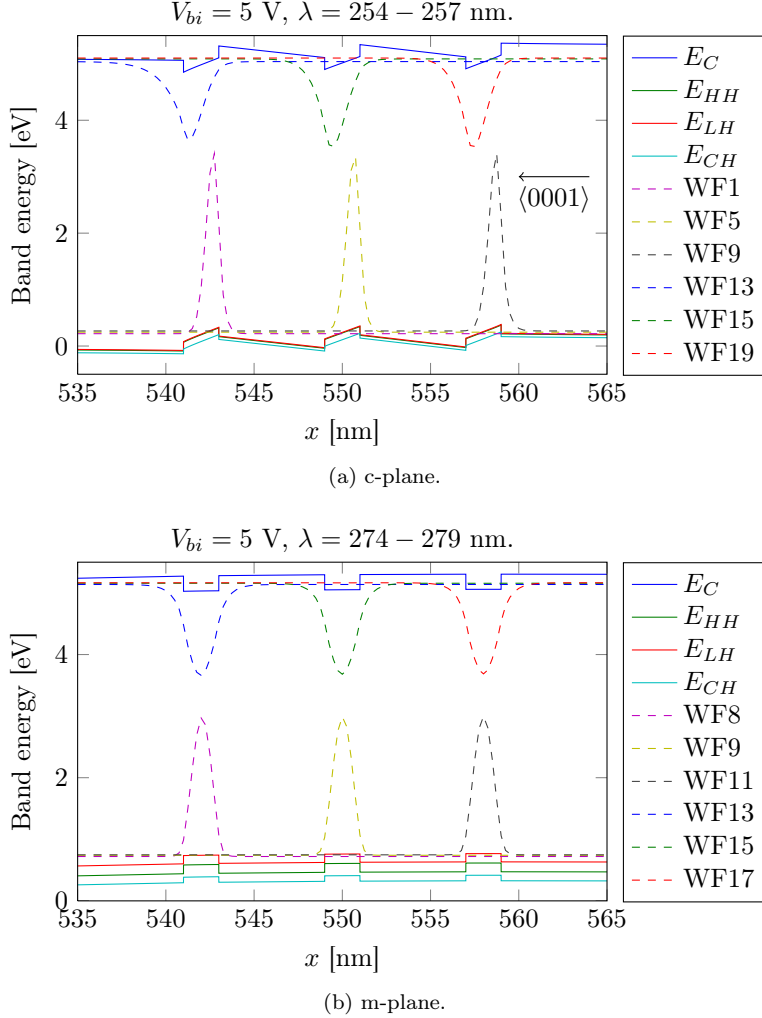
Figure 2.5: The QW region in a DUV-LED design simulated using NEXTNANO. Some relevant wavefunctions were selected to show the overlap between electron and hole wavefunctions in the active region. The simulations were performed on both c- (a) and m-plane (b) to illustrate the reduction of wavefunction overlap for growth on the c-plane. Also note the increase of the emission wavelength due to the strain induced LH and HH splitting in (b).

14

Chapter 3

Deep Ultraviolet Emitters

In recent years, research on AlGaN based LEDs and LDs has expanded from blue emitters towards emitters operating at both longer and shorter wavelengths. In this chapter, the current status and applications of deep ultra-violet emitters is discussed.

3.1 Ultraviolet Radiation

UV light is radiation with wavelengths that are too short to be visible, generally the limit is drawn at 400 nm although slightly shorter wavelengths can be seen. Wavelengths shorter than 300 nm are further grouped into the DUV part of the spectrum. This is only one of many division of the spectrum. Since UV light has many applications, the definitions of the sub-spectra are somewhat overlapping and also differ slightly between different sources. In this work the definitions presented in [57] are used. They are UVA (400-320nm), UVB (320-280 nm), UVC (280-200 nm) and VUV (200-100 nm).

These definitions are based on the interaction with biological matter and the spectral distribution of the sunlight transmitted through the atmosphere, see Figure 3.1. The UVA region is non-germicidal and is partly transmitted through the atmosphere. This part of the spectrum is invisible for humans but is perceived by many birds [58]. UVB is mostly absorbed in the atmosphere and is both germicidal and erythemal (causing skin irritation). In addition to the erythemal and germicidal properties of UVB light, light with UVC wavelengths is ozone producing. The VUV (vacuum UV) wavelengths are heavily attenuated in air and can therefore only be used in vacuum or for wavelengths longer than 150 nm in nitrogen [57].
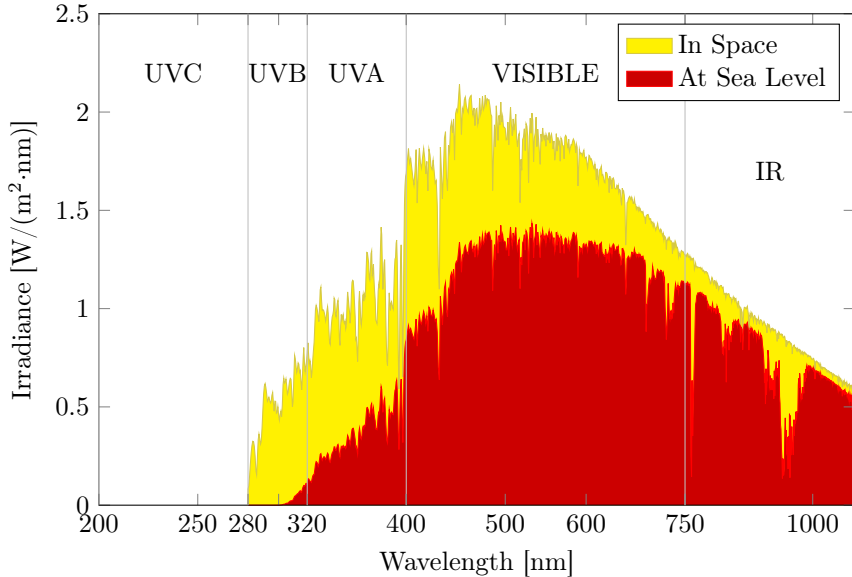
Figure 3.1: Spectral irradiance in space and at sea level from the ASTM G173-03 Reference Spectra [59]. Parts of the solar spectrum are absorbed in the atmosphere. The divisions in the different UV parts of the spectrum is based upon the absorption in the atmosphere and the interaction with biological matter.

3.2 Applications

Air and water purification is a well known application for UVB and UVC radiation. Already in 1909 an experimental plant was constructed in Marseilles, France, where Hg based UV lamps were used to purify 600 m^3 water per 24 h [60]. Radiation at all UVB and UVC wavelengths is germicidal, but most efficient for E. coli pathogen deactivation is radiation at 265 nm, the *"germicidal wavelength"*[57]. However, the peak disinfection wavelength varies somewhat between organisms [61]. The primary light sources used for air and water purification are Hg based gas discharge lamps emitting at the 254 nm Hg line in the UVC spectrum. The UVC power efficiency of such standard low-pressure gas discharge lamps varies between 28-40% over the lamp lifetime of 9000 hours [62]. High efficiency and high power LEDs for the blue region have reached wall-plug efficiencies of 57% at 440 nm with 643 mW optical power and estimated lifetimes of 100 000 hours [63]. Thus, there is an efficiency improvement potential for LED based germicidal lamps for air and water purification operating

at the germicidal wavelength of 265 nm combined with significantly longer lifetimes and smaller dimensions. However, current DUV-LEDs require significant efficiency improvement before being able to compete with the efficiency of Hg based gas-discharge lamps. In some applications, the robustness and compactness of the solid-state LED device compared to the fragile glass tube of the bulky and toxic gas-discharge lamp can outweigh the efficiency shortcomings and make DUV-LEDs attractive in, for instance, transportable disinfection and purification systems.

Short wavelength UV LDs also have the potential to increase the storage density of optical media compared to that of the current Blu-ray Disk™. Blu-ray Disk™operates at a wavelength of 405 nm. However, the use of shorter wavelengths is problematic since plastics tend to deteriorate under UV irradiation [64], thereby requiring new types of optical disks.

The treatment of skin diseases can benefit from narrow band UV sources. For instance, the phototherapy action spectrum peaks around 300 nm, but to limit risk of erythemogenic skin damage wavelengths slightly longer than 300 nm are preferable [65]. Currently, narrow band fluorescent low-pressure Hg lamps at 311 nm are available [66] but they could be replaced by more efficient LEDs.

The interaction with plastics and other materials is another application of UV emitters. The large photon energy allows photo-chemical reactions to occur in materials that are stable under conventional illumination. Examples of applications are, the exposure of photo-resist, UV-curing of adhesives, ozone generation and release of adhesives.

3.3 Light Emitting Diodes

An LED consists of a pn-junction (a diode). When it is forward biased, a current (I) of electrons and holes, from the n and p region, respectively, is driven through the junction. With electrons and holes coexisting at the junction, there is a probability that the electrons and holes recombine by photon emission if the bandgap is direct. Careful design of the junction can increase the radiative recombination probability significantly. In efficient LED designs the radiative recombination efficiency (η_r) can be above 90%.

The part of the current driven through the LED that enters the recombination region gives the injection efficiency (IE) η_i. Nearly 100% IE is possible. The third efficiency of importance is the light extraction efficiency (LEE) η_x. It quantifies the fraction of photons generated in the junction that are emitted out of the LED. LEEs over 80% are possible with proper designs [4, 63]. The product of the three efficiencies gives the external quantum efficiency (EQE) η_e of the LED, defining the fraction of injected electrons converted to output photons. As a complement to the EQE the internal quantum efficiency (IQE) is often used to signify the product of η_r and η_i. However, IQE is often measured using PL, a method that does not accurately take η_i

into account, since the QWs are excited under different conditions than with electro-luminescence (EL), and assumes $\eta_r = 1$ at low temperatures. A more accurate IQE could be obtained by measuring the EQE of LEDs with known LEE [67].

To obtain the power efficiency η_p of the LED, the energy of each output photon (E_{ph}) and the voltage drop (V) over the diode junction at the drive current (I) must be taken into account. The power efficiency (η_p) is often referred to as the wall-plug efficiency (WPE). The resulting expression for the power efficiency becomes:

$$\eta_p = \frac{P_{out}}{VI} = \frac{\eta_e E_{ph} I/q}{VI} = \eta_i \eta_r \eta_x \frac{E_{ph}}{qV} \qquad (3.1)$$

where P_{out} is the optical output power and q is the electron charge.

As will be seen in Section 3.4, increasing the LEE is the currently most pressing challenge for high efficiency AlGaN-based DUV-LEDs. The difficulty of obtaining a large LEE stems mostly from optical absorption in the p-contact region where UV absorbing p-GaN is often used to reduce the contact resistance, but in some cases also from absorption in the substrate. However, there is still a need to improve the IQE and to reduce the resistive losses.

3.4 State-of-the-Art

AlGaN based UV emitters can, and have been, demonstrated to cover essentially the entire UV spectrum, from GaN emission at 364 nm down to AlN emission at 210 nm [5]. Unfortunately, the efficiency of the devices is declining rapidly when shorter wavelengths are approached, as can be seen in Figure 3.2 [6, 68–74].

It has been observed that the radiative recombination efficiency is greatly improved with inclusion of In in the QWs. This usually requires the LED to operate at energies below the bandgap of GaN ($\lambda > 365$ nm). It has been speculated that the increased efficiency is due to In clustering in the QWs forming efficient radiative recombination centers. The clustering theory has recently come under question since the observed clustering effects can be attributed to sample damage during transmission electron microscopy (TEM) analysis [74, 75]. When using repeated High-Resolution TEM imaging, random alloy fluctuations were observed in InGaN layers [76]. Nonetheless, devices with In in the QWs are generally more efficient than those without. For DUV-LEDs, threading dislocation densities (TDDs) larger than 10^9 cm^{-2} are limiting the IQE to values $< 50\%$ [77, 78].

AlN bulk substrates have much lower dislocation densities than the more commonly used AlN templates on sapphire. This allows for the growth of AlGaN heterostructures with low TDD. With pseudomorphically grown layers, an IQE near 70% has been reached [72, 79] at 260-270 nm. An increase of the extraction efficiency from 4% to 15% led to an EQE of 4.9% with 67 mW output power. For DUV-LEDs on sapphire, the IQE is lower due to a higher TDD, but with a thick AlN buffer layer a TDD
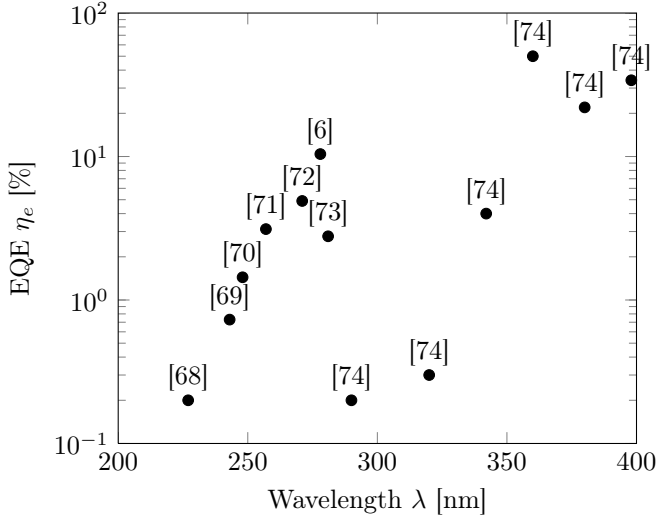
Figure 3.2: Reported EQEs for LEDs at various UV wavelengths. The efficiency drops rapidly when leaving the GaN bandgap region around 365 nm where InGaN QWs are used. The increased efficiencies around the germicidal wavelength at 265 nm can be attributed to a larger development effort because of a potentially large market.

of $2 \cdot 10^8$ cm^{-3} and an IQE > 55% was obtained [6]. With the advantages of the transparent sapphire substrate and a highly reflective p-electrode, an EQE of 10.4% at 9.3 mW and 278 nm was reached [6].

The effect of carbon related absorption at 265 nm in PVT grown AlN substrates [80] was reduced by wafer thinning to 20 μm [72]. Alternatively, HVPE-AlN substrates can be grown on PVT-AlN to obtain both low carbon related absorption (< 10 cm^{-1}), and low TDD. After removal of the absorbing PVT-AlN part of the substrate, leaving 170 nm HVPE-AlN, an EQE of 2.4% at 268 nm with 28 mW output power was reached [81].

As LDs are generally more demanding in terms of material quality than LEDs, with requirements of thick cladding layers and low defect density QWs, the shortest lasing wavelengths for electrically pumped LDs are in the UVA region. A pulsed mode laser emitting at 336 nm with 3 mW output power has been demonstrated [7]. The laser emission was TE polarized. Optically pumped RT lasers have been demonstrated at 242-243 nm [82, 83].

3.5 Droop

Operation of high brightness LEDs requires large current densities. This spells trouble for nitride based LEDs where the EQE is markedly reduced as the current density increases. This phenomenon is commonly referred to as the efficiency droop. It is observed in both visible and DUV LEDs [84]. Currently, the physical mechanism behind the efficiency droop is a question of debate in the research community. It is attributed to a number of effects, among them are Auger recombination, electron leakage, carrier delocalization, dislocations, junction heating, and carrier injection asymmetry [84–88], some of which are discussed below.

The efficiency droop occurs when the current density in the LED increases and scales to a large degree with the cube of the carrier density. This in combination with carrier lifetime measurements implies that Auger-recombination plays a key role [85]. Auger-recombination means that when an electron and hole recombine, instead of emitting a photon, the released energy excites an electron or a hole. The excited carrier thereafter decays to its initial state by phonon emission. Due to the three carriers involved, the recombination rate scales with the cube of the carrier density. However, the measured Auger coefficient is roughly four orders of magnitude larger than what is expected based on other semiconductors [84].

The strong inherent electrical polarization fields are characteristic for the AlGaN materials and distinguish them from other semiconductors. The fields strongly affect the electron structure in the QWs, making them a prime suspect in the search for droop causing effects. The large fields could cause carriers to pass over the QWs without being captured. The fields also enforce the use of narrow QWs, as was shown in Figure 2.5a, causing high carrier densities in the QWs, potentially increasing thermal emission due to junction heating. The growth on non-polar planes should then reduce droop. For a non-polar InGaN LED grown on m-plane GaN, a low efficiency droop of 18% at current densities up to 330 A/cm^2 was observed [89]. This does signify an advantage in terms of reduced droop for growth on non-polar planes. A comparison between c- and m-plane LEDs grown on sapphire and GaN, respectively, shows a reduction in droop for the m-plane LEDs [90]. However, droop was still observed.

Since the dislocation density can be remarkably high in AlGaN-based devices without causing significant nonradiative recombination, efficiency droop mechanisms due to dislocations have been proposed. Carrier localization due to In clustering or the formation of V-shaped pits around defects have been considered. With increased filling of the QWs, defect assisted Shockley Reed Hall recombination could then exhibit a nonlinear behavior, explaining the efficiency droop [84]. Observation of droop in bulk GaN with $< 10^7$ cm^{-2} TDD by PL suggests more fundamental effects such as Auger [91], but does not exclude dislocation related phenomena.

The difficulty in reaching large hole concentrations due to high ionization energy of p-type dopants is attributed to cause droop due to an asymmetric carrier injection into the QWs [86]. Onset of droop was found to occur at lower current densities at

lower temperatures, where the ratio of electron to hole currents was larger due to lower thermal ionization. To reduce electron leakage into the p-region an electron blocking layer (EBL) was used. Since this also creates a barrier for the holes in the valence band, a lower degree of hole injection over the EBL could also contribute to the increased droop at lower temperatures.

Although much effort has been spent on understanding and reducing the efficiency droop it is still present, although significantly reduced in low defect density non-polar m-plane devices [90]. Droop is also observed in the company Soraas high efficiency (68% EQE at 180 A/cm^2) 410 nm LEDs on bulk GaN substrates [92]. The remaining cause for the observed efficiency droop could be due to asymmetric carrier injection, junction heating and/or Auger recombination.

Effective p-type doping is then a remaining obstacle that, if it can be resolved, should reduce the efficiency droop and increase the device performance. However, for the Al-rich layers required for DUV-LEDs this presents great difficulties, since the Mg ionization energy increases rapidly with the Al-content. In the work presented in Paper I, we have achieved a RT resistivity of 7 kΩ·cm for Mg-doped $Al_{0.85}Ga_{0.15}N$ grown by hot-wall MOCVD. This should be compared to the previously achieved resistivity of 10 kΩ·cm for $Al_{0.7}Ga_{0.3}N$ [38, 39] grown by conventional MOCVD.

Chapter 4

Blue Vertical Cavity Surface Emitting Lasers

VCSELs have several advantages over edge-emitting LDs, such as circular beam-profiles, high modulation speed at low currents, simple formation of 2D arrays, and cost reducing on wafer-testing. VCSELs in GaAs-based materials emitting at 850 nm are produced in tens of millions each month and are mainly used in short-range optical data links and optical computer mice [93]. Blue and green emitting VCSELs would be of interest for high-resolution printers, read-out-heads for optical data storage and for bio-medical applications. To achieve blue and green emission, one must explore other material systems, where the GaN-based system has shown to be a promising candidate. However, realizing VCSELs in GaN-based materials is challenging due to the difficulty of growing high reflectivity distributed Bragg reflectors (DBRs), the low electrical conductivity of p-type GaN, and problems to achieve a high material quality and homogeneity. To date, five research groups have realized electrically driven blue VCSELs [8, 20, 94–96]. The performance of these are not yet comparable to GaAs-based devices; the output powers are a factor of 10-1000 lower and threshold current densities a factor of 2-100 times higher. In this chapter, the current state-of-the-art of GaN-based VCSELs is reviewed and key elements in these devices and associated challenges are discussed.

4.1 Basic Principles

As the name implies, the VCSEL is a LD with a vertical cavity, and thus emits light from the surface of the semiconductor wafer. A schematic view of a GaN-based VCSEL is shown in Figure 4.1. The vertical cavity is defined by two mirrors, between which
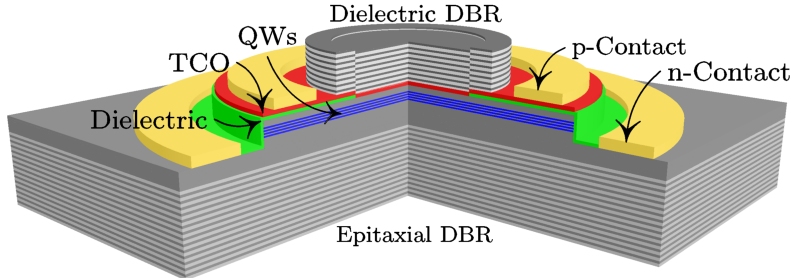
Figure 4.1: Blue VCSEL structure using an epitaxial DBR on the n-side, a dielectric DBR on the p-side, and a dielectric current confinement aperture. The thickness of the QWs and TCO aperture is exaggerated for visibility.

an optical gain region is sandwiched. To achieve lasing, the gain experienced by a mode during one round trip in the cavity needs to equal the losses. A VCSEL has a low modal gain per round trip in the cavity compared to an edge-emitting laser due to the small overlap between the standing optical field and the gain region in the vertical configuration. Thus, high reflectivity mirrors ($R > 99\%$) are required, which are typically realized by distributed Bragg reflectors (DBRs) consisting of dielectric materials or epitaxially grown semiconductor material. Lasing has been achieved in electrically driven VCSELs using two dielectric DBRs [20, 94, 97] as well as using a hybrid approach [96, 98], i.e. one dielectric and one semiconductor-based DBR.

The gain region is similar to the QW region in a blue LED structure. A stack of InGaN QWs is placed in the center of a p-GaN/n-GaN diode. Due to the low conductivity of nitride-based materials, an intra-cavity contacting scheme is used for the current injection in the currently realized blue VCSELs. A current confining aperture is formed on the p-GaN layer, and a thin transparent conductive oxide (TCO) on top of the aperture is used for current injection and to improve the lateral current spreading. The n-GaN layer is typically several wavelengths thick for low lateral resistance and is used as the opposing contact.

4.2 State-of-the-Art

Performance of blue VCSELs is not yet comparable to that of GaAs and InP based VCSELs. There are only a few groups who have demonstrated lasing in electrically driven devices. The best performance is achieved from a VCSEL with two dielectric DBRs produced by Nichia Corporation (Japan) with an maximum optical output power of 0.7 mW CW emission at 451 nm at RT [8]. In the same paper they also demonstrate

pulsed green emission at 503 nm. The blue (451 nm) VCSEL has a threshold voltage of 3.3 V and estimated threshold current density of 3 kA/cm^2. Since Nichia uses two dielectric mirrors in their VCSELs the fabrication is fairly complicated. It requires both wafer bonding and chemical mechanical polishing (CMP) are to remove the GaN substrate before deposition of the second dielectric DBR. The CMP step makes it difficult to control the cavity length accurately and thus the alignment between longitudinal resonance and gain. The same approach with two dielectric DBRs is also used by Panasonic Corporation (Japan) to reach CW lasing at RT [94]. The threshold current is < 2 mA for an aperture diameter of 20 μm with multiple longitudinal mode emission centered around 407 nm and a maximum output power just above 3 μW. The current is very low for such a large aperture, indicating a nonuniform current injection and filamentation. The multiple longitudinal modes are due to the several micrometer long cavity caused by the inaccuracy of the substrate removal.

Researchers at University of California, Santa Barbara (USA) have recently demonstrated another method to fabricate blue VCSELs with two dielectric DBRs [20]. A sacrificial layer with InGaN QWs is included at the bottom of the epitaxial structure. This allows for substrate removal using photoelectrochemical (PEC) etching that improves the control of cavity length significantly compared to CMP. In the PEC process, a 405 nm laser is used to excite the sacrificial QWs. The devices were grown on nonpolar m-plane GaN, thereby avoiding electrical fields in the QWs, which improves the electron-hole wavefunction overlap and thus the gain. Additionally, the devices have a preferred polarization direction (along the [1$\bar{2}$10] a-direction), as is expected due to the refractive index and gain anisotropy introduced by m-plane growth. The peak output power of the devices emitting at 412 nm was 19.5 μW under pulsed conditions at RT, and the threshold current was around 80 mA. Lasing was observed only locally within the aperture.

To avoid substrate removal both optical gain region and bottom DBR can be grown epitaxially. A group at National Chiao Tung University (Taiwan) has demonstrated CW lasing at RT for a device with a 29 pair AlN/GaN DBR grown by MOCVD [95]. Short period superlattices (SPSLs) were introduced in the DBR to reduce strain problems caused by the AlN/GaN lattice mismatch. The threshold current density was 12.4 kA/cm^2 and the peak output power 37 μW.

To avoid the strain induced by the lattice mismatched AlN and GaN layers, researchers at École Polytechnique Fédérale de Lausanne (Switzerland) have used a lattice matched 41.5 pair Al$_{0.80}$In$_{0.20}$N/GaN bottom DBR [96]. Lattice matching allows the growth of QWs with similar defect densities as in the substrate, since no strain related defects are introduced. Current confining apertures were fabricated using SiO$_2$ and with an alternative approach consisting of reactive-ion etching (RIE) passivation of the p-GaN layer. Lasing was observed only in the RIE treated devices at RT under pulsed conditions with a threshold current density of 140 kA/cm^2 and a maximum output power of 320 μW. As will be discussed in Section 4.5, the concave structure resulting from the dielectric passivation is antiguiding, unlike the planar device structure resulting from the RIE passivation approach [99].

4.3   Transparent Contacts

The low p-GaN conductivity is a problem for all GaN-based light emitters. In bottom emitting LEDs and edge emitting LDs, the use of metal current spreaders eliminates the need for lateral current spreading in the p-GaN. The use of metal current spreaders is not possible in VCSELs where they would need to be placed inside the laser cavity, thereby causing large optical absorption loss. Instead, TCOs are used for lateral current spreading as is also done in top emitting LEDs and liquid crystal displays.

Despite the name, TCOs absorb light, mainly through processes such as free electron absorption (FEA) and interband absorption. The absorption coefficient and electrical conductivity are highly dependent on deposition and annealing conditions. The absorption minimum for ITO, a common TCO, is near 450 nm where an absorption coefficient $\alpha_{ITO} = 10^3$ cm^{-1} is reasonable [100]. Thus, the TCO layer needs to be thin, preferably $< \lambda/4$ so that it can be placed at an antinode of the optical field for minimal absorption loss. Apart from ITO, other TCOs such as Ga or Al doped ZnO [101] could also be used, but for all TCOs there is a trade-off between optical absorption and electrical conduction. Besides low optical absorption, a low electrical resistivity of $\rho = 2 \cdot 10^{-4}$ Ω·cm is readily achieved [100, 101].

Besides high lateral conductivity of the TCO, it must also be able to form contacts to p-GaN with low resistivity and be able to withstand the high current densities required for lasing. Unfortunately, p-GaN is sensitive to plasma damage. Surface passivation and even conversion from p- to n-type by Ar-plasma bombardment is possible [102]. This is problematic since deposition of high-quality ITO and other TCOs is predominately done by sputtering, which can create plasma damage. Fortunately, systems promising plasma-damage free deposition of ITO on p-GaN, such as the Evatech Radiance, has recently been demonstrated [103, 104]. Evaporation is also a viable option for ITO deposition [104].

Even without plasma damage the formation of ohmic contacts to p-GaN is challenging due to the low hole concentration in p-GaN and the difference in workfunction between the n-type ITO and p-GaN. To reduce contact resistance, thin high workfunction metal layers are often used in surface emitting LEDs [105], but they do increase the absorption loss.

A p-type TCO such as CuAlO$_2$ [106] or NiO [107] could reduce contact resistance. However, the resistivity of the p-type TCOs is larger than n-type TCOs [106–108]. Instead, a dual layer of TCO could be used: a thin p-type TCO to improve contact resistance to p-GaN with a n-type TCO on top to improve the lateral transport. For this to be effective the TCO pn-junction should have sufficient carrier densities to form a low resistance tunnel junction. A specific contact resistivity of $3.6 \cdot 10^{-5}$ Ω·cm^2 to p-GaN was obtained using a 5 nm thick NiO layer between p-GaN and 200 nm thick n-type TCO [109]. Unfortunately, the 5 nm NiO layer introduced an additional absorption loss of 4.2% at 470 nm.

Another interesting alterative to reduce the contact resistance is the use of a thin strained InGaN cap layer between the TCO and p-GaN. This utilizes the inherent polarization effects in nitride semiconductors to reduce the tunneling barrier length and help with the formation of ohmic contacts [110]. A highly doped InGaN layer was used to improve the ITO contact in [95].

Graphene has recently emerged as a viable alternative to replace TCOs. A single layer of graphene could offer similar sheet resistance ($< 50 \ \Omega/\square$) and transparency (2.3%) as a thin ITO layer [111–114]. The comparatively very thin graphene layer could then be placed exactly at the antinode of the optical field for negligible absorption. Although graphene has a similar workfunction as ITO, the Fermi level and consequently carrier concentration can, due to the low density of states, adapt to the material it is in contact with [115]. This could help in forming low resistance contacts to p-GaN without using metal layers.

The electrical and optical properties of graphene depend on the quality of the graphene layer, in perfect graphene the transparency T is given by the fine structure constant ($\alpha \approx 1/137$) where $T \approx \pi\alpha = 2.3\%$ in the visible [112]. Nearly perfect graphene with mobility of more than $15\,000 \ \mathrm{cm}^2/(\mathrm{V \cdot s})$ can be obtained by exfoliation of graphene flakes from bulk graphite [113, 116]. However, the flakes are typically small and the process is not suitable for industrial production. Alternative methods to grow graphene are e.g. growth by catalytically enhanced chemical vapor deposition (CVD) on metal substrates such as Cu [117, 118] or by high temperature annealing of SiC substrates [119, 120]. The benefit of CVD grown graphene is that it can be released from the Cu substrate relatively easily and thereafter transferred to devices or test structures [121].

Graphene has been examined for use as a transparent current spreader for GaN-based LEDs [122–126]. In these studies the graphene layer was placed between a metal bondpad and the p-GaN surface. Although current spreading was observed in the graphene layer the possibility that the bondpad contacted the p-GaN surface through the graphene layer cannot be excluded. The inclusion of metal either as a dopant into the graphene layer or as a thin interlayer (1-2 nm) at semiconductor surface was used to increase the conductivity and to improve the contact to p-GaN [123, 126].

In Paper V we have examined the use of metal-free graphene as a transparent electrode for GaN-based light emitters. Single-layer CVD graphene grown on Cu foil was released by a electrolytic process and mechanically transferred to the samples [121]. The transfer was repeated to achieve dual-layer graphene. We were able to achieve lateral current spreading using single-layer graphene, see Figure 4.2a. The maximum current density for single-layer graphene, seen in Figure 4.2b, of 300 A/cm^2 could be increased to 1 kA/cm^2 by using dual-layer graphene. This is close to the threshold current density required for GaN-based VCSELs (3 kA/cm^2 [8]). The contacts exhibited a non-linear current-voltage dependence and degraded rapidly during operation. The sheet resistance of the CVD grown graphene was approximately one order of magnitude larger than the than what should be possible when comparing with exfoliated

(a)   (b)
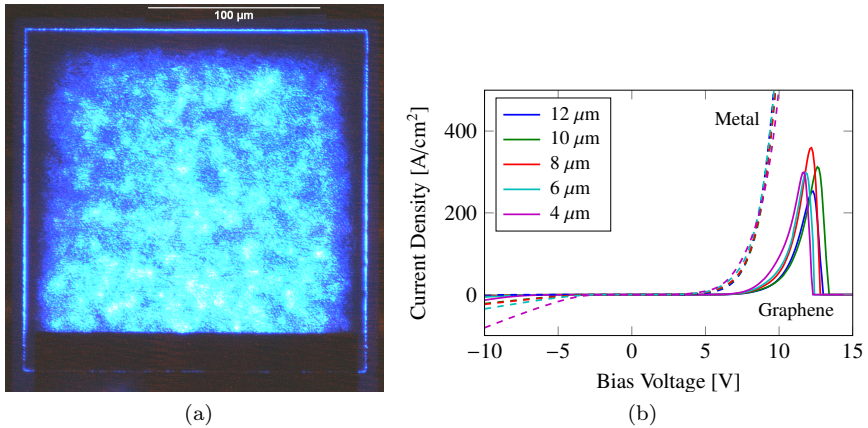
Figure 4.2: (a) A transparent graphene electrode is used to drive a 100×100 μm blue LED. (b) Current density as function of bias voltage for circular LEDs with different aperture diameters. Both metal (dashed) and single-layer graphene (solid) electrodes were used. With increased current density and forward bias the graphene contact is destroyed, as seen from the rapid decrease in forward current.

graphene flakes [116].

Although promising, the results suggest a need for improved contact reliability and reduced contact resistance. The use of a protective dielectric coating such as hBN [127] or metal oxides [128] could be used to increase contact reliability and improve graphene characteristics. Alternatively to reduce the contact resistance interesting approaches are using direct growth of graphene on the p-GaN surface, doping, or the use of contact enhancing interlayers similar to those discussed earlier for TCO contacts. In the interim though, the proved ITO contact seems a more viable choice.

4.4 Distributed Bragg Reflectors

A DBR consists of a stack of layers with alternating refractive index. The reflectivity for a specific wavelength is maximized when the thickness of each layer corresponds to a quarter of the optical wavelength in that layer. Constructive interference causes the reflections at each interface to add up in phase and yield an overall very high reflectivity. The total reflectivity increases with the number of pairs and the refractive index difference between the layers. A high refractive index contrast also increases the stopband of the mirror, i.e. provides high reflectivity over a broader wavelength range. The materials in the DBR can be dielectrics or epitaxially grown semiconductors.

The mirror on the p-doped side of electrically driven GaN-based VCSELs have so far been dielectric, since a TCO has been used between the mirror and the top p-GaN layer to improve lateral current spreading across the aperture. A dielectric mirror also provides a larger bandwidth, which facilitates the spectral matching between gain, cavity resonance and mirror reflectivity. The dielectrics used vary but the low index material is typically SiO_2, whereas different high index dielectrics such as Ta_2O_5 [20, 95, 97], TiO_2 [96], HfO_2 [129] and ZrO_2 [94] have been used for blue DBRs. Although only a few (8-10) periods are required for high reflectivity, the thermal conductivity in dielectrics is low compared to epitaxially grown layers. The use of two dielectric DBRs could therefore make devices more susceptible to overheating.

On the n-side of the VCSEL, both dielectric and epitaxial materials have been used. By using an epitaxially grown mirror, the epitaxial growth becomes more complicated while device processing is simplified. For epitaxial DBRs, both lattice matched $Al_{0.8}In_{0.2}N$/GaN [96] and strained AlN/GaN [95] DBRs have been successfully used in blue VCSELs. The use of lattice matched $Al_{0.8}In_{0.2}N$ and GaN layers enables growth of DBRs without strain introduced defects and dislocations but requires precise control of the growth conditions. The best results were reached using MOCVD [130, 131], but MBE has also been used to grow crack free AlInN/GaN DBRs [132, 133]. Due to the low refractive index difference, 41.5 pairs were used in the MOCVD grown VCSEL [96]. For the binary AlN/GaN DBR, fewer pairs are required to reach the same reflectivity due to a larger refractive index difference. 29 pairs were used to achieve a reflectivity above 99% [95]. However, the strain will need to relax either through formation of dislocations or cracks. Dislocations can be tolerated to a remarkably high extent in blue InGaN-QWs [134] but are detrimental to laser lifetime [135]. Crack free growth is, on the other hand, needed both for the formation of a functional active region, with electrically pumped QWs, and for high reflectivity DBRs with low optical losses.

Most device structures are grown on GaN templates on sapphire substrates, or recently on bulk GaN substrates with low dislocation densities. This is problematic for growth of epitaxial DBRs with AlN or AlGaN as the low index material. The lower lattice constant compared to GaN in these layers leads to tensile strain buildup in the structure that is often released by crack formation. To cope with the introduced strain, SPSLs have been used [95]. Alternatively, for growth on SiC substrates, both GaN and AlN layers are compressively strained. Crack-free growth of AlN/GaN DBRs is possible without the insertion of additional strain compensating layers. A strain balanced state where GaN layers are compressively strained and AlN layers tensile strained for a residual net stress close to zero is reported [136]. The strain balance is attributed to only partial relaxation of the first layers in the DBR.

Using MBE we have grown a 22.5 period AlN/GaN DBR on SiC a with strain balancing SPSL inserted in every fifth pair. Although no strain compensating layers were needed for crack-free growth on 6H-SiC [136], we found that the inclusion of SPSLs improved growth quality so that crack-free growth was obtained on 4H-SiC. A cross-sectional scanning electron microscopy (SEM) image of part of the DBR is shown
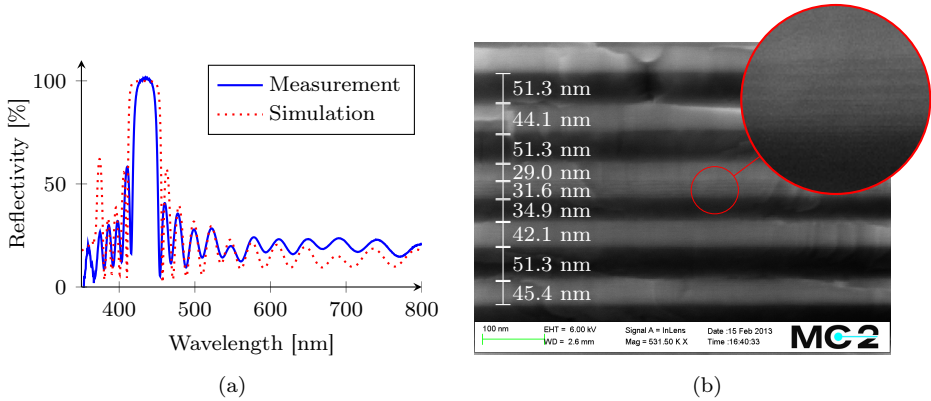
Figure 4.3: (a) Measured and simulated reflectivity as a function of the wavelength for a 22.5 pair AlN/GaN DBR with intermediate SPSLs grown by MBE. (b) SEM image showing some of the DBR periods, the one in the center contains a SPSL. The bright fields are GaN and the dark fields AlN. Layer thicknesses are indicated. A part of the SPSL is enlarged.

in Figure 4.3b. The AlN/GaN SPSL insertion in one GaN layer is shown in the center of the image. The layers are homogeneous with sharp interfaces up to the surface of the DBR as are seen in the SEM image. This is supported by atomic force microscopy (AFM) scans of the top surface, shown in Figure 4.4, where stepflow growth morphology is visible. The screw type dislocation density is estimated at $2 \cdot 10^9$ cm^{-2}, which is fairly large when considered for use in the active region of a LD, but it is reasonable compared to what can be expected for AlN/GaN heterostructures. As can be seen in Figure 4.3a, the maximum measured reflectivity is slightly above 100%. This is clearly unphysical, with the slight overestimation of the peak reflectivity most likely caused by a slightly lower reflectivity of the Si reference than expected. A simulation of the DBR structure is also included, where it can be seen that the bandwidth of the measured reflectivity is slightly smaller than the simulated bandwidth. This can be caused by, for instance, thickness variations in the grown layers, or an incorrect thickness of the layer pairs with SPSL. However, taking the experimental uncertainties into consideration there is a fairly good agreement between measurement and simulation, especially when considering the overlap between reflection peaks in the tail extending into the visible region.

With epitaxial DBRs there is a potential advantage if they can be made sufficiently conductive so that the lower intracavity contact can be replaced by the bottom DBR. The cavity length would be significantly shorter, since the thickness of the highly

(a)　　　　　　　　　　　　　　　　(b)
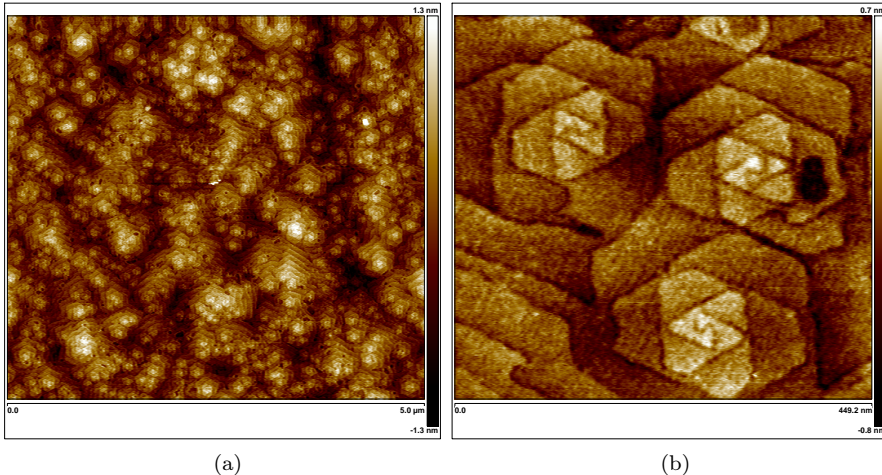
Figure 4.4: (a) 5×5 μm AFM scan showing stepflow growth morphology on a MBE grown 22.5 pair AlN/GaN DBR with intermediate SPSLs. (b) Closeup on a cluster of three screw type dislocations. A dislocation density of $2 \cdot 10^9$ cm^{-2} was estimated from the 5×5 μm scan.

doped n-GaN layer below the QWs could be reduced. The large FEA in this layer, that is situated in the area with the highest optical intensity of the laser, could then be avoided, albeit with an increased FEA in the bottom DBR. The device design and processing would also be simplified by combining the conductive DBR with a conductive substrate contacted with a bottom contact, thereby avoiding the need to etch through the active region for contact formation. Additionally, the current crowding effects in the n-GaN contact layer would be avoided. Conductive n-type DBRs have been demonstrated [136, 137], but the specific resistivity of $2 \cdot 10^{-3}$ $\Omega \cdot$cm^2 is somewhat too large for this to be a viable alternative compared with the current n-GaN intracavity contacts. To reduce the resistance, the large conduction band offset between AlN and GaN could be softened by using compositional gradings, such as thin Al$_{0.5}$Ga$_{0.5}$N inter-layers, SPSLs, or even sinusoidal modulation of the material composition [138]. The AlN layers could also be replaced by InAlN layers or AlN/GaN SPSLs with a increased conductivity compared to AlN, through the formation of a conductive mini-band. However, the lower refractive index contrast in such structures would require more periods in the DBR.

31

4.5 Lateral Current Confinement

An aperture confining current to the center of the device is needed in VCSELs, to achieve sufficiently large current densities to obtain gain at low bias currents. Preferably, the aperture should also confine the optical field to increase the overlap between the optical mode and the gain region. In GaAs-based VCSELs, an oxide aperture formed by selective wet oxidation of a high Al mole fraction AlGaAs layer is used with high reliability [139]. This is advantageous since the reduced refractive index of the oxide also contributes to the confinement of the optical field. It also allows the whole epitaxial structure to be grown in a single run since the aperture layer is inserted into the epitaxial stack during the growth. Other techniques such as proton implantation, regrowth and buried tunnel-junctions have been explored in other material systems where the inclusion of a selectively oxidized AlGaAs layer is not possible.

For AlGaN-based devices, apertures formed by selective oxidation of AlInN have been demonstrated [140, 141]. However, the differential resistance of LEDs increased with the introduction of the n-type AlInN layer. The LEDs were driven with current densities up to 20 kA/cm^2, which could allow the threshold current density required for lasing to be reached. Combining the oxidized AlInN aperture with a epitaxial lattice-matched AlInN/GaN DBR is potentially problematic since the layers in the DBR would be oxidized simultaneously with the aperture.

An alternative to selective oxidation is regrowth, which has been demonstrated for MOCVD grown edge emitting LDs. Two regrowths were required to introduce a MBE-grown resistive Al$_{0.83}$In$_{0.17}$N current confining aperture in the p-Al$_{0.06}$Ga$_{0.94}$N cladding layer [142]. The edge-emitting laser diodes had threshold current densities slightly larger than 3 kA/cm^2. As an alternative to the resistive Al$_{0.83}$In$_{0.17}$N layer, an insulating AlN layer could be used. A blue microcavity LED has been demonstrated with a buried AlN current aperture that was formed by epitaxial regrowth [143]. The regrowth process is fairly complicated and risks introducing optical losses, and increasing the electrical resistance. But, regrown apertures could still be of interest as current confining apertures for blue VCSELs, for instance if p-conductive DBRs could be realized.

So far, patterned SiO$_2$ has mainly been used as current confining aperture in AlGaN-based VCSELs. Due to the aperture, the transparent contact and DBR above will become somewhat concave as can be seen in Figure 4.1. This can result in an anti-guiding device structure with significant optical leakage loss [99]. Preferably, a slightly convex DBR should be used for improved optical confinement. Despite their theoretical disadvantage, anti-guiding apertures are used in state-of-the-art blue VCSELs [8].

An alternative way to create a current confining aperture that does not result in a concave top DBR is to electrically passivate the p-GaN by RIE treatment [96]. The lithography used to define the RIE induced aperture could in an additional step be used for the patterning of a thin p$^+$-InGaN or NiO layer that could reduce the contact resistivity of the TCO. An additional benefit with this approach would be that the device becomes slightly convex, thereby improving the lateral optical confinement.

Chapter 5

Quantum Cascade Lasers

Nitride based QCLs have not yet been demonstrated. However, with other material systems the QCL has in recent years become an important laser source for emission in the mid and far IR. In this chapter, the operating principle and major applications of QCLs will be discussed, followed by a discussion of AlGaN based QCLs.

5.1 Operating Principle

The QCL is an intersubband (ISB) device. This means that all transitions take place in either the conduction or the valence band. Consequently, the QCL only requires one type of carriers and is therefore a unipolar device. The conduction band is nearly always used, removing the need for p-type doping. The concatenation of multiple thin QWs allows the wavefunctions of the QWs states to overlap, forming a closely spaced set of energy states, a mini-band. By adjusting the dimensions and spacing between coupled QWs, the ISB transition energy can be engineered for ISB absorption or gain at a particular wavelength.

The gain region, see Figure 5.1, consists of gain stages connected by transport stages. Both gain and transport stages typically consist of several QWs, albeit with different well/barrier spacing. The stages are designed in such a manner that electrons can tunnel into an excited state of the gain stage (level 3) and then, after a stimulated emission process into a lower energy state (level 2), tunnel out into the next transport stage, often with the help of an optical phonon (to level 1). The electron then proceeds through the transport stage towards the next gain stage where it enters into the excited state of that gain stage. In this manner, a cascading structure is created where each
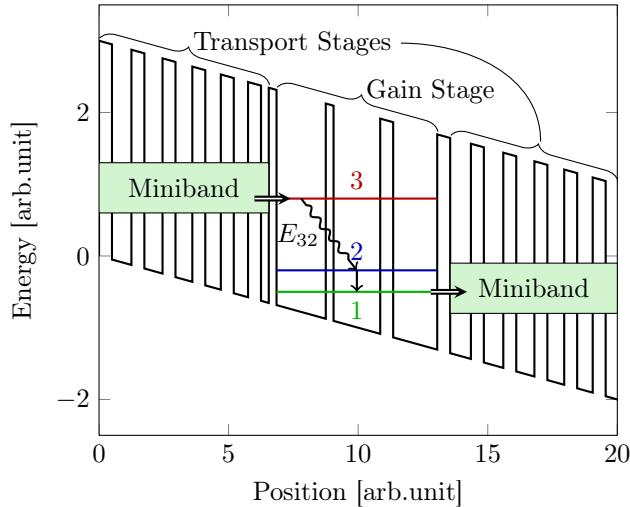
Figure 5.1: Illustration of a QCL active region design. Here, the gain stages consist of three coupled QWs with three energy levels. The lasing transition is between levels 3 and 2. Level 3 is populated by tunneling through the miniband of the first transport stage. The lower lasing state (level 2) is quickly depleted by an optical phonon assisted transition into level 1. Electrons in level 1 then tunnel through the miniband of the second transport stage where they gain energy relative to the conduction band edge as they approach the next gain stage. The strong polarization fields inherent to AlGaN-QCLs grown on polar c-plane substrates are not included.

electron passing through the device can generate several photons. At a certain injection rate, ISB population inversion and optical gain are achieved [144].

The ISB operation gives large freedom in the obtainable lasing wavelength. This is because the dependence on the material bandgap associated with interband lasers is removed. Instead, the lasing wavelength is determined by the width and depth of the QWs, thereby allowing different wavelengths by small design changes.

The electron recycling in the multiple gain stages makes the drive current required for a given output power lower than for diode lasers. The required drive voltage is, on the other hand, higher due to the multiple gain stages. Notably, the WPE of QCLs was initially low, $< 1\%$, but recently a WPE of over 50% was reached at up to 9 W optical output power at 5 μm for a InP-based QCL [145, 146]. However, GaAs-based interband CW LDs at 940 nm can have WPE over 75% at RT with 100 W output power [147].

5.2 Applications

InP-based QCLs with more than 100 mW CW output power at RT have been demonstrated in the wavelength range 3.8-11.5 μm [148]. This is a wavelength range where most molecules have characteristics absorption lines. Consequently, monitoring and measurement of trace gases is a key application for QCLs.

The detection is usually done by tuning the wavelength of the QCL over the vibrational and rotational absorption lines of the molecule of interest. Wavelength tuning can be achieved by changing the temperature (slow) or bias current (fast), but often both simultaneously. The laser light is transmitted through the gas sample, and the intensity after transmission is detected. By analyzing the wavelength dependence of the absorption, the trace gases and their concentrations can be determined [149].

Generally, smaller molecules have higher rotation and vibration frequencies than larger molecules and they are consequently absorbing at shorter wavelengths. As will be discussed in Section 5.3, the use of III-nitrides can potentially allow QCL operation at shorter wavelengths than what is possible with conventional materials. This would allow for increased detectability of trace amounts of smaller molecules such as HCl ($\lambda_{vib} = 3.34$ μm) and HF ($\lambda_{vib} = 2.42$ μm) [150].

Operation at shorter wavelengths could also enable the QCL to be used in telecom applications. Due to the symmetry of the ISB gain spectrum, the laser can be modulated essentially without chirp, which reduces the optical pulse broadening due to chromatic dispersion in optical fibres. The linewidth of a QCL can also be very small, with linewidths of 12 kHz being reported [151]. The low linewidths are attributed to the low refractive index dependence on population inversion fluctuations in QCLs, compared to interband LDs [151]. The results in the appended Paper II show that the ISB transition energy of AlN/GaN QWs has a very weak temperature dependence, corresponding to a wavelength drift of only 38 pm/K. This is an order of magnitude lower than the wavelength drift of 1.55 μm InP interband lasers (≈ 400 pm/K) [152] and could potentially remove the requirement for active temperature control.

Long wavelength QCL operation for THz applications is also possible. For instance, a 100 μm (≈ 3 THz) GaAs-QCL has been demonstrated [153]. Potential applications of such lasers are imaging for security and medical purposes. However, current THz QCLs can only operate at cryogenic temperatures, mainly limited by the small longitudinal-optical (LO) phonon energy (≈ 36 meV). The larger LO-phonon energy (≈ 90 meV) of the III-nitrides could allow RT QCL THz-lasing [154]. Using a GaN/AlGaN QCL structure, ISB related EL at 2.7 THz at 7 K has been demonstrated [155].

5.3 Limiting Effects at Short Wavelengths

The first QCL employed InGaAs/InAlAs QWs grown on an InP substrate and operated at a wavelength of 4.2 μm [144]. Today, RT lasing has been demonstrated at

wavelengths as short as 3.0 μm using $Ga_{0.21}In_{0.79}As$ wells and $Al_{0.89}In_{0.11}As$ barriers on an InP substrate [156]. At cryogenic temperatures, wavelengths of 2.63-2.65 μm have been demonstrated with InAs/AlSb QWs grown on InAs substrates with operation at temperatures up to 175 K [9].

Presently, the physical effect that is the main obstacle for reaching shorter wavelengths is carrier leakage into the L-valley in the InAs QWs. The offset between Γ- and L-valley energies in InAs is 0.73 eV, which limits the separation between the upper laser level and the bottom of the QW [9]. Although it has been suggested that it might be possible to reach lasing at even shorter wavelengths, given that the intervalley scattering time can be comparable to the electron lifetime in the upper lasing state [157], for efficient lasing the remote valleys have to lie above the upper lasing level.

For the AlN/GaN QCL, the remote valleys of GaN are therefore expected to be the factor limiting the shortest obtainable wavelength. In theoretical calculations of the bandstructure, the obtained remote valley separation varies somewhat, from 2.1 eV [158] to 1.6 eV [159]. Using pump-probe spectroscopy, the remote valley separation separation was measured to 1.12 eV [160] and 1.34 eV [161] and recently a photoexcited field emission measurements gave a value of 1.18-1.21 eV [162]. Using the smallest value, 1.12 eV, as the maximum energy of the upper state in a three level laser, the shortest obtainable wavelength for an AlN/GaN based QCL can be predicted. In a very crude approximation, all of the excess remote-valley energy-separation can be used to increase the photon energy, thereby making it 0.39 eV larger than that of an InAs/InSb QCL. The resulting lower limit of the lasing wavelength then becomes 1.45 μm.

For a more accurate estimation of the lower wavelength limit, the design of the gain region of the AlN/GaN QCL needs to be taken into consideration. The large optical phonon energy increases the optimal separation between the two lower laser levels slightly. The effect of strain on the remote valley separation also has to be considered. In addition, the inherent polarization fields could potentially also reduce the shortest obtainable lasing wavelength due to the tilt of the conduction band in the QWs. Still, the measured remote valley separation is significantly larger in GaN than in InAs, making it likely that QCLs with wavelengths shorter than 2.6 μm can be realized using the III-nitrides, potentially even reaching telecom wavelengths (1.55 μm).

5.4 Waveguide Design

In the design of a laser, the waveguide that confines the optical energy to the active region with optical gain is one of the most important elements. Quantitatively, this is expressed by the optical confinement factor. For interband lasers, it is defined as the normalized overlap integral between the mode intensity and the QWs (the gain elements). However, for QCLs it is common to define the gain region as the whole QCL

stack, effectively smearing out the gain from the region with gain onto the transport regions between the active gain elements. This definition is useful since it allows for easy separation of the design of the waveguide and the design of the gain structure. The other more physically correct alternative is to define the confinement factor as the overlap with the reaction cross-section of the wavefunctions in the QWs where the transitions providing optical gain occur. But as the reaction cross-section of the gain elements is strongly dependent on the design of the QW structure, the latter definition requires the confinement factor to be recalculated for each modification of the gain structure.

Apart from good optical confinement, the waveguide should also have low optical loss to limit device heating and power consumption. For e.g. telecom applications it is also of importance that the waveguide only supports the fundamental spatial mode. The guided mode profile should also match the mode profile of the single mode optical fiber for efficient coupling.

The optical mode needs to be confined both vertically and horizontally. Initially, we limit the discussion to the vertical confinement which is more difficult to achieve in AlGaN-based QCLs compared to QCLs in more conventional III-V semiconductors.

For InGaAs/InAlAs based QCLs, the lattice matched InP substrate and a cap layer of InP are used as waveguide cladding layers and current injection and extraction layers. For GaAs/AlGaAs based QCLs, optical confinement is obtained using a thick high Al fraction AlGaAs layer grown on the GaAs substrate [163] or by using a heavily doped GaAs substrate with the real part of the refractive index lowered by a plasmon resonance [164]. For InAs/AlSb based QCLs, the waveguides are also based on plasmon resonances using a heavily doped InAs substrates with InAs/AlSb spacer layers [165].

If we now consider an AlGaN-based QCL for emission at 1.55 μm, with GaN QWs and AlN barriers (and possibly AlGaN layers in the transport stages), the mean refractive index of the gain region is between those of the two limiting compositions of AlN and GaN. The refractive index of AlN is lower than that of GaN, so it is possible to use AlN layers as cladding layers. However, there is a significant drawback with this approach since the conductivity of n-doped AlN is very low. The resistive losses incurred in the waveguide cladding layers make such an approach quite unfeasible for a device where electrical pumping is required.

The approach used for the InAs/AlSb [165] and AlGaAs/GaAs [164, 166] based QCLs, to heavily dope cladding layers to reduce the refractive index by means of plasmon resonance, could be another possibility. It requires that GaN can be sufficiently doped so that the refractive index is reduced enough below that of the equivalent AlGaN core. Some theoretical investigations have been performed [167], showing that with an electron concentration of $1 \cdot 10^{20}$ cm^{-3} the complex refractive index of GaN at 1.55 μm becomes $2.11 + i0.011$, close to that of AlN. In a waveguide using such n^{++}-GaN cladding layers, the resulting free electron absorption is expected to cause quite significant losses. The calculated waveguide loss is 230 cm^{-1} at 1.55 μm [167], unfortunately a rather significant waveguide loss.
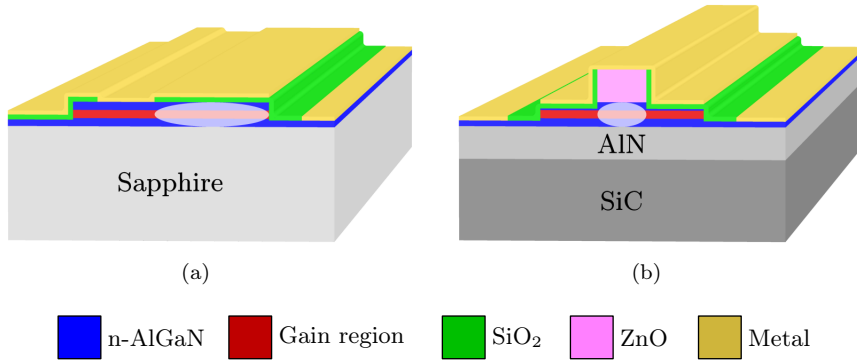
Figure 5.2: (a) The waveguide proposed in Paper III, which allows the guiding of a low loss TM polarized mode (white ellipse) in the region to the right of the metal contact. (b) The waveguide described in Paper IV, which allows the guiding of a low loss TM polarized mode (white ellipse) in the region beneath the ZnO contact.

In this work, two alternative waveguide designs are therefore investigated. Both allow for low-loss, single mode guiding with good optical confinement while allowing current injection into and out of the gain region. The designs are shown in Figure 5.2.

In Paper III a waveguide design (Figure 5.2a) which avoids the conduction problem of AlN by using a nonconductive dielectric coating (SiO_2) for the vertical mode confinement from above and the substrate (sapphire) from below is presented. The current is injected laterally through a contact metallization in an opening in the dielectric. In the paper we show that the mode loss is fairly low, although the optical mode is in direct contact with the ohmic metal contact. For this waveguide, the simulated metal induced loss for the guided TM-like mode is 6.1 cm^{-1} with a confinement factor of 52%. A sapphire substrate was chosen due to its low refractive index of 1.746 at 1.55 μm [168]. Other potential substrates with suitable refractive indices are AlN ($n = 2.1$ [21]) and ZnO ($n = 1.93$ [43]). Unfortunately, SiC ($n = 2.6$ [169]) and GaN (n=2.3 [21]) have refractive indices that are too large.

The waveguide design in Paper IV (Figure 5.2b) removes the need for the lateral current injection. Instead, a conductive and transparent ZnO layer is used as the top cladding layer. We also show that by using a 2 μm thick AlN lower cladding layer, a SiC substrate can be used without introducing significant radiation leakage loss to the substrate. Waveguide properties were examined for core regions with average AlGaN mole fractions ranging from 25 to 75%. Losses due to FEA were accounted for and a single TM-mode design with a 40% confinement factor and 39 cm^{-1} loss was identified and examined in more detail.

5.5 Cavity Mirrors

Aside from waveguide losses, the losses in the cavity mirrors are often significant in diode lasers and QCLs with cleaved mirrors. Due to the low refractive indices of GaN and AlN at 1.55 μm (Figure 2.2) mirror losses are expected to be large for AlN/GaN QCLs. Given a reasonable mode index of 2.2, the power reflectivity of an ideal cleaved facet is only 14%.

To achieve ideal facets, cleaving of the epi-structure along crystal planes is generally considered to be the best method. The cleaving is done to obtain an atomically flat surface perpendicular to the laser waveguide. Most GaN based lasers are grown on sapphire substrates. Unfortunately, the crystal planes of the substrate and epi-layers are misaligned in this configuration, making reproducible cleaving of atomically flat mirrors very challenging [41]. With new substrates such as GaN and AlN emerging, the cleaving of laser mirrors becomes feasible.

Dry etching of the mirror facets can be a more reproducible option for lasers grown on sapphire substrates. The mirrors will, however, be rougher than perfectly cleaved facets and thus suffer from increased scattering losses. Losses will also increase if the facets are non-vertical. Both effects are inherent in dry etched mirrors but can be reduced by optimizing the etch mask, process chemistry and plasma power levels [170, 171]. With the longer emission wavelength of a NIR-QCL, the influence of surface roughness is less significant than for a laser in the visible.

Another process that can yield high quality mirrors is focused ion beam milling. This is a mechanical process were an ion beam is used to sputter away material. The process is not suitable for mass fabrication since only one device can be processed at a time [172].

Wet etching of AlGaN materials is almost impossible with most acids. However, it is possible to etch both GaN and AlN using heated KOH. This etchant is selective with respect to the crystal planes, making it possible to use it to reduce the roughness of a dry etched mirror [173].

The deposition of a dielectric coating on the mirror surface can be used to increase or decrease the mirror reflectivity. In all likelihood, a dielectric high reflectivity coating is required to reduce the mirror losses for AlGaN based QCLs.

To further reduce the mode loss, a distributed feedback (DFB) structure can be introduced along the waveguide, for instance by etching of a grating into the waveguide ridge. This will eliminate the need for highly reflective cleaved mirrors and at the same time enable the single longitudinal mode operation needed for many applications. When estimating the required threshold current in Paper IV, the use of a DFB grating is assumed to reduce the modal losses, from the 20 cm^{-1} that would arise from the cavity mirrors for a 1 mm long QCL, down to 11 cm^{-1}.

Chapter 6

Epitaxial Growth and Device Processing Methods

Epitaxial growth and device processing methods for III-nitride semiconductors are similar to those for other semiconductors. Some adaptation is needed because of the large chemical inertness, mechanical hardness and optical transparency. Initially, the most common epitaxial growth and substrate preparation methods will be described, followed by some important device processing methods.

6.1 Epitaxial Growth and Substrate Preparation

The first step when an optoelectronic device is produced usually consists of epitaxial growth. The substrate, is overgrown with a semiconducting material under such conditions that it crystallizes, layer by layer, on the substrate. This process is called epitaxy. The substrate can be of the same material as the deposited semiconductor (homoepitaxy) or of a different material (heteroepitaxy). The huge technological importance of epitaxial growth stems from the ability to change the material compositions and doping levels during the growth, thereby forming a crystal consisting of layers of different semiconductors (heterostructures), with sharp interfaces, and with the conductivity controlled by the introduction of dopants. This has enabled advanced devices such as the laser diode.

The growth conditions ultimately affect the composition of the materials and the surface chemistry. These growth conditions must be maintained under precise control to yield high-quality crystals. The conditions differ between different semiconductors, and growth methods. In general, the substrate temperature is elevated to give the surface ad-atoms enough energy to migrate to an energetically favorable lattice site.

The growth methods differ in the way atoms are supplied to the growth surface, and thereby in the optimal growth temperature. In the following sections some technologies relevant for the growth of III-nitrides will be described.

6.1.1 Substrate Preparation Techniques

Although substrates are grown from a seed crystal, the requirements are different from the growth of epitaxial layers for device fabrication. It is sufficient to be able to grow a single semiconductor material, and, although preferable, selective control of carrier concentration is not always required. Since substrate growth requires large crystals to be formed, a high growth rate is desirable. It is also important to be able to grow crystals with low defect densities, and without macroscopic defects.

Two substrate growth methods were mentioned in Section 2.5: PVT and ammonothermal growth, suitable for AlN and GaN, respectively. Complementing these two methods is the HVPE growth method, capable of both AlN [174, 175] and GaN [176] growth.

HVPE has a high growth rate and has been used to grow low defect density GaN templates on sapphire [177, 178]. Also, high-quality crack-free AlN templates on sapphire have been grown [179]. HVPE can also be used to grow thicker layers, free-standing GaN templates, and boules [180]. In the HVPE reactor, group-III metals are usually supplied by flowing hot gaseous HCl over molten Al or Ga, forming GaCl or AlCl. When the hot metal-chloride gases are mixed with ammonia (NH_3), at an even higher temperature, epitaxial growth of AlN or GaN takes place. A typical GaN growth temperature is 1050-1100 °C [180]. Dopants such as Fe, Mg, or Si can be included during growth. Although the growth speed can be adjusted for growth of thin layers, and several metal sources can be used to grow subsequent layers with different alloy compositions so that device structures can be grown, HVPE growth is generally considered to be more suited for growth of thick templates and boules for substrate fabrication than for growth of device structures.

PVT is a method suitable for growth of AlN boules. AlN powder and N_2 gas is heated to about 2100 °C in a TaC or W crucible [52, 181]. AlN then crystallizes on a seed crystal in the lid of the crucible when the temperature gradient is properly adjusted [52]. Incorporation levels of C and O impurities on the order of 10^{19} cm^{-3} each were observed [52].

The ammonothermal growth of GaN can produce high quality substrates. This method utilizes a solubilizing agent or mineralizer to allow a GaN feedstock to dissolve in supercritical ammonia and then recrystalize in another part of the growth vessel, due to a temperature gradient. The process can occur under basic, acidic, or neutral conditions depending on the mineralizer used [180]. The growth takes place at 0.1-0.3 GPa, and at 500-600 °C [48]. Growth rate is relatively low, roughly 10 μm/h, but hundreds of crystals can be grown simultaneously [48].

6.1.2 Metal-Organic Chemical Vapor Deposition

The majority of epitaxial III-nitride growth is done using MOCVD. This technique allows growth on several wafers simultaneously with good uniformity, for example the CRIUS II-XL MOCVD system from Aixtron handles 19×4 inch wafers [182].

While there are slightly different designs of MOCVD systems, the basic principles are similar. A carrier gas, typically H_2 or N_2, is used to dissolve and transport a vapor of metal-organic (MO) molecules, e.g., trimethylgallium $(CH_3)_3Ga$, and triethylaluminium $(CH_3)_6Al_2$ from a solid or liquid source, to the surface of the substrate. The elevated temperature of the substrate causes the MO molecule to break apart or crack, releasing the metal atom at the surface while the CH_3 radicals are pumped away. Nitrogen is supplied from ammonia (NH_3). The ammonia also dissociates at the surface releasing nitrogen atoms that react with Ga or Al and form GaN or AlN. For dopants, silane (SiH_4) and bis(cyclopentadienyl)magnesium $[(C_5H_5)_2Mg]$ are used for (n-type) Si- and (p-type) Mg-doping, respectively.

For the growth of Mg-doped $Al_{0.85}Ga_{0.85}N$ in Paper I, a hot-wall MOCVD system was used with a growth temperature of 1100 °C. The hot-wall system was originally developed for SiC growth and allows high growth temperatures ($\leq$ 1600 °C). The term hot-wall refers to the heating of the chamber walls in addition to the substrate. This results in a more uniform temperature distribution, more efficient cracking of the precursors, and reduced substrate bowing compared to a cold-wall chamber, in which the substrate is heated only from below [183, 184].

6.1.3 Molecular Beam Epitaxy

MBE allows very rapid transitions in material composition and doping type/level and sharp interfaces. MBE growth uses pure materials and requires ultra-high vacuum. A typical base pressure in a clean system is in the low 10^{-10} Torr [185].

For III-nitride growth, nitrogen can be supplied from a plasma source or through injection of ammonia (NH_3). Our system is equipped with a plasma source. The metals are supplied from temperature controlled crucibles containing source materials. Mechanical shutters in front of the crucibles are rapidly opened and closed to turn the beam of atoms emitted from the crucibles on and off. The beam flux is controlled by the source temperature. The rapid shutter action allows for very sharp interfaces with atomic layer precision.

In growth of AlGaN compounds, the growth is typically performed under metal stable growth conditions where a film of a few monolayers of metal floats on the surface. Nitrogen atoms from the plasma source enter the metal and bond to the metals on the growth front. Since an excess of metal is present on the surface, the growth rate is controlled by the nitrogen flux from the plasma source (N-stable). The plasma is needed to activate the N_2 molecules since the growth temperature (700-800 °C) is not sufficiently large for N_2 molecules to crack at the growth surface.

6.2 Activation Annealing

Parts of the carrier gas used in MOCVD growth are incorporated in the crystal lattice. As mentioned in Section 6.1, H_2 is often used as a carrier gas and is also present in the MO precursors. Thus, H will be incorporated in MOCVD grown material. The H atoms passivate the Mg acceptors and significantly reduce the hole concentration and therefore also the p-type conductivity [12]. For MBE growth, H incorporation is much lower due to the elemental source materials used and the passivation can thus be avoided. However, atomic H can be introduced to increase the Mg incorporation [186], at the expense of passivation.

For MOCVD grown material the H that passivates the Mg acceptor atoms needs to be removed to obtain conductive material. This is achieved through high temperature annealing around 700 °C in N_2 [12, 187], which is the currently preferred method. The activation annealing can damage the p-GaN crystal surface due to dissociation of GaN at temperatures above 800-850 °C in vacuum, [188]. Therefore, care must be taken to control the annealing temperature. The segregation can be suppressed by annealing under high N_2 pressure [12, 189].

6.3 Photolithography

Conventional photolithographic processes are described in detail in most books on fabrication methods, e.g. [190]. In essence, a pattern is imaged onto a photosensitive film (photoresist) by illumination with a Hg-based UV lamp. Subsequent development of the photoresist allows the formation of a resist pattern that is used in following process steps.

Due to the wide bandgap of the III-nitrides, the UV light from the lamp is not sufficiently absorbed in the semiconductor material, thereby complicating the photolithography process. To limit the impact of this effect, exposure times should be kept short so that the exposure dose from reflections in the wafer and the mask-aligner is minimized. It is also recommended to use a chuck with a UV absorbing coating. This effect is especially noticeable with image reversal resists and if frame exposures are attempted. The unwanted exposure dose can further be reduced by altering the mask design to include more dark fields.

6.4 Dry Etching

The strong covalent bonds and chemical stability of the III-nitrides make them almost impregnable for wet-chemical etching. Dry etching techniques are instead used for the formation of mesa recesses and material removal. The dry-etch processes used for AlGaN etching in the work leading up to this thesis were based on Cl/Ar plasmas.

The optimization of process chemistry and plasma powers used is done to allow the formation of smooth and vertical facets.

The etch reactor used allows the control of two RF power sources to excite the plasma in different ways. One that couples inductively to the plasma and one that couples capacitively to the wafer table. By adjusting the power ratios, the velocity and density of ions impinging on the wafer can be adjusted. More inductively coupled power gives a more isotropic etch while a increase in the capacitively coupled power results in a more anisotropic etch. When dry-etching GaN and AlN, pits or pillars are often created at defect sites where the etch can be faster or slower than on the surrounding surface, depending on process conditions. Pillars are usually formed if the capacitive power is too large and pits if the inductive power is too large [191].

6.5 Dielectric Deposition

Dielectric materials are often used to protect the surface of semiconductors and to provide isolation, allowing the placement of metal bondpads and conductors above areas that should not be contacted. Several dielectrics and deposition methods exist. Two common dielectrics are SiO_2 and Si_3N_4. They can be deposited by methods such as sputtering, CVD, and evaporation [192].

Unfortunately p-GaN is relatively sensitive to damage by both the deposition and the subsequent removal of the dielectric. It was for instance found that the resistivity of p-GaN increased one order of magnitude when Si_3N_4 was deposited in a high-temperature (770 °C) low-pressure-CVD process. The degradation can likely be attributed to hydrogen passivation from the ammonia and the silane precursor used in the Si_3N_4 CVD deposition. Instead, the dielectric coating used in Paper V was sputtered SiO_2 which was patterned with a buffered oxide etchant.

6.6 Contact Metallization

To inject the current needed for light emitting devices, metal contacts need to be formed at the semiconductor. Preferably they should have linear current-voltage characteristics and low resistivity. Such contacts are referred to as ohmic contacts.

When a metal is deposited on a semiconductor, an energy barrier is formed at the interface. From basic theory, the barrier is caused by the difference between the work function of the metal (Φ_m) and the semiconductor (Φ_s). The work function is the difference between the Fermi-level and the vacuum level. If a metal with a suitable work function, matching the Fermi-level in the semiconductor, is used, an ohmic contact can be formed. If they differ, a depletion region is formed between the metal and the semiconductor when the Fermi levels align. At the interface between heavily doped semiconductors and metals, the depletion region is very narrow and electrons can effectively tunnel through the barrier and the contact has ohmic characteristics. If the

carrier concentration in the semiconductor is low, the formation of an ohmic contact can be quite difficult, especially if a metal with a suitable work function does not exits.

For n-doped GaN and AlN, a reactive metal such as Ti is often used. A rapid thermal annealing process is used to improve the contact quality. At the elevated temperature (800-1000 °C), the contact metal reacts with the semiconductor and the contact resistivity is reduced. It is generally believed that nitrogen vacancies are formed in the vicinity of the metal, under the formation of TiN, yielding a high electron concentration immediately below the contact, thereby forming an ohmic contact [193, 194]. Another explanation for the ohmic contact formation on n-GaN is that the work function of TiN is suitably aligned with the Fermi-level in the semiconductor. Using synchrotron radiation photoemission spectroscopy, it has been showed that the TiN formation increases the barrier height and that N vacancy formation is the cause of the ohmic behavior [195].

To protect the contact and to allow easy probing and bonding more metal layers are usually added, typically ending with Au as an upper contact layer. Some intermediate layers are used to separate the ohmic contact and the Au. A common metal stack used on n-doped AlGaN is Ti/Al/Ti/Au [193]. To reduced surface roughness, Ti/Al/Ni/Au is often used [196].

Other reactive metals such as V, forming VN, can be used and the required annealing temperature can then be reduced. In [197], the annealing temperature required for forming low resistance ohmic contacts could be reduced by 150 °C to 650 °C when using a V/Al/Pt/Au stack compared to a Ti/Al/Pt/Au. In [198], an annealing temperature of 825 °C for 30 s was found optimal with a V/Al/V/Ag metal stack on n-doped GaN and of 865 °C for n-$Al_{0.58}Ga_{0.42}N$.

For formation of contacts to p-GaN, metals with large work functions are used to reduce the height of the contact barrier, thereby creating an ohmic contact. Commonly used metals are Ni ($\Phi_{Ni} = 5.09$ eV), Pd ($\Phi_{Pd} = 5.40$ eV) and Pt ($\Phi_{Pt} = 5.66$ eV) [150, 199]. For p-GaN, the Fermi-level is near the valence band edge. The separation between the conduction band and the vacuum level is 4.1 eV [200] and the valence band lies $E_g = 3.437$ eV below the conduction band [15]. This means that a barrier of around 2 eV will be present and ohmic contacts must be formed by reducing the width of the depletion barrier with heavy p-doping near the contact. For AlN and AlGaN, the barrier is even larger. For DUV-LEDs, a thin heavily p-doped GaN layer is nearly always inserted to ease the contact formation but can degrade the surface morphology. The contacts are usually annealed for up to 10 minutes around 500 °C [199].

For similar reasons as those for using Au on the top of the n-contact metal stack, a top layer of Au is usually added on the p-contacts. The lower annealing temperature in combination with the lower reactivity of the contact metal reduces the need for several metals in the contact stack. Common choices for p-contact metallizations are Pd/Au, Ni/Au and Pt/Au.

It has also been observed that oxidation annealing of Ni/Au contacts on p-GaN can form low resistance contacts by forming NiO/Au on the p-GaN surface and the

formation of Ga vacancies at the contact interface [201–203].

The purity of the semiconductor interface is important for the contact formation. Usually organic compounds are dissolved in degreasing processes, such as ultrasonic acetone, methanol and isopropyl alcohol rinsing, prior to photolithography. Other impurities and native oxides are often removed using a acid dip immediately before depositing the contact metals. A dip of a few minutes in buffered HF, followed by rinsing in deionized water, can be used. However, care must be taken so that dielectrics or other layers in the device structure are not removed.

Chapter 7

Characterization Techniques

For characterization of semiconductor materials and devices many different techniques are used. In this chapter, some of the most important techniques used in this work, and their implementations, are discussed. Standard techniques, such as Hall, SEM, AFM, optical ellipsometry and mechanical profilometry have also been used but are not described here.

7.1   X-Ray Diffraction

X-ray diffraction (XRD) is a widely used method to study and analyze the crystalline or structural quality. The sample is illuminated with x-rays and the resulting diffraction pattern is analyzed. The fundamental principle of x-ray diffraction is similar to the optical reflections in a DBR stack. However, the x-rays are diffracted by the crystallographic planes inside the crystal, see Figure 7.1. In principle, for maximum diffraction from a set of crystal planes with a separation distance, d, the wavelength (λ) of the x-ray photons and the incidence angle, ω_i, need to satisfy the Bragg condition $m\lambda = 2d\sin(\omega_i)$, where m is an integer. That is, the optical path length experienced by photons reflected on different crystal planes must be such that the photons are in phase at the output.

Various optical components such as slits and crystal based monochromators can be used to reduce the divergence and the linewidth of the x-ray beam, thereby increasing the angular resolution of the instrument. Thus, the crystalline quality can be assessed by measuring the width of the diffraction peak. The wider this peak is, the worse is the crystalline quality. For the III-nitrides, screw and edge dislocations mostly
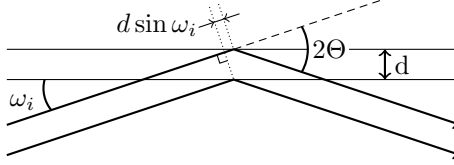
Figure 7.1: Diffraction geometry for XRD.

affect the width of the diffraction peaks of planes parallel and perpendicular to the growth plane (c-plane), respectively [204]. The full width at half maximum (FWHM) of the in-plane diffraction peaks, $\Delta\omega_s$, is readily measurable in reflection mode x-ray diffractometers. For the diffraction peaks from planes perpendicular to the surface, this type of measurement is not possible due to geometrical limitations of the XRD instrument. Although other measurement geometries can be used, the FWHM of the out-of-plane diffraction peaks, $\Delta\omega_s$, can instead be estimated from the FWHM of layers with increasing inclination to the surface normal [205]. Although the FWHM depends on several different effects it is often used to estimate the edge, ρ_e, and screw, ρ_s, type dislocation densities using the expressions [204]

$$\rho_e = \frac{\Delta\omega_e^2}{4.35 b_e^2}, \qquad \rho_s = \frac{\Delta\omega_s^2}{4.35 b_s^2}, \tag{7.1}$$

where b_e, and b_s are the lengths of the Burgers vectors associated with edge $(11\bar{2}0)$ and screw (0001) dislocations, respectively. The Burgers vector corresponds to the step required to restore the lattice after traversing around a dislocation line [206].

Since XRD allows for the examination of the crystal structure, it can also be used to determine the lattice constants of the sample. Since the lattice constants of the substrate are known and are not affected by the epitaxial layers it can be used as a reference. In Figure 7.2, a reciprocal space map of the 22.5 pair AlN/GaN DBR previously described in Section 4.4 around the $(10\bar{1}5)$ diffraction peak is shown. The peaks from the grown layers are aligned vertically, indicating that they have assumed the same in-plane lattice constant. The lattice constants of the layers are obtained by comparison with the known lattice constants of the 4H-SiC substrate, under the assumption that the tilt of the c-axis compared to the Z-axis of the XRD system is negligible, which is reasonable for substrates grown without miss-cut. For this particular DBR the lattice constants of the free-standing layers are $a_{GaN} = 3.15$ Å, $c_{GaN} = 5.20$ Å, $a_{AlN} = 3.14$ Å, and $c_{AlN} = 4.94$ Å.

Apart from the previously described measurements, XRD can also be used to measure, for instance, the periodicity of DBR and SPSL structures, and QW strain.
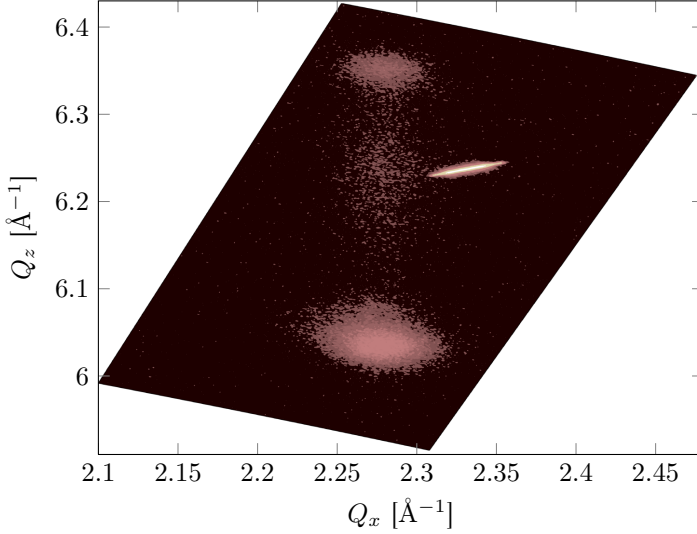
Figure 7.2: Reciprocal space map of the 22.5 pair AlN/GaN DBR described in Section 4.4, around the $(10\bar{1}5)$ reflection peak. Peak broadening is caused by a low 2Θ resolution due to the use of a $1/8°$ slit on the detector.

7.2 Raman Spectroscopy

Spectroscopical investigations of semiconductors are often desirable since they are generally nondestructive and require limited sample preparation. Raman spectroscopy is one such technique that can be used to, e.g., characterize graphene layers.

The sample is illuminated with monochromatic light, usually from a laser, and the backscattered light is analyzed. While the photon energy is mostly maintained, some photons experience an energy shift due to interaction with the optical phonons in the material. Thus, a spectroscopical analysis of the backscattered light allows the phonon spectrum of the material to be measured. The phonon spectrum is strongly linked to the properties of the crystal lattice. For instance, the phonon energy in AlN is related to the stress in the layer and the stress can, thereby, be measured using Raman spectroscopy [207].

Graphene is a single monolayer of carbon atoms with the same hexagonal structure as the individual layers in graphite. Graphene is difficult to handle and characterize since it is very thin, fragile and fairly transparent. Graphite films with two or a few layers are referred to as bi or few layer graphene. Since the electrical and optical
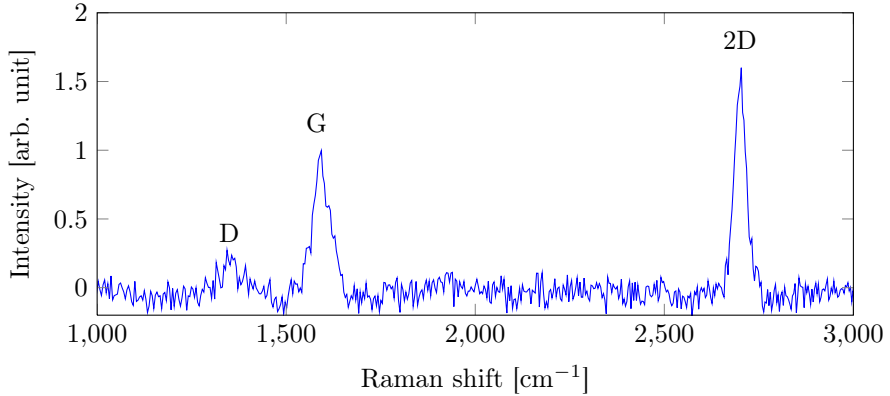
Figure 7.3: Raman spectrum of CVD grown graphene transferred to a blue LED structure. The spectrum has been normalized to the G-peak after baseline removal.

properties are different for single layer graphene and few layer graphene, a method to determine the type of graphene is needed. Although AFM can be used to separate flakes of single and bi layer graphene it is very time consuming and challenging on device structures. Alternatively, Raman spectroscopy can be used to identify single layer graphene in a non-destructive and comparatively rapid measurement [208].

To separate graphene from graphite, the intensity ratio between the so called G (1580 cm^{-1}) and 2D (2700 cm^{-1}) peaks in the Raman spectrum is measured, see figure 7.3. In defect free graphene, the 2D peak is more intense, roughly 4 times, than the G peak. In bi-layer graphene, the 2D peak becomes broader and is slightly upshifted in energy. As more layers are added, the 2D peak becomes broader and reduces in intensity relative to the G peak. After approximately five layers the Raman peaks are essentially indistinguishable from bulk graphite. In graphite, the 2D peak is separated into two broad overlapping peaks with the most intense having roughly half the intensity of the G peak. Measuring the relative intensities and shapes of these peaks can thus be used to separate, single, bi, few layer graphene, and bulk graphite in a nondestructive way [208].

Raman spectroscopy was used to verify that the method used to grow and transfer graphene for Paper V resulted in single layer graphene. The method is described in [121].

7.3 Bulk Resistivity Measurements

The transmission line method (TLM) is commonly used to measure the resistance of metal-semiconductor contacts. However, the resistivity of the bulk semiconductor between the contacts (the sheet resistivity R_{sh} [$\Omega/\square$]) is simultaneously measured. In principle, since the resistance between two contacts to a semiconductor consists of the sum of the contact resistances and the resistance in the semiconductor between the contacts, the contacts can have geometries such that the individual resistance contributions can be separated. This is possible when the resistance between contact pads of several different separation distances is measured. A full description of the TLM method can be found in [190].

In Figure 7.4a, the two most commonly used contact geometries are shown. They are the linear and circular TLM patterns. The linear pattern requires the metal pads to be placed on a mesa to restrict the current flow to the width of the contact pad. The circular pattern does not require a mesa since the contact pad geometry restricts the current flow. This simplifies the fabrication of test structures. However, the analysis of the measurement data is simpler when using the linear pattern. Although both types of TLM patterns are often used to measure the specific contact resistance, r_c [$\Omega \cdot cm^2$], the lateral geometry makes such measurements imprecise, especially for specific contact resistances lower than 1×10^{-6} $\Omega \cdot cm^2$ [190]. The method is more suited to measure the in-plane contact resistance, R_c [$\Omega \cdot cm$]. For more accurate measurement of low specific contact resistances, other device geometries such as the four-terminal Kelvin resistor can be employed [209].

For linear TLM patterns, the resistance measured between the contact pads, R_m [Ω], increases linearly with the pad separation, Δd. For contact pads with the width W [cm], R_c and R_{sh} can then be calculated by fitting $R_m W = 2R_c + R_{sh}\Delta d$ to the measured resistances. Now, given R_c and R_{sh}, the Δd_0 that satisfies $R_m W = 0$ is related to a quantity called the transfer length L_t [cm] by $L_t = -\Delta d_0/2$. The transfer length relates to the current spreading beneath the contact pad. Under the assumption of equivalent sheet resistance in the semiconductor beneath and between the contact pads, the specific contact resistance is then given by $r_c = R_{sh}L_t^2$ [190, 210].

If the same linear analysis is used for a circular pattern, with W taken as the pad circumference and Δd as the radial separation, it will give a slight error in the sheet resistance and a quite significant error in the contact resistance [210]. When using a circular transmission line method (CTLM) pattern, it has been is suggested to use

$$R_m = \frac{R_{sh}}{2\pi}\left[\ln\left(\frac{r_o}{r_i}\right) + L_t\left(\frac{1}{r_o} + \frac{1}{r_i}\right)\right] \qquad (7.2)$$

instead of a linear approximation [210]. For each pattern, r_o [cm] is the outer pad diameter and r_i [cm] is the inner pad diameter. Similarly, R_{sh} and L_t are obtained by fits to the measured resistances between several contact pads. The equation is an approximation valid when $4L_t < r_i$. The contact resistance is given by $R_c = \pi r_i R_m$

53

for the R_m corresponding to $r_o = r_i$. The bulk resistivity ρ [Ω·cm] is related to the sheet resistance by $\rho = R_{sh}t$, where t [cm] is the thickness of the semiconductor layer.

A further complication stems from the fact that contacts to p-GaN and p-AlGaN often exhibit a non-linear current-voltage dependence. This means that the measured contact resistance depends on the applied voltage. However, even with nonlinear contacts there are methods that can be used to extract some information on contact and sheet resistances [211–213]. By performing the measurement at several applied voltages it has been observed that the extracted sheet resistance stabilizes at high voltages where the impact of the nonlinear contact is reduced [211].

The current-voltage-curves in Figure 7.4b are from a CTLM measurement on p-GaN using Pd/Au contacts before contact annealing. The contacts are clearly nonlinear. In Figure 7.4c, the average resistance for each of the examined contacts is shown, and a least squares fit using Eq. 7.2 is included. The fit resulted in a resistivity of 2.1 Ω·cm for the p-GaN layer. In Figure 7.4d, the dependence of the extracted resistivity on the method used to determine R_m is shown. The resistance and the differential resistance at each bias point was used as R_m to calculate the p-GaN resistivity, which is plotted as the solid and dashed curves, respectively. After annealing the contacts were more linear and the measured resistivity was 1.7 Ω, indicated by the black line. The resistivities extracted from the resistance and the differential resistance methods were more consistent. Thus, when extracting the sheet resistance, a more accurate value is obtained if the influence of the nonlinear contact is reduced by using the differential resistance at large applied voltages. This technique was used to extract a resistivity of 7 kΩ·cm for Mg-doped Al$_{0.85}$Ga$_{0.15}$N grown by hot-wall MOCVD (Paper I).
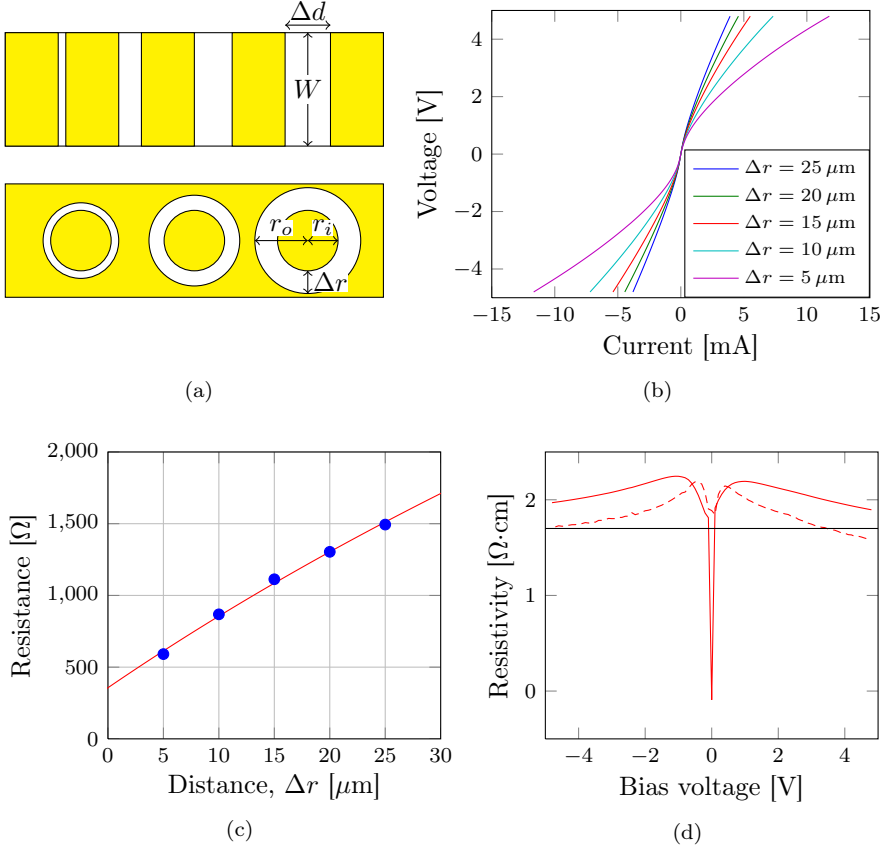
Figure 7.4: (a) The two most common pad layouts for TLM measurements: rectangular (TLM) and circular (CTLM) patterns, above and below, respectively. (b) Current-voltage curves from CTLM measurements on a 765 nm thick p-GaN layer using Pd/Au contacts before contact annealing. The CTLM pattern has an inner radius of 80 μm and a separation to the outer pad of $\Delta r = 5, 10, 15, 20, 25$ μm. (c) Average resistance between pads in the CTLM pattern with different separation. The red curve is a least square fit of Eq. 7.2. (d) The resistivity calculated from the resistance and differential resistance at each applied voltage of the current-voltage scans, solid and dashed curves, respectively. After contact annealing, a sheet resistivity of 1.7 Ω·cm was measured, indicated by the black line.

7.4 Electrical Characterization of Transparent Electrodes

For electrical characterization of electrodes for use as current spreaders and transparent contacts, there are three contributions to the overall resistance. They are the resistance between the metal contact and the transparent electrode, the sheet-resistance of the electrode, and the contact resistance between the electrode and the semiconductor. It is also important that the contact can withstand the current densities required for operation.

The resistance of metal contacts to the transparent electrode and the lateral sheet resistance inside the electrode can be measured using the TLM structures described in Section 7.3, if the transparent electrode material is deposited on an insulating substrate. In principle, the contact resistance between the transparent electrode and the semiconductor can also be characterized using the TLM method, if the transparent electrode is patterned so that it replaces the metal contact pads. That is, if the sheet resistance in the electrode is sufficiently low so that the measured resistance does not critically depend on where the probe needles are placed on the transparent electrodes. The transparent electrodes must also be sufficiently mechanically stable, so that they are not damaged by the probe needles. When these conditions are unfulfilled it is common to add a metal pad above the electrode to ease the contacting of the electrode. However, when characterizing thin electrodes, as are needed in blue VCSELs, the metal pads can accidentally contact the semiconductor through voids in the transparent electrode. The metal can also alter the properties of the transparent electrode.

To avoid such problems, a test structure with a dielectric layer separating the metal-transparent electrode interface from the transparent electrode-semiconductor interface was used, see Figure 7.5. The contact area between the transparent electrode and the semiconductor is defined by a circular aperture in the dielectric. A conventional contact metallization, with known current-voltage characteristics, is used as the opposing contact. Comparison of the current passing through contacts with different aperture radii can then be used to determine the specific contact resistance if the current is limited by the contact area. However, if the current is limited by the contact circumference the specific contact resistance cannot readily be extracted since current crowding limits the actual contact area to the outer parts of the contact.

This method was used in Paper V to characterize graphene for use as a transparent electrode in blue VCSELs. Contacts were formed on both p-GaN and blue LED structures. Unfortunately, due to the comparatively large p-GaN resistivity, current crowding effects were observed. On the LED structures, the current scaled with the contact area, which can be attributed to the lower resistivity of the n-GaN below the pn-junction. However, the LED structure contains a pn-junction which makes it impossible to examine the transparent contact under reverse bias and introduces an extra forward voltage drop under forward bias. With a thicker or lower resistivity p-GaN layer, the sheet resistance should be lower and the current crowding be reduced, potentially enough for the current to scale with the contact area.
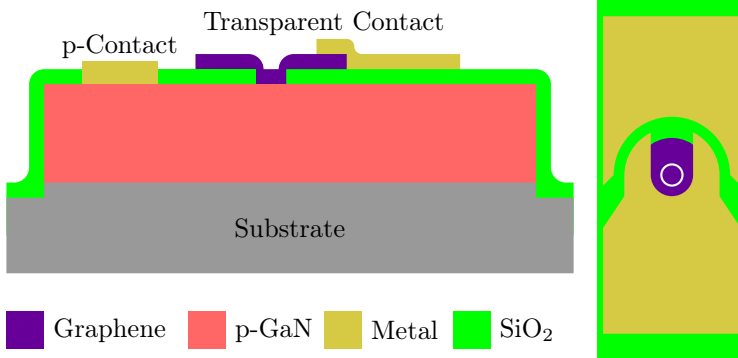
56

Figure 7.5: The test structure used to evaluate transparent contacts on p-GaN in Paper V. Left: side view, and right: top view. The white circle, in the top view, indicates the dielectric aperture. A similar structure was used for contact evaluation on LED structures.

7.5 Spectral Reflectance Measurements

The spectral reflectance measurement shown in Figure 4.3a was performed using a white light reflectance system. The light from a xenon lamp (Thorlabs OSL1-EC) was collected into a bifurcated reflection-probe with sig bundled illumination and one detection fibers (Filmetrics FO-RP1-NIR-1.3). A sample stage (Filmetrics SS-3) was used to align the sample with the reflection probe. The reflected light was collected in the center core of the reflection probe and was led to a fiber coupled monochromator (Avaspec 3648). The system has a spot size of approximately 1×1 mm and covers the wavelength range 350-800 nm.

Since the output power of the lamp can vary it is necessary to calibrate against a reference sample, with known reflectivity (R_r), for each measurement, after allowing the lamp to stabilize. After measuring the intensity of light reflected in the sample (I_s), the reference (I_r) and the system response to a scan without reflecting sample (I_d), the sample reflectivity (R_s) is given by:

$$R_s = R_r \frac{I_s - I_d}{I_r - I_d}, \tag{7.3}$$

assuming a linear system response. All parameters above are functions of the wavelength, λ.

Another method that can be used to measure the spectral reflectance is the V-W method. The method is in principle similar to the previously described method. However, it has the advantage that no reference reflector is needed. Instead two

different optical configurations, referred to as the V and W configuration, are used to measure the system response corresponding to 100% reflection and the sample intensity, respectively. The drawback is that the method requires the light incident on the sample to have a slight angle with respect to the surface normal and that the sample must be sufficiently large and uniform (approximately 4×4 cm) for the two reflections needed in the W configuration [214, 215].

For increased measurement accuracy the cavity phase-shift (CAPS) method, which allows for a measurement accuracy of 0.01%, can be used [216, 217]. In the CAPS method, two mirrors are used to form a resonator. The phase delay experienced by an amplitude modulated laser beam as it passes through the resonator is used to measure the Q-factor of the resonator. Since the combined loss in both mirrors is measured, one of the mirrors has to have a known reflectance. However, this reference reflectance can be determined by measuring the three possible resonators formed using three mirrors with unknown reflectance. The CAPS method is in principle similar to the waveguide loss measurement method presented in Section 7.7. The difference is that the phase delay caused by the photon lifetime in the resonator is used to calculate the loss instead of the Fabry-Pérot (FP) resonance spectrum.

7.6   Intersubband Absorption Measurements

In Paper II, the temperature dependence of the ISB-transition energy in GaN/AlN QWs was measured. The measurement was based on Fourier transform infrared (FTIR) spectroscopy. The sample was cleaved and polished into a multipass geometry with $45°$ beveled input and output facets, see Figure 7.6. The multipass structure is required due to the selection rules of the ISB transitions where only photons with E-field perpendicular to the QWs can be absorbed [218, 219]. The sample was heated using a resistive heater integrated in the sample holder. The sample holder was built to fit inside the sample compartment of a Bruker IFS 55 FTIR spectrometer, see Figure 7.7. A thermo-electrically cooled InGaAs detector with built-in amplification was used to detect the light transmitted through the sample. A polarizer was used to select the polarization.

In FTIR measurements, a polarizing beamsplitter with a movable mirror is used to spectrally modulate light from a white light source. The modulated light is transmitted through the sample and onto a photodetector. By Fourier transforming the detected signal with respect to the mirror position, the energy dependence of the transmission through the sample is obtained. To extract the absorption in a sample, a similar but non-absorbing dummy sample is needed as a reference, so that the intensity variation of the system can be accounted for in the calculation of the absorption.
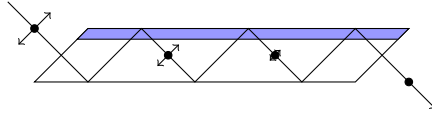
Figure 7.6: Side view of the multipass geometry. The incoming light is reflected on the sidewalls and passes through the QW stack (blue) several times. Photons polarized parallel to the plane of the QWs (dots) are fully transmitted, while some of the photons with perpendicular polarization (arrows) are absorbed in each pass through the QWs.
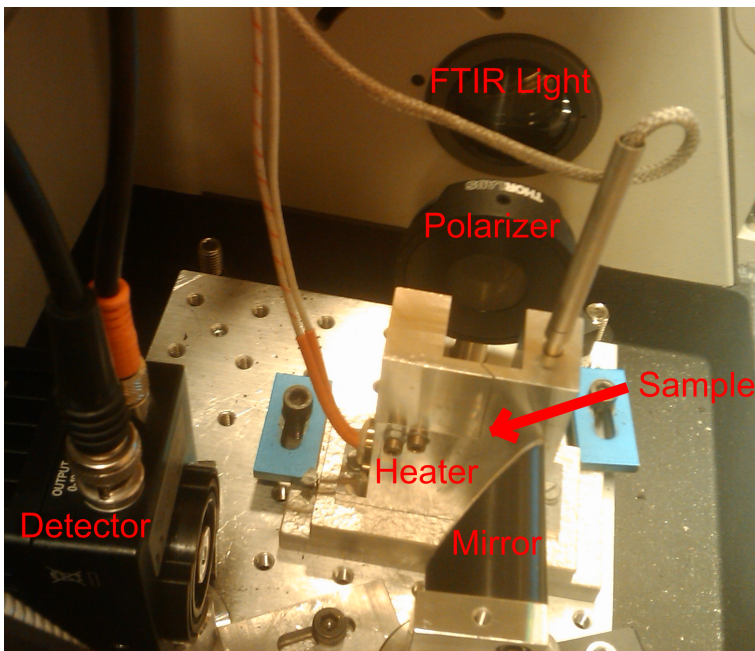
Figure 7.7: A setup for temperature dependent absorption measurements. With a temperature controller, the temperature of the aluminium sample holder can be adjusted between room temperature and 400 °C. The light from the FTIR window passes through a polarizer and is focused onto the sample. After multiple internal reflections in the sample, the transmitted light is collected and focused onto a thermo-electrically cooled InGaAs detector with the help of a concave mirror.

7.7 Waveguide Loss and Mode Characterization

To enable experimental verification of the waveguide designs proposed in Papers III and IV, a waveguide characterization system has been constructed. A schematic of the setup is shown in Figure 7.8a. Light from an external source is injected into one end of the waveguide, and the light transmitted through the waveguide is collected and analyzed. A 3 dB coupler is used so that light from both a wavelength tunable external-cavity fiber-coupled laser at 1.55 μm and a red laser (635 nm) can be injected. The light passes through a polarization controller and is injected into the waveguide by a lensed fiber. The position of the fiber is precisely controlled with a piezoelectric xyz-translator. The red laser is used for coarse alignment so that the coupling into the waveguide can be observed with an ordinary microscope, see Figure 7.8b. The nearfield at the output facet is collected with a lens and imaged onto a NIR-camera for monitoring the waveguide modes or a photodetector for loss measurements. A polarizer is placed before the camera to verify the polarization state selected by the polarization controller.

Although it is possible to directly measure the intensity of the light transmitted through the waveguide, and relate it to the losses, it is not recommendable since the intensity is highly depended on the amount of injected light, and thereby the alignment of the lensed fiber. Alternatively, the loss can be measured by observing the intensity oscillations caused by the FP resonances in the resonator formed by the waveguide end facets as the wavelength of the laser is varied. The maximum (I_{max}) and minimum (I_{min}) intensity values are used to determine the finesse of the resonator [220]:

$$F = \frac{\pi}{2}\sqrt{\frac{I_{max}}{I_{min}} - 1}. \tag{7.4}$$

The finesse is related to the waveguide loss α_{wg} by [220]:

$$F = \frac{\pi \exp\left(-\frac{L}{2}\left(\alpha_{wg} + \frac{1}{2L}\ln\left(\frac{1}{R_1 R_2}\right)\right)\right)}{1 - \exp\left(-L\left(\alpha_{wg} + \frac{1}{2L}\ln\left(\frac{1}{R_1 R_2}\right)\right)\right)} \tag{7.5}$$

where L is the length of the waveguide and R_1, R_2 are the reflectivities of the two end facets. Under the assumption of equal reflectivity at both facets, it is possible to determine both the waveguide loss and the facet reflectivity if two equivalent waveguides with different lengths are used.

(a)

(b)

(c)

(d)

(e)
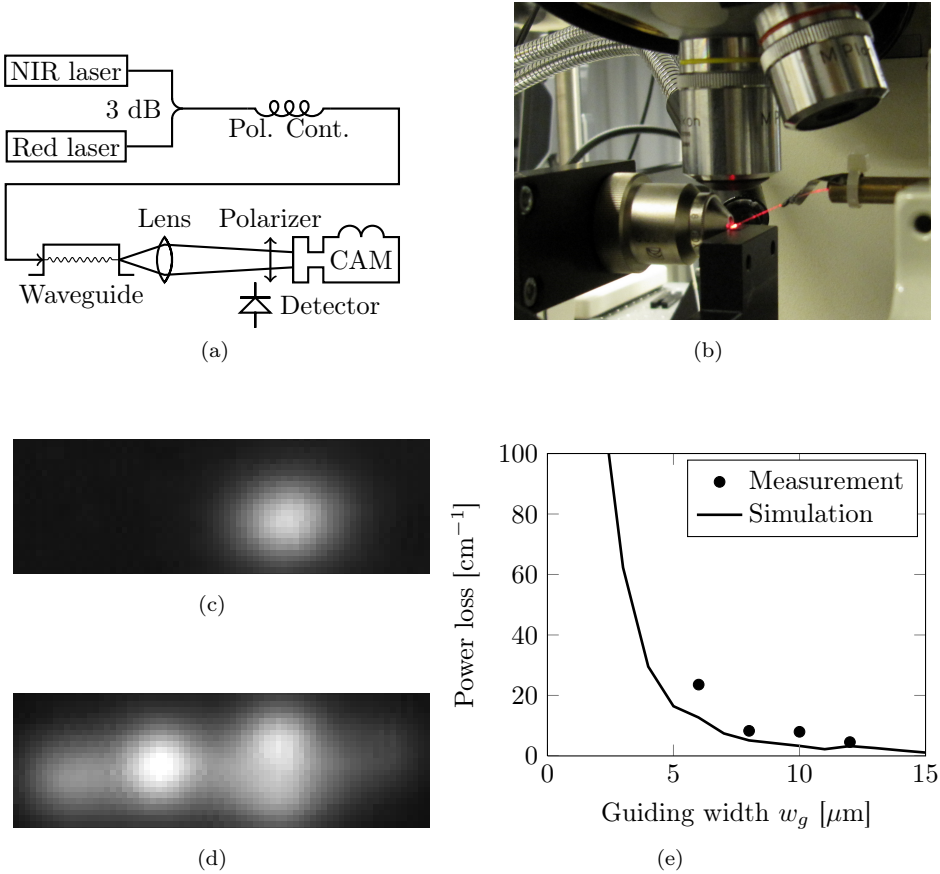
Figure 7.8: (a) The waveguide characterization setup. (b) View showing the optics used to inject and extract light from the waveguide in the center of the image, the lens for imaging the waveguide end facet to the left, the microscope ocular used to view the alignment above, and the lensed fiber excited with the red laser to the right. (c) and (d) Nearfield of the TM- and TE-polarized modes, respectively, for a waveguide with the metal-contact design from Paper III. Note that, as predicted by the simulations, the TM mode is only transmitted through the right side of the waveguide, and not in the area beneath the metal contact. (e) Simulated metal induced loss and measured total loss for the TM-polarized mode of waveguides fabricated in a 2.5 μm thick GaN template on a sapphire substrate (Figure 7.9), using the design from Paper III.
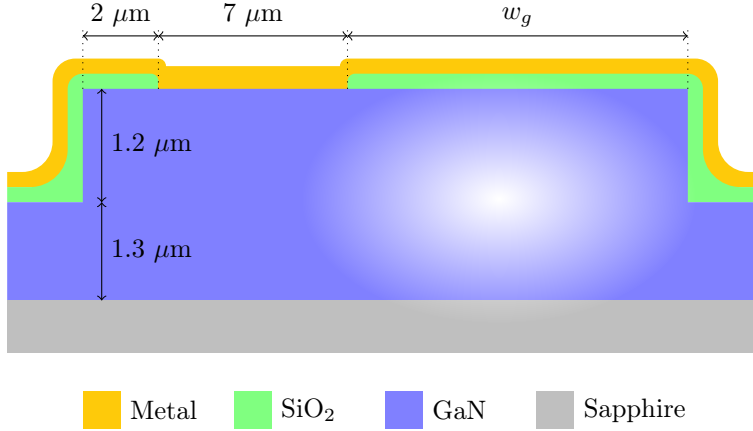
Figure 7.9: To test the waveguide design proposed in Paper III, waveguides in a 2.5 μm thick GaN template on a sapphire substrate were fabricated. The width of the guiding region, beneath the label w_g, was varied. The white ellipse indicates the area where the low loss TM polarized mode is guided.

To verify the waveguide design proposed in Paper III, waveguides were fabricated in a 2.5 μm thick GaN template on a sapphire substrate, see Figure 7.9. The end facets were formed by dry etching. The partial width of the waveguide ridge on the right side of the metal contact, here referred to as the guiding width, w_g, was varied. In Figures 7.8c and 7.8d, nearfield images of the guided TM and TE modes are shown. A comparison between the relative position of the TM and TE polarized modes serves as a verification that the TM mode only exists in the area to the right of the metal contact, as suggested by the simulations. In Figure 7.8e, the losses measured for the TM mode of 300 μm long waveguides with different guiding width are compared with a simulation of the metal-induced losses. The measurement was based on the relative intensities of the FP resonances in the waveguide. Based on the effective mode index, $n_{eff} = 2.28$, a reflectivity of 15% was assumed for the dry etched end facets when calculating the waveguide loss using Eq. 7.5. The slightly larger measured losses compared to those from the simulations can be explained by considering that the simulations only take the loss caused by the contact metallization into consideration and ignores other loss sources such as scattering at sidewall roughness.

Chapter 8

Future Outlook

Despite the large development that has occurred during the last few years, the full potential of the III-nitrides remains to be explored. Probably most exciting for the nearest future is the increasing availability of high-quality native and non-polar substrates with low defect densities, that has started to enable efficient DUV-LEDs, improve the efficiency of blue LEDs and LDs, and extend the wavelength range into the green. A remaining challenge is the difficulty of obtaining high p-type conductivity, which sofar remains modest despite significant research and development efforts. Some potential future development possibilities, related to the device technologies studied in this thesis, will be discussed in this chapter.

8.1 Deep Ultraviolet Emitters

As was mentioned in Section 3.4, the record EQE (10.4%) for DUV-LEDs is for a device grown on sapphire substrate [6]. The UV transparent substrate allows for high LEE (30%), especially when combined with a reflective p-contact. It was observed that the IQE increased as the TDD decreased. If the high LEE could be achieved for devices grown on low TDD AlN substrates with IQE of 70% [72], an EQE of 21% can be expected. Increasing the LEE up to 45% as expected in [78] would then give 31% EQE. However, when estimating the currently obtained IQEs based on the EQEs and LEEs in the references the IQEs are in the range of 30-35% and not 70% [6, 72]. The LEE for devices on AlN substrates could be improved by using high purity HVPE-AlN with a lower defect related absorption of 6.6 cm^{-1} at 265 nm compared to the 35 cm^{-1} for PVT-AlN [72, 221]. LEDs on HVPE-AlN with an EQE of 2.4% have been

demonstrated [81]. This could be improved by wafer thinning and encapsulation in a low index material similar to that used in [72].

High purity transparent AlN substrates could also allow the use of laser lift-off to remove the epitaxial structure for substrate reuse. The extraction efficiency would then potentially increase significantly, in a manner similar to that of thin-GaN blue LEDs grown on sapphire substrates where a LEE > 80% was achieved [4]. With high purity substrates, it might also be possible to introduce doping to obtain n-type conductivity. This could allow the use of backside contacts for LED and LDs which would simplify device processing and improve current spreading compared to the currently favored lateral contact geometry.

A further advantage for growth on high quality native substrates is the possibility to use non- or semi-polar orientations. Non-polar device structures might enable larger efficiencies, due to the increased electron-hole overlap and the possibility of using wider QWs. Further research is warranted to determine the optimal growth plane and device structure for DUV-LEDs.

The difficulty of obtaining high p-type conductivity is a remaining hurdle that reduces the power efficiency of DUV emitters. Much of the effort is directed to the search of a better dopant. However, the best results so far are obtained using Mg, as was done for $Al_{0.85}Ga_{0.15}N$ in Paper I. Other dopants such as Be and MgO complexes have been suggested to reduce the ionization energy and might lead to improved conductivity. Another method with potential to increase the conductivity is to utilize the internal polarization fields to reduce the ionization energy of the Mg acceptors. This has been used [37, 222–224] to increase the p-type conductivity in various AlGaN structures.

A highly exploratory technique that could alleviate the p-doping problem is the formation of a tunnel junction assisted by the polarization fields in a thin highly strained layer at the interface between the p-region and an added n-type contact layer; the purpose of the layer being to align the valence- and conduction-band on each side of the layer so that tunneling through this junction becomes possible. Such a tunnel junction has been demonstrated in GaN using an $In_{0.33}Ga_{0.67}N$ layer sandwiched between p- and n-type GaN layers [225], markedly increasing reverse and moderately increasing forward current density compared to a degenerately doped p+/n+ GaN junction. Such a junction could be used to reduce the resistive losses in an AlGaN-based LD design, where a thick n-doped waveguide cladding layer could be used on both sides of the gain region. The polarization enhanced tunnel junction is then used to connect one of the n-doped cladding layers to a thin p-doped hole injector layer immediately before the gain region. However, for the formation of an efficient tunnel junction, a hole concentrations larger than what is currently demonstrated in high Al mole fraction AlGaN is likely required, despite the assistance from the high strain fields.

Still, with the currently achieved power efficiencies, > 5% [6], and output powers, > 60 mW [72], DUV-LEDs are already a viable alternative for replacing Hg-based gas

discharge lamps for applications where low turn-on delay, long device lifetime, and/or physical robustness are more important than maximizing power efficiency.

8.2 Blue Vertical Cavity Surface Emitting Lasers

Due to intense development efforts, several research groups have in the last few years demonstrated GaN-based blue VCSELs, with the best devices approaching mW power levels for CW lasing at RT. With further developments, an output power of a few mW, sufficient for several applications, is likely.

The devices with the best performance have both top and bottom dielectric DBRs. Since these structures require complicated substrate removal, wafer scale processing with high yield is a challenge. Thus, devices with an epitaxial bottom DBR would be preferred. However, currently the performance of such hybrid devices is inferior to those with double dielectric DBRs. For VCSELs with a bottom AlN/GaN DBR, the lower performance could be attributed to large dislocation density in the active region. For the VCSEL with a lattice-matched bottom AlInN/GaN DBR, the performance is even worse. This is attributed to a low top dielectric DBR reflectivity of 98.4% and an unnecessarily thick ($\lambda/4$) and incorrectly placed ITO layer [96]. If these and other design issues are addressed, the performance should increase significantly.

So far no VCSELs have employed a conductive bottom DBRs. Although it is difficult to obtain conductivity in AlN, a conductive AlN/GaN DBR has been demonstrated [136]. Lattice matched AlInN/GaN doped with Si could potentially have lower resistivity, since both GaN and AlInN are intrinsically n-type. Recently, p-type AlInN was demonstrated [226] which could enable p-type DBRs, and even fully epitaxial blue VCSELs.

It should be noted that most of the blue VCSELs use a dielectric aperture to confine the current to the center of the device. Such structures have a tendency to be anti-guided [99], resulting in increased optical loss that can be reduced if a structure providing index guiding is used. It was demonstrated that RIE treatment of p-GaN could be used for current confinement in a planar structure [96]. If the RIE treatment is combined with surface patterning, an index guided structure could be realized. This could be made using dry-etching of the p-GaN, or preferably in combination with the patterning of a contact resistance reducing interlayer, for instance, a thin InGaN [110] or NiO [109] layer. For blue VCSELs, a 2 nm p^+-InGaN layer has been used to improve the p-contact resistance [95].

Finally, it might be beneficial to move away from the optically absorbing In-based TCOs that are used to contact the p-GaN surface in the center of the devices. The possibility to use metal-free graphene was examined in Paper V. Although the contacts were not able to withstand the current densities required in present blue VCSELs, both contact resistance and reliability could likely be improved using methods suggested in the paper and in Section 4.3.

8.3   Quantum Cascade Lasers

The demonstration of an AlGaN-based QCL still lies in the future. One problem hindering this is the difficulty in forming a low-loss waveguide that also allows for current injection. The designs presented in Papers III and IV might provide sufficiently low loss for lasing to occur. There are also other problems related to QCLs in the III-nitrides, for instance the large defect density and risk of crack formation due to growth on non-native substrates, such as sapphire. The optimal active region design for high gain is also an open question, where the polarization fields for growth on the c-plane complicate matters.

Many of the growth and material related issues can hopefully be resolved by growth on high quality AlN substrates. This would also enable growth on non-polar planes which could simplify the design of the active region. The suggested waveguide designs (Papers III and IV) are compatible with bulk AlN substrates. Growth on AlN will compressively strain the active region and, thereby, reduce the risk of cracking.

Although PL induced spontaneous ISB emission has been demonstrated [227–229], and a gain region designs have been proposed in Paper III and [230], there has been no demonstration of NIR EL. Such a demonstration would be the logical next step towards a NIR AlN/GaN QCL, and would provide data to refine the design and the theoretical models. The spontaneous ISB emission rate in a QCL is very low. Approximately one in a million of the transitions between the upper and lower laser level results in the emission of a photon [229, 231]. This makes detection of spontaneous emission difficult. Although significant stimulated emission typically requires conditions close to lasing, it can potentially be measured even if such conditions cannot be obtained. This could be done by using a setup similar to that for measuring waveguides losses, presented in Section 7.7, to measure the loss reduction (gain) when current is driven through the QCL stack. The measurement of gain in this manner could also be used to strengthen the validity of the EL results for the AlN/GaN THz-QCL presented in [155].

Chapter 9

Summary of Papers

Paper I

The resistivity of Mg-doped $Al_{0.85}Ga_{0.15}N$ grown by hot-wall MOCVD on an AlN template on SiC is measured to be 7 kΩ·cm. With an estimated mobility of 2 $cm^2/(V·s)$, the corresponding carrier concentration is $\approx 10^{14}$ cm^{-3}. Given the large ionization energy of the Mg-dopant at this alloy composition, a hole concentration around $\approx 1 \cdot 10^{13}$ cm^{-3} is expected with the used acceptor concentration of $2 \cdot 10^{19}$ cm^{-3}.

Contributions: I designed and fabricated the test structures, did the measurements and data analysis to extract the resistivity, and took part in writing the paper. The epitaxial layers were grown by collaborators at Linköping University.

Paper II

The temperature stability of ISB transitions in AlN/GaN multiple QW structures absorbing around 700 meV is examined at temperatures up to 400 °C. A physical model is used to explain the transition energy shift. The transition energy is found to be dependent only weakly on temperature, with a red-shift of 15 μeV/K (38 pm/K). This suggests e.g. that AlGaN-based QCLs for telecom applications could operate without active temperature control.

Contributions: I proposed the experiment, developed the sample preparation technique, designed and implemented the measurement setup, led the measurements, and wrote the experimental part of the paper. The theoretical analysis was performed by Dr. K. Berland at the Bionano Systems Laboratory at MC2. The epitaxial structures were

provided by the group of Professor Thorvald Andersson at the Microwave Electronics Laboratory at MC2.

Paper III

In this paper we propose a waveguide design for III-nitride based QCLs designed for operation at telecom wavelengths. The optical mode is vertically confined by SiO_2 above and sapphire below, and horizontally confined by a ridge structure and the metal contact used for current injection into the waveguide. The waveguide properties are examined using finite element simulations while varying the most critical parameters. It is shown that single-mode operation is possible with a low metal-induced loss of 6.1 cm^{-1} for the fundamental mode with a mode confinement of 52%.

Contributions: I proposed the waveguide design, performed the simulations, and wrote the paper.

Paper IV

In this paper a second improved waveguide design for AlGaN-based QCLs at telecom wavelengths is proposed and analyzed. The optical mode is confined vertically by a lower AlN cladding and an upper conductive ZnO cladding used for current injection, and horizontally by a ridge structure. Finite element simulations were again used to examine the waveguide characteristics, accounting for both refractive index anisotropy and free carrier absorption. The design was evaluated with material compositions appropriate for AlGaN-based QCLs. The most promising waveguide design was examined in greater detail. The design was found to provide a mode confinement of 40% and exhibiting a modal loss of 39 cm^{-1}.

Contributions: I proposed the waveguide design, performed the simulations, and wrote the paper.

Paper V

In this paper we examine the use of transferred metal-free graphene as a transparent electrode on GaN-based light emitters. Although the reliability was found to be poor, bi-layer graphene was able to momentarily sustain current densities close to the threshold current density of state-of-the-art GaN-based VCSELs.

Contributions: I designed the test structures, fabricated the devices, performed the measurements and data analysis, and wrote the paper. The expitaxial structures used in the experiment were provided by the group of Professor N. Grandjean at EPFL, Lausanne, Switzerland. The graphene layers were grown and transferred to the devices by Dr. J. Sun at the Quantum Device Physics Laboratory at MC2.

References

[1] S. Nakamura, T. Mukai, and M. Senoh, "Candela-class high-brightness InGaN/AlGaN double-heterostructure blue-light-emitting diodes," *Applied Physics Letters*, 64(13):1687–1689, 1994. `doi:10.1063/1.111832`.

[2] European Commission, "Frequently asked questions on the regulation phasing out conventional incandescent bulbs," `http://ec.europa.eu/energy/lumen/doc/full_faq-en.pdf`, 2009. Last checked: 2011-01-06.

[3] J. Harpe and M. van Wichen, "Philips creates the world's most energy-efficient warm white led lamp," Online: `http://www.newscenter.philips.com/main/standard/news/press/2013/20130411-philips-creates-the-world-s-most-energy-efficient-warm-white-led-lamp.wpd#.UWxORNcavDM`, 2013. Last checked: 2013-04-15.

[4] A. Laubsch, M. Sabathil, J. Baur, M. Peter, and B. Hahn, "High-power and high-efficiency InGaN-based light emitters," *Electron Devices, IEEE Transactions on*, 57(1):79 –87, 2010. `doi:10.1109/TED.2009.2035538`.

[5] Y. Taniyasu, M. Kasu, and T. Makimoto, "An aluminium nitride light-emitting diode with a wavelength of 210 nanometres," *Nature*, 441(7091):325–328, 2006. `doi:10.1038/nature04760`.

[6] M. Shatalov, W. Sun, A. Lunev, X. Hu, A. Dobrinsky, Y. Bilenko, J. Yang, M. Shur, R. Gaska, C. Moe, G. Garrett, and M. Wraback, "AlGaN deep-ultraviolet light-emitting diodes with external quantum efficiency above 10%," *Applied Physics Express*, 5(8):082101, 2012. `doi:10.1143/APEX.5.082101`.

[7] H. Yoshida, Y. Yamashita, M. Kuwabara, and H. Kan, "Demonstration of an ultraviolet 336 nm AlGaN multiple-quantum-well laser diode," *Applied Physics Letters*, 93(24):241106, 2008. `doi:10.1063/1.3050539`.

[8] D. Kasahara, D. Morita, T. Kosugi, K. Nakagawa, J. Kawamata, Y. Higuchi, H. Matsumura, and T. Mukai, "Demonstration of blue and green GaN-based vertical-cavity surface-emitting lasers by current injection at room temperature," *Applied Physics Express*, 4(7):072103, 2011. `doi:10.1143/APEX.4.072103`.

[9] O. Cathabard, R. Teissier, J. Devenson, J. C. Moreno, and A. N. Baranov, "Quantum cascade lasers emitting near 2.6 μm," *Applied Physics Letters*, 96(14):141110, 2010. `doi:10.1063/1.3385778`.

[10] E. F. Shubert. *Light-Emitting Devices*. Cambridge University Press, second edition, 2006.

[11] H. Amano, M. Kito, K. Hiramatsu, and I. Akasaki, "P-type conduction in Mg-doped GaN treated with low-energy electron beam irradiation (LEEBI)," *Japanese Journal of Applied Physics*, 28:L2112–L2114, 1989. `doi:10.1143/JJAP.28.L2112`.

[12] S. Nakamura, N. Iwasa, M. Senoh, and T. Mukai, "Hole compensation mechanism of p-type GaN films," *Japanese Journal of Applied Physics*, 31:1258–1266, 1992. `doi:10.1143/JJAP.31.1258`.

[13] S. Nakamura, M. Senoh, S. Nagahama, N. Iwasa, T. Yamada, T. Matsushita, H. Kiyoku, and Y. Sugimoto, "InGaN-based multi-quantum-well-structure laser diodes," *Japanese Journal of Applied Physics*, 35:L74–L76, 1996. `doi:10.1143/JJAP.35.L74`.

[14] N. A. Sanford, L. H. Robins, A. V. Davydov, A. Shapiro, D. V. Tsvetkov, A. V. Dmitriev, S. Keller, U. K. Mishra, and S. P. DenBaars, "Refractive index study of $Al_xGa_{1-x}N$ films grown on sapphire substrates," *Journal of Applied Physics*, 94(5):2980–2991, 2003. `doi:10.1063/1.1598276`.

[15] I. Vurgaftman and J. R. Meyer. *Nitride Semiconductor Devices*, chapter 2 Electron Bandstructure Parameters, pages 13–48. Wiley-VCH Verlag, 2007.

[16] L. Liu and J. H. Edgar, "Substrates for gallium nitride epitaxy," *Materials Science and Engineering: R: Reports*, 37(3):61 – 127, 2002. `doi:10.1016/S0927-796X(02)00008-6`.

[17] R. Butté, J.-F. Carlin, E. Feltin, M. Gonschorek, S. Nicolay, G. Christmann, D. Simeonov, A. Castiglia, J. Dorsaz, H. J. Buehlmann, S. Christopoulos, G. B. H. von Högersthal, A. J. D. Grundy, M. Mosca, C. Pinquier, M. A. Py, F. Demangeot, J. Frandon, P. G. Lagoudakis, J. J. Baumberg, and N. Grandjean, "Current status of AlInN layers lattice-matched to GaN for photonics and electronics," *Journal of Physics D: Applied Physics*, 40(20):6328, 2007. `doi:10.1088/0022-3727/40/20/S16`.

[18] W. Scheibenzuber, U. Schwarz, R. Veprek, B. Witzigmann, and A. Hangleiter, "Optical anisotropy in semipolar (Al,In)GaN laser waveguides," *Physica Status Solidi (c)*, 7(7-8):1925–1927, 2010. `doi:10.1002/pssc.200983646`.

[19] C.-Y. Huang, A. Tyagi, Y.-D. Lin, M. T. Hardy, P. S. Hsu, K. Fujito, J.-S. Ha, H. Ohta, J. S. Speck, S. P. DenBaars, and S. Nakamura, "Propagation of spontaneous emission in birefringent m-axis oriented semipolar $(11\bar{2}2)$ (Al,In,Ga)N waveguide structures," *Japanese Journal of Applied Physics*, 49(1):010207, 2010. `doi:10.1143/JJAP.49.010207`.

[20] C. Holder, J. S. Speck, S. P. DenBaars, S. Nakamura, and D. Feezell, "Demonstration of nonpolar GaN-based vertical-cavity surface-emitting lasers," *Applied Physics Express*, 5(9):092104, 2012. `doi:10.1143/APEX.5.092104`.

[21] R. Goldhahn, C. Buchheim, P. Schley, A. T. Winzer, and H. Wenzel. *Nitride Semiconductor Devices*, chapter 5 Optical Constants of Bulk Nitrides, pages 95–115. Wiley-VCH Verlag, 2007.

[22] Á. Szabó, N. T. Son, E. Janzén, and A. Gali, "Group-II acceptors in wurtzite AlN: A screened hybrid density functional study," *Applied Physics Letters*, 96(19):192110, 2010. `doi:10.1063/1.3429086`.

[23] M. Nagamori, S. Ito, H. Saito, K. Shiojima, S. Yamada, N. Shibata, and M. Kuzuhara, "Optimum rapid thermal activation of Mg-doped p-type GaN," *Japanese Journal of Applied Physics*, 47(4):2865–2867, 2008. `doi:10.1143/JJAP.47.2865`.

[24] M. L. Nakarmi, N. Nepal, C. Ugolini, T. M. Altahtamouni, J. Y. Lin, and H. X. Jiang, "Correlation between optical and electrical properties of Mg-doped AlN epilayers," *Applied Physics Letters*, 89(15):152120, 2006. `doi:10.1063/1.2362582`.

[25] W. Götz, N. M. Johnson, C. Chen, H. Liu, C. Kuo, and W. Imler, "Activation energies of Si donors in GaN," *Applied Physics Letters*, 68(22):3144–3146, 1996. `doi:10.1063/1.115805`.

[26] M. L. Nakarmi, K. H. Kim, K. Zhu, J. Y. Lin, and H. X. Jiang, "Transport properties of highly conductive n-type Al-rich $Al_xGa_{1-x}N$ ($x \geq 0.7$)," *Applied Physics Letters*, 85(17):3769–3771, 2004. `doi:10.1063/1.1809272`.

[27] F. Bernardini and V. Fiorentini, "Macroscopic polarization and band offsets at nitride heterojunctions," *Physical Review B*, 57(16):R9427–R9430, 1998. `doi:10.1103/PhysRevB.57.R9427`.

[28] J. Zhang, H. Zhao, and N. Tansu, "Effect of crystal-field split-off hole and heavy-hole bands crossover on gain characteristics of high Al-content AlGaN quantum well lasers," *Applied Physics Letters*, 97(11):111105, 2010. `doi: 10.1063/1.3488825`.

[29] C. G. Van de Walle, "Computational studies of conductivity in wide-band-gap semiconductors and oxides," *Journal of Physics: Condensed Matter*, 20(6):064230, 2008. `doi:10.1088/0953-8984/20/6/064230`.

[30] T. Ive, O. Brandt, H. Kostial, K. J. Friedland, L. Däweritz, and K. H. Ploog, "Controlled n-type doping of AlN:Si films grown on 6H-SiC(0001) by plasma-assisted molecular beam epitaxy," *Applied Physics Letters*, 86(2):024106, 2005. `doi:10.1063/1.1850183`.

[31] Y. Taniyasu, M. Kasu, and T. Makimoto, "Electrical conduction properties of n-type Si-doped AlN with high electron mobility (> 100 cm^2 v^{-1} s^{-1})," *Applied Physics Letters*, 85(20):4672–4674, 2004. `doi:10.1063/1.1824181`.

[32] A. Y. Polyakov, N. B. Smirnov, A. V. Govorkov, E. A. Kozhukhova, A. M. Dabiran, P. P. Chow, A. M. Wowchak, I.-H. Lee, J.-W. Ju, and S. J. Pearton, "Comparison of electrical properties and deep traps in p-Al$_x$Ga$_{1-x}$N grown by molecular beam epitaxy and metal organic chemical vapor deposition," *Journal of Applied Physics*, 106(7):073706–6, 2009. `doi:10.1063/1.3238508`.

[33] A. Castiglia, J.-F. Carlin, and N. Grandjean, "Role of stable and metastable Mg–H complexes in p-type GaN for cw blue laser diodes," *Applied Physics Letters*, 98(21):213505, 2011. `doi:10.1063/1.3593964`.

[34] S. Nakamura, T. Mukai, M. Senoh, and N. Iwasa, "Thermal annealing effects on p-type Mg-doped GaN films," *Japanese Journal of Applied Physics*, 31(Part 2, No. 2B):L139–L142, 1992. `doi:10.1143/JJAP.31.L139`.

[35] R. Q. Wu, L. Shen, M. Yang, Z. D. Sha, Y. Q. Cai, Y. P. Feng, Z. G. Huang, and Q. Y. Wu, "Possible efficient p-type doping of AlN using Be: An ab initio study," *Applied Physics Letters*, 91(15):152110, 2007. `doi:10.1063/1.2799241`.

[36] A. Sedhain, T. M. A. Tahtamouni, J. Li, J. Y. Lin, and H. X. Jiang, "Beryllium acceptor binding energy in AlN," *Applied Physics Letters*, 93(14):141104, 2008. `doi:10.1063/1.2996977`.

[37] Q.-H. Zheng, Y.-A. Yin, L.-H. Zhu, J. Huang, X.-Y. Li, and B.-L. Liu, "Tailoring the hole concentration in superlattices based on nitride alloys," *Applied Physics Letters*, 94(22):222104–3, 2009. `doi:10.1063/1.3148244`.

72

[38] A. Chakraborty, C. G. Moe, Y. Wu, T. Mates, S. Keller, J. S. Speck, S. P. DenBaars, and U. K. Mishra, "Electrical and structural characterization of Mg-doped p-type $Al_{0.69}Ga_{0.31}N$ films on SiC substrate," *Journal of Applied Physics*, 101(5):053717, 2007. `doi:10.1063/1.2710303`.

[39] M. L. Nakarmi, K. H. Kim, M. Khizar, Z. Y. Fan, J. Y. Lin, and H. X. Jiang, "Electrical and optical properties of Mg-doped $Al_{0.7}Ga_{0.3}N$ alloys," *Applied Physics Letters*, 86(9):092108, 2005. `doi:10.1063/1.1879098`.

[40] I. Vurgaftman and J. R. Meyer, "Band parameters for nitrogen-containing semiconductors," *Journal of Applied Physics*, 94(6):3675–3696, 2003. `doi:10.1063/1.1600519`.

[41] R. K. Sink. *Cleaved-Facet Group-III Nitride Lasers*. PhD thesis, University of California, Santa Barbara, 2000.

[42] Cree, "Silicon carbide substrates and epitaxy," `http://www.cree.com/products/pdf/MAT-CATALOG.pdf`, 2009. Last checked: 2011-01-03.

[43] U. Özgür, Y. I. Alivov, C. Liu, A. Teke, M. A. Reshchikov, S. Doğan, V. Avrutin, S.-J. Cho, and H. Morkoç, "A comprehensive review of ZnO materials and devices," *Journal of Applied Physics*, 98(4):041301, 2005. `doi:10.1063/1.1992666`.

[44] D. J. Rogers, F. H. Teherani, A. Ougazzaden, S. Gautier, L. Divay, A. Lusson, O. Durand, F. Wyczisk, G. Garry, T. Monteiro, M. R. Correira, M. Peres, A. Neves, D. McGrouther, J. N. Chapman, and M. Razeghi, "Use of ZnO thin films as sacrificial templates for metal organic vapor phase epitaxy and chemical lift-off of GaN," *Applied Physics Letters*, 91(7):071120, 2007. `doi:10.1063/1.2770655`.

[45] A. Kobayashi, K. Ueno, J. Ohta, and H. Fujioka, "Coherent growth of r-plane GaN films on ZnO substrates at room temperature," *Physica Status Solidi (a)*, 208(4):834–837, 2011. `doi:10.1002/pssa.201026397`.

[46] X. Gu, M. A. Reshchikov, A. Teke, D. Johnstone, H. Morkoc, B. Nemeth, and J. Nause, "GaN epitaxy on thermally treated c-plane bulk ZnO substrates with O and Zn faces," *Applied Physics Letters*, 84(13):2268–2270, 2004. `doi:10.1063/1.1690469`.

[47] R. Dwiliński, R. Doradziński, J. Garczyński, L. Sierzputowski, A. Puchalski, Y. Kanbara, K. Yagi, H. Minakuchi, and H. Hayashi, "Bulk ammonothermal GaN," *Journal of Crystal Growth*, 311(10):3015 – 3018, 2009. Proceedings of the 2nd International Symposium on Growth of III-Nitrides. `doi:10.1016/j.jcrysgro.2009.01.052`.

[48] R. Dwiliński, R. Doradziński, J. Garczyński, L. Sierzputowski, R. Kucharski, M. Zając, M. Rudziński, R. Kudrawiec, W. Strupiński, and J. Misiewicz, "Ammonothermal GaN substrates: Growth accomplishments and applications," *Physica Status Solidi (a)*, 208(7):1489–1493, 2011. `doi:10.1002/pssa.201001196`.

[49] R. Kucharski, M. Zając, R. Doradziński, M. Rudziński, R. Kudrawiec, and R. Dwiliński, "Non-polar and semi-polar ammonothermal GaN substrates," *Semiconductor Science and Technology*, 27(2):024007, 2012. `doi:10.1088/0268-1242/27/2/024007`.

[50] AMMONO, "Buy now - enquiry form," `http://ammono.com/enquiry-form`, 2013. Last checked: 2013-03-16.

[51] S. G. Mueller, R. T. Bondokov, K. E. Morgan, G. A. Slack, S. B. Schujman, J. Grandusky, J. A. Smart, and L. J. Schowalter, "The progress of AlN bulk growth and epitaxy for electronic applications," *Physica Status Solidi (a)*, 206(6):1153–1159, 2009. `doi:10.1002/pssa.200880758`.

[52] Z. Herro, D. Zhuang, R. Schlesser, and Z. Sitar, "Growth of AlN single crystalline boules," *Journal of Crystal Growth*, 312(18):2519–2521, 2010. `doi:10.1016/j.jcrysgro.2010.04.005`.

[53] Hexatech, "Aluminum nitride (AlN) substrate," `http://www.hexatechinc.com/documents/HexaTech-c-plane-transparent-wafer-spec-AlN-30.pdf`, 2013. Last checked: 2013-03-15.

[54] S.-H. Park, "Crystal orientation effects on electronic properties of wurtzite InGaN/GaN quantum wells," *Journal of Applied Physics*, 91(12):9904–9908, 2002. `doi:10.1063/1.1480465`.

[55] S.-H. Park and D. Ahn, "Depolarization effects in (11$\bar{2}$2)-oriented InGaN/GaN quantum well structures," *Applied Physics Letters*, 90(1):013505, 2007. `doi:10.1063/1.2420795`.

[56] Y. Zhao, Q. Yan, C.-Y. Huang, S.-C. Huang, P. S. Hsu, S. Tanaka, C.-C. Pan, Y. Kawaguchi, K. Fujito, C. G. V. de Walle, J. S. Speck, S. P. DenBaars, S. Nakamura, and D. Feezell, "Indium incorporation and emission properties of nonpolar and semipolar InGaN quantum wells," *Applied Physics Letters*, 100(20):201108, 2012. `doi:10.1063/1.4719100`.

[57] W. Kowalski. *Ultraviolet Germicidal Irradiation Handbook.* Springer-Verlag, 2009.

[58] S. E. Wilkie, P. M. Vissers, D. Das, W. J. Degrip, J. K. Bowmaker, and D. M. Hunt, "The molecular basis for UV vision in birds: spectral characteristics, cDNA sequence and retinal localization of the UV-sensitive visual pigment of the budgerigar (Melopsittacus undulatus)," *Biochemical Journal*, 330(1):541–547, 1998.

[59] ASTM International, "ASTM G173 - 03(2008) standard tables for reference solar spectral irradiances: Direct normal and hemispherical on 37° tilted surface," `http://rredc.nrel.gov/solar/spectra/am1.5/ASTMG173/ASTMG173.xls`, 2008. Downloaded at 2011-02-01.

[60] M. N. Baker. *The Quest for Pure Water*. The American Water Works Association, 1948.

[61] M. Würtele, T. Kolbe, M. Lipsz, A. Külberg, M. Weyers, M. Kneissl, and M. Jekel, "Application of GaN-based ultraviolet-c light emitting diodes - UV LEDs - for water disinfection," *Water Research*, 45(3):1481 – 1489, 2011. `doi:DOI:10.1016/j.watres.2010.11.015`.

[62] Heraeus Noblelight GmbH, "Design for economic efficiency with superior Heraeus amalgam lamps," `http://www.heraeus-noblelight.com/fileadmin/user_upload/PDF/disinfection/amalgam_comparison.pdf`, 2008. Last checked: 2011-01-07.

[63] J. Baur, F. Baumann, M. Peter, K. Engl, U. Zehnder, J. Off, V. Kuemmler, M. Kirsch, J. Strauss, R. Wirth, K. Streubel, and B. Hahn, "Status of high efficiency and high power ThinGaN®-LED development," *Physica Status Solidi (c)*, 6(S2):S905–S908, 2009. `doi:10.1002/pssc.200880936`.

[64] Blu-ray Disc™ Association, "Blu-ray Disc™ format," `http://www.blu-raydisc.com/Assets/Downloadablefile/general_bluraydiscformat-15263.pdf`, 2010. Last checked: 2011-01-07.

[65] J. A. Parrish, "Phototherapy and photochemotherapy of skin diseases," *Journal of Investigative Dermatology*, 77(1):167–171, 1981. `doi:10.1111/1523-1747.ep12479366`.

[66] Philips, "Light sources for phototherapy," `http://www.lighting.philips.com/pwc_li/main/application_areas/assets/phototheraphy/Phototherapy_treatment.pdf`, 2009. Last checked: 2013-03-18.

[67] A. Getty, E. Matioli, M. Iza, C. Weisbuch, and J. S. Speck, "Electroluminescent measurement of the internal quantum efficiency of light emitting diodes," *Applied Physics Letters*, 94(18):181102, 2009. `doi:10.1063/1.3129866`.

[68] H. Hirayama, S. Fujikawa, N. Noguchi, J. Norimatsu, T. Takano, K. Tsubaki, and N. Kamata, "222-282 nm AlGaN and InAlGaN-based deep-UV LEDs fabricated on high-quality AlN on sapphire," *Physica Status Solidi (a)*, 206(6):1176–1182, 2009. `doi:10.1002/pssa.200880961`.

[69] J. Grandusky, J. Smart, M. Mendrick, L. Schowalter, K. Chen, and E. Schubert, "Pseudomorphic growth of thick n-type $Al_xGa_{1-x}N$ layers on low-defect-density bulk AlN substrates for UV LED applications," *Journal of Crystal Growth*, 311(10):2864 – 2866, 2009. `doi:DOI:10.1016/j.jcrysgro.2009.01.101`.

[70] J. R. Grandusky, S. R. Gibb, M. C. Mendrick, and L. J. Schowalter, "Properties of mid-ultraviolet light emitting diodes fabricated from pseudomorphic layers on bulk aluminum nitride substrates," *Applied Physics Express*, 3(7):072103, 2010. `doi:10.1143/APEX.3.072103`.

[71] C. Pernot, M. Kim, S. Fukahori, T. Inazu, T. Fujita, Y. Nagasawa, A. Hirano, M. Ippommatsu, M. Iwaya, S. Kamiyama, I. Akasaki, and H. Amano, "Improved efficiency of 255–280 nm AlGaN-based light-emitting diodes," *Applied Physics Express*, 3(6):061004, 2010. `doi:10.1143/APEX.3.061004`.

[72] J. R. Grandusky, J. Chen, S. R. Gibb, M. C. Mendrick, C. G. Moe, L. Rodak, G. A. Garrett, M. Wraback, and L. J. Schowalter, "270 nm pseudomorphic ultraviolet light-emitting diodes with over 60 mW continuous wave output power," *Applied Physics Express*, 6(3):032101, 2013. `doi:10.1143/APEX.6.032101`.

[73] A. Fujioka, T. Misaki, T. Murayama, Y. Narukawa, and T. Mukai, "Improvement in output power of 280-nm deep ultraviolet light-emitting diode by using AlGaN multi quantum wells," *Applied Physics Express*, 3(4):041001, 2010. `doi:10.1143/APEX.3.041001`.

[74] A. Khan, K. Balakrishnan, and T. Katona, "Ultraviolet light-emitting diodes based on group three nitrides," *Nature Photonics*, 2(2):77–84, 2008. `doi:10.1038/nphoton.2007.293`.

[75] T. M. Smeeton, M. J. Kappers, J. S. Barnard, M. E. Vickers, and C. J. Humphreys, "Electron-beam-induced strain within ingan quantum wells: False indium "cluster" detection in the transmission electron microscope," *Applied Physics Letters*, 83(26):5419–5421, 2003. `doi:10.1063/1.1636534`.

[76] T. Schulz, T. Remmele, T. Markurt, M. Korytov, and M. Albrecht, "Analysis of statistical compositional alloy fluctuations in InGaN from aberration corrected transmission electron microscopy image series," *Journal of Applied Physics*, 112(3):033106, 2012. `doi:10.1063/1.4742015`.

[77] M. Kneissl, T. Kolbe, C. Chua, V. Kueller, N. Lobo, J. Stellmach, A. Knauer, H. Rodriguez, S. Einfeldt, Z. Yang, N. M. Johnson, and M. Weyers, "Advances in group III-nitride-based deep UV light-emitting diode technology," *Semiconductor Science and Technology*, 26(1):014036, 2011. `doi:10.1088/0268-1242/26/1/014036`.

[78] M. Shatalov, A. Lunev, X. Hu, O. Bilenko, I. Gaska, W. Sun, J. Yang, A. Dobrinsky, Y. Bilenko, R. Gaska, and M. Shur, "Performance and applications of deep UV LED," *International Journal of High Speed Electronics and Systems*, 21(01):1250011, 2012. `doi:10.1142/S0129156412500115`.

[79] J. R. Grandusky, S. R. Gibb, M. C. Mendrick, C. Moe, M. Wraback, and L. J. Schowalter, "High output power from 260 nm pseudomorphic ultraviolet light-emitting diodes with improved thermal performance," *Applied Physics Express*, 4(8):082101, 2011. `doi:10.1143/APEX.4.082101`.

[80] R. Collazo, J. Xie, B. E. Gaddy, Z. Bryan, R. Kirste, M. Hoffmann, R. Dalmau, B. Moody, Y. Kumagai, T. Nagashima, Y. Kubota, T. Kinoshita, A. Koukitu, D. L. Irving, and Z. Sitar, "On the origin of the 265 nm absorption band in AlN bulk crystals," *Applied Physics Letters*, 100(19):191914, 2012. `doi:10.1063/1.4717623`.

[81] T. Kinoshita, K. Hironaka, T. Obata, T. Nagashima, R. Dalmau, R. Schlesser, B. Moody, J. Xie, S. Inoue, Y. Kumagai, A. Koukitu, and Z. Sitar, "Deep-ultraviolet light-emitting diodes fabricated on AlN substrates prepared by hydride vapor phase epitaxy," *Applied Physics Express*, 5(12):122101, 2012. `doi:10.1143/APEX.5.122101`.

[82] Z. Lochner, T.-T. Kao, Y.-S. Liu, X.-H. Li, M. M. Satter, S.-C. Shen, P. D. Yoder, J.-H. Ryou, R. D. Dupuis, Y. Wei, H. Xie, A. Fischer, and F. A. Ponce, "Deep-ultraviolet lasing at 243 nm from photo-pumped AlGaN/AlN heterostructure on AlN substrate," *Applied Physics Letters*, 102(10):101110, 2013. `doi:10.1063/1.4795719`.

[83] T. Takano, Y. Narita, A. Horiuchi, and H. Kawanishi, "Room-temperature deep-ultraviolet lasing at 241.5 nm of AlGaN multiple-quantum-well laser," *Applied Physics Letters*, 84(18):3567–3569, 2004. `doi:10.1063/1.1737061`.

[84] J. Piprek, "Efficiency droop in nitride-based light-emitting diodes," *Physica Status Solidi (a)*, 207(10):2217–2225, 2010. `doi:10.1002/pssa.201026149`.

[85] A. David and M. J. Grundmann, "Droop in InGaN light-emitting diodes: A differential carrier lifetime analysis," *Applied Physics Letters*, 96(10):103504, 2010. `doi:10.1063/1.3330870`.

[86] D. S. Meyaard, G.-B. Lin, Q. Shan, J. Cho, E. F. Schubert, H. Shim, M.-H. Kim, and C. Sone, "Asymmetry of carrier transport leading to efficiency droop in GaInN based light-emitting diodes," *Applied Physics Letters*, 99(25):251115, 2011. `doi:10.1063/1.3671395`.

[87] K. Jarašiūnas, S. Nargelas, R. Aleksiejūnas, S. Miasojedovas, M. Vengris, S. Okur, H. Morkoç, U. Ozgür, C. Giesen, O. Tuna, and M. Heuken, "Spectral distribution of excitation-dependent recombination rate in an $In_{0.13}Ga_{0.87}N$ epilayer," *Journal of Applied Physics*, 113(10):103701, 2013. `doi:10.1063/1.4793637`.

[88] M. F. Schubert and J. K. Kim, "Efficiency droop in GaInN high-power light-emitting diodes," *International Journal of High Speed Electronics and Systems*, 20(02):247–265, 2011. `doi:10.1142/S0129156411006581`.

[89] S.-P. Chang, T.-C. Lu, L.-F. Zhuo, C.-Y. Jang, D.-W. Lin, H.-C. Yang, H.-C. Kuo, and S.-C. Wang, "Low droop nonpolar GaN/InGaN light emitting diode grown on m-plane GaN substrate," *Journal of The Electrochemical Society*, 157(5):H501–H503, 2010. `doi:10.1149/1.3327909`.

[90] S.-C. Ling, T.-C. Lu, S.-P. Chang, J.-R. Chen, H.-C. Kuo, and S.-C. Wang, "Low efficiency droop in blue-green m-plane InGaN/GaN light emitting diodes," *Applied Physics Letters*, 96(23):231101, 2010. `doi:10.1063/1.3449557`.

[91] A. David and N. F. Gardner, "Droop in III-nitrides: Comparison of bulk and injection contributions," *Applied Physics Letters*, 97(19):193508, 2010. `doi:10.1063/1.3515851`.

[92] M. J. Cich, R. I. Aldaz, A. Chakraborty, A. David, M. J. Grundmann, A. Tyagi, M. Zhang, F. M. Steranka, and M. R. Krames, "Bulk GaN based violet light-emitting diodes with high efficiency at very high current density," *Applied Physics Letters*, 101(22):223509, 2012. `doi:10.1063/1.4769228`.

[93] M. Cooke, "Short- and long-reach of new VCSEL applications," *Semiconductor Today*, 6(6):116–121, 2011.

[94] T. Onishi, O. Imafuji, K. Nagamatsu, M. Kawaguchi, K. Yamanaka, and S. Takigawa, "Continuous wave operation of gan vertical cavity surface emitting lasers at room temperature," *Quantum Electronics, IEEE Journal of*, 48(9):1107–1112, 2012. `doi:10.1109/JQE.2012.2203586`.

[95] T.-C. Lu, T.-T. Wu, S.-W. Chen, P.-M. Tu, Z.-Y. Li, C.-K. Chen, C.-H. Chen, H.-C. Kuo, S.-C. Wang, H.-W. Zan, and C.-Y. Chang, "Characteristics of current-injected GaN-based vertical-cavity surface-emitting lasers," *Selected Topics in Quantum Electronics, IEEE Journal of*, 17(6):1594–1602, 2011. `doi:10.1109/JSTQE.2011.2116771`.

[96] G. Cosendey, A. Castiglia, G. Rossbach, J.-F. Carlin, and N. Grandjean, "Blue monolithic AlInN-based vertical cavity surface emitting laser diode on free-standing GaN substrate," *Applied Physics Letters*, 101(15):151113, 2012. `doi:10.1063/1.4757873`.

[97] Y. Higuchi, K. Omae, H. Matsumura, and T. Mukai, "Room-temperature CW lasing of a GaN-based vertical-cavity surface-emitting laser by current injection," *Applied Physics Express*, 1(12):121102, 2008. `doi:10.1143/APEX.1.121102`.

[98] T.-C. Lu, C.-C. Kao, H.-C. Kuo, G.-S. Huang, and S.-C. Wang, "CW lasing of current injection blue GaN-based vertical cavity surface emitting laser," *Applied Physics Letters*, 92(14):141102, 2008. `doi:10.1063/1.2908034`.

[99] E. Hashemi, J. Gustavsson, J. Bengtsson, M. Stattin, G. Cosendey, N. Grandjean, and Å. Haglund, "Engineering the lateral optical guiding in gallium nitride-based vertical-cavity surface-emitting laser cavities to reach the lowest threshold gain," Japanese Journal of Applied Physics, 2013. To be published.

[100] I. Hamberg and C. G. Granqvist, "Evaporated Sn-doped In_2O_3 films: Basic optical properties and applications to energy-efficient windows," *Journal of Applied Physics*, 60(11):R123–R160, 1986. `doi:10.1063/1.337534`.

[101] T. Minami, "Transparent conducting oxide semiconductors for transparent electrodes," *Semiconductor Science and Technology*, 20(4):S35, 2005. `doi:10.1088/0268-1242/20/4/004`.

[102] X. A. Cao, S. J. Pearton, A. P. Zhang, G. T. Dang, F. Ren, R. J. Shul, L. Zhang, R. Hickman, and J. M. V. Hove, "Electrical effects of plasma damage in p-GaN," *Applied Physics Letters*, 75(17):2569–2571, 1999. `doi:10.1063/1.125080`.

[103] Evatec Process Systems, "HB LEDs & OLEDs," Online: `http://www.evatecnet.com/uploads/media/EVA_LED_TFP_8p_web_july2012.pdf`, 2012. Last checked: 2013-02-28.

[104] S. S. Thöny, H. Friedli, M. Padrun, A. Castiglia, G. Cosendey, and N. Grandjean, "Damage-free ITO deposition on LED devices," In *IWN2012 - International Workshop on Nitride Semiconductors - Abstract Book*, pages ThP–OD–20, 2012.

[105] J. Song, J.-S. Ha, and T.-Y. Seong, "Ohmic-contact technology for GaN-based light-emitting diodes: Role of p-type contact," *Electron Devices, IEEE Transactions on*, 57(1):42 –59, 2010. `doi:10.1109/TED.2009.2034506`.

[106] H. Kawazoe, M. Yasukawa, H. Hyodo, M. Kurita, H. Yanagi, and H. Hosono, "P-type electrical conduction in transparent thin films of $CuAlO_2$," *Nature*, 389(6654):939–942, 1997. `doi:10.1038/40087`.

[107] H. Sato, T. Minami, S. Takata, and T. Yamada, "Transparent conducting p-type NiO thin films prepared by magnetron sputtering," *Thin Solid Films*, 236(1-2):27–31, 1993. `doi:10.1016/0040-6090(93)90636-4`.

[108] M. A. Marquardt, N. A. Ashmore, and D. P. Cann, "Crystal chemistry and electrical properties of the delafossite structure," *Thin Solid Films*, 496(1):146–156, 2006. `doi:10.1016/j.tsf.2005.08.316`.

[109] J.-H. Lim, D.-K. Hwang, H.-S. Kim, J.-H. Yang, R. Navamathavan, and S.-J. Park, "Effect of interlayers on the indium oxide-doped ZnO ohmic contact to p-type GaN," *Journal of The Electrochemical Society*, 152(6):G491–G493, 2005. `doi:10.1149/1.1914758`.

[110] T. Gessmann, J. W. Graff, Y.-L. Li, E. L. Waldron, and E. F. Schubert, "Ohmic contact technology in III nitrides using polarization effects of cap layers," *Journal of Applied Physics*, 92(7):3740–3744, 2002. `doi:10.1063/1.1504169`.

[111] F. Bonaccorso, Z. Sun, T. Hasan, and A. C. Ferrari, "Graphene photonics and optoelectronics," *Nature Photonics*, 4(9):611–622, 2010. `doi:10.1038/nphoton.2010.186`.

[112] R. R. Nair, P. Blake, A. N. Grigorenko, K. S. Novoselov, T. J. Booth, T. Stauber, N. M. R. Peres, and A. K. Geim, "Fine structure constant defines visual transparency of graphene," *Science*, 320(5881):1308, 2008. `doi:10.1126/science.1156965`.

[113] A. K. Geim and K. S. Novoselov, "The rise of graphene," *Nature Materials*, 6(3):183–191, 2007. `doi:10.1038/nmat1849`.

[114] K. S. Novoselov, V. I. Fal'ko, L. Colombo, P. R. Gellert, M. G. Schwab, and K. Kim, "A roadmap for graphene," *Nature*, 490(7419):192–200, 2012. `doi:10.1038/nature11458`.

[115] G. Giovannetti, P. A. Khomyakov, G. Brocks, V. M. Karpan, J. van den Brink, and P. J. Kelly, "Doping graphene with metal contacts," *Physical Review Letters*, 101:026803, 2008. `doi:10.1103/PhysRevLett.101.026803`.

[116] K. S. Novoselov, A. K. Geim, S. V. Morozov, D. Jiang, Y. Zhang, S. V. Dubonos, I. V. Grigorieva, and A. A. Firsov, "Electric field effect in atomically thin carbon films," *Science*, 306(5696):666–669, 2004. `doi:10.1126/science.1102896`.

[117] X. Li, W. Cai, J. An, S. Kim, J. Nah, D. Yang, R. Piner, A. Velamakanni, I. Jung, E. Tutuc, S. K. Banerjee, L. Colombo, and R. S. Ruoff, "Large-area synthesis of high-quality and uniform graphene films on copper foils," *Science*, 324(5932):1312–1314, 2009. `doi:10.1126/science.1171245`.

[118] J. Sun, N. Lindvall, M. Cole, K. Angel, T. Wang, K. Teo, D. Chua, J. Liu, and A. Yurgens, "Low partial pressure chemical vapor deposition of graphene on copper," *Nanotechnology, IEEE Transactions on*, 11(2):255 –260, 2012. `doi: 10.1109/TNANO.2011.2160729`.

[119] I. Forbeaux, J.-M. Themlin, and J.-M. Debever, "Heteroepitaxial graphite on 6H-SiC(0001): Interface formation through conduction-band electronic structure," *Physical Review B*, 58:16396–16406, 1998. `doi:10.1103/PhysRevB.58.16396`.

[120] C. Virojanadara, M. Syväjarvi, R. Yakimova, L. I. Johansson, A. A. Zakharov, and T. Balasubramanian, "Homogeneous large-area graphene layer growth on 6H-SiC(0001)," *Physical Review B*, 78:245403, 2008. `doi:10.1103/PhysRevB. 78.245403`.

[121] C. J. L. de la Rosa, J. Sun, N. Lindvall, M. T. Cole, Y. Nam, M. Loffler, E. Olsson, K. B. K. Teo, and A. Yurgens, "Frame assisted H_2O electrolysis induced H_2 bubbling transfer of large area graphene grown by chemical vapor deposition on Cu," *Applied Physics Letters*, 102(2):022101, 2013. `doi:10.1063/ 1.4775583`.

[122] Y. Zhang, L. Wang, X. Li, X. Yi, N. Zhang, J. Li, H. Zhu, and G. Wang, "Annealed InGaN green light-emitting diodes with graphene transparent conductive electrodes," *Journal of Applied Physics*, 111(11):114501, 2012. `doi: 10.1063/1.4723813`.

[123] S. Chandramohan, J. H. Kang, Y. S. Katharria, N. Han, Y. S. Beak, K. B. Ko, J. B. Park, H. K. Kim, E.-K. Suh, and C.-H. Hong, "Work-function-tuned multilayer graphene as current spreading electrode in blue light-emitting diodes," *Applied Physics Letters*, 100(2):023502, 2012. `doi:10.1063/1.3675631`.

[124] B.-J. Kim, C. Lee, Y. Jung, K. H. Baik, M. A. Mastro, J. K. Hite, J. Charles R. Eddy, and J. Kim, "Large-area transparent conductive few-layer graphene electrode in GaN-based ultra-violet light-emitting diodes," *Applied Physics Letters*, 99(14):143101, 2011. `doi:10.1063/1.3644496`.

[125] T. H. Seo, T. S. Oh, S. J. Chae, A. H. Park, K. J. Lee, Y. H. Lee, and E.-K. Suh, "Enhanced light output power of GaN light-emitting diodes with graphene film as a transparent conducting electrode," *Japanese Journal of Applied Physics*, 50:125103, 2011. `doi:10.1143/JJAP.50.125103`.

[126] J. M. Lee, H. Y. Jeong, K. J. Choi, and W. I. Park, "Metal/graphene sheets as p-type transparent conducting electrodes in GaN light emitting diodes," *Applied Physics Letters*, 99(4):041115, 2011. `doi:10.1063/1.3595941`.

[127] A. S. Mayorov, R. V. Gorbachev, S. V. Morozov, L. Britnell, R. Jalil, L. A. Ponomarenko, P. Blake, K. S. Novoselov, K. Watanabe, T. Taniguchi, and A. K. Geim, "Micrometer-scale ballistic transport in encapsulated graphene at room temperature," *Nano Letters*, 11(6):2396–2399, 2011. `doi:10.1021/nl200758b`.

[128] J. Yamaguchi, K. Hayashi, S. Sato, and N. Yokoyama, "Passivating chemical vapor deposited graphene with metal oxides for transfer and transistor fabrication processes," *Applied Physics Letters*, 102(14):143505, 2013. `doi: 10.1063/1.4801927`.

[129] Y.-K. Song, H. Zhou, M. Diagne, I. Ozden, A. Vertikov, A. V. Nurmikko, C. Carter-Coman, R. S. Kern, F. A. Kish, and M. R. Krames, "A vertical cavity light emitting InGaN quantum well heterostructure," *Applied Physics Letters*, 74(23):3441–3443, 1999. `doi:10.1063/1.124121`.

[130] G. Cosendey, J.-F. Carlin, N. A. K. Kaufmann, R. Butte, and N. Grandjean, "Strain compensation in AlInN/GaN multilayers on GaN substrates: Application to the realization of defect-free Bragg reflectors," *Applied Physics Letters*, 98(18):181111, 2011. `doi:10.1063/1.3586767`.

[131] R. Butté, E. Feltin, J. Dorsaz, G. Christmann, J.-F. Carlin, N. Grandjean, and M. Ilegems, "Recent progress in the growth of highly reflective nitride-based distributed Bragg reflectors and their use in microcavities," *Japanese Journal of Applied Physics*, 44(10):7207–7216, 2005. `doi:10.1143/JJAP.44.7207`.

[132] Ž. Gačević, S. Fernández-Garrido, D. Hosseini, S. Estrade, F. Peiró, and E. Calleja, "InAlN/GaN Bragg reflectors grown by plasma-assisted molecular beam epitaxy," *Journal of Applied Physics*, 108(11):113117, 2010. `doi: 10.1063/1.3517138`.

[133] T. Ive, O. Brandt, X. Kong, A. Trampert, and K. H. Ploog, "(Al,In)N layers and (Al,In)N/GaN heterostructures grown by plasma-assisted molecular beam epitaxy on 6H-SiC (0001)," *Physical Review B*, 78:035311, 2008. `doi:10.1103/PhysRevB.78.035311`.

[134] T. Mukai and S. Nakamura, "Ultraviolet InGaN and GaN single-quantum-well-structure light-emitting diodes grown on epitaxially laterally overgrown GaN substrates," *Japanese Journal of Applied Physics*, 38(Part 1, No. 10):5735–5739, 1999. `doi:10.1143/JJAP.38.5735`.

[135] S. Tomiya, T. Hino, S. Goto, M. Takeya, and M. Ikeda, "Dislocation related issues in the degradation of GaN-based laser diodes," *Selected Topics in Quantum Electronics, IEEE Journal of*, 10(6):1277–1286, 2004. `doi:10.1109/JSTQE.2004.837735`.

[136] T. Ive, O. Brandt, H. Kostial, T. Hesjedal, M. Ramsteiner, and K. H. Ploog, "Crack-free and conductive Si-doped AlN/GaN distributed Bragg reflectors grown on 6H-SiC(0001)," *Applied Physics Letters*, 85(11):1970–1972, 2004. `doi:10.1063/1.1791738`.

[137] M. Arita, M. Nishioka, and Y. Arakawa, "InGaN vertical microcavity LEDs with a Si-doped AlGaN/GaN distributed Bragg reflector," *Physica Status Solidi (a)*, 194(2):403–406, 2002. `doi:10.1002/1521-396X(200212)194:2<403::AID-PSSA403>3.0.CO;2-2`.

[138] S. Figge, H. Dartsch, T. Aschenbrenner, C. Kruse, and D. Hommel, "Distributed Bragg reflectors in comparison to RUGATE and nested super lattices - growth, reflectivity, and conductivity," *Physica Status Solidi (c)*, 5(6):1839–1842, 2008. `doi:10.1002/pssc.200778692`.

[139] B. M. Hawkins, R. A. Hawthorne III, J. K. Guenter, J. A. Tatum, and J. R. Biard, "Reliability of various size oxide aperture VCSELs," In *Electronic Components and Technology Conference, 2002. Proceedings. 52nd*, pages 540–550, 2002. `doi:10.1109/ECTC.2002.1008148`.

[140] A. Castiglia, D. Simeonov, H. J. Buehlmann, J.-F. Carlin, E. Feltin, J. Dorsaz, R. Butte, and N. Grandjean, "Efficient current injection scheme for nitride vertical cavity surface emitting lasers," *Applied Physics Letters*, 90(3):033514, 2007. `doi:10.1063/1.2431484`.

[141] J. Dorsaz, H.-J. Buhlmann, J.-F. Carlin, N. Grandjean, and M. Ilegems, "Selective oxidation of AlInN layers for current confinement in III–nitride devices," *Applied Physics Letters*, 87(7):072102, 2005. `doi:10.1063/1.2012533`.

[142] W.-S. Tan, K. Takahashi, V. Bousquet, A. Ariyoshi, Y. Tsuda, M. Ohta, and M. Kauer, "Blue-violet inner stripe laser diodes using lattice matched AlInN as current confinement layer for high power operation," *Applied Physics Express*, 2(11):112101, 2009. `doi:10.1143/APEX.2.112101`.

[143] B.-S. Cheng, Y.-L. Wu, T.-C. Lu, C.-H. Chiu, C.-H. Chen, P.-M. Tu, H.-C. Kuo, S.-C. Wang, and C.-Y. Chang, "High Q microcavity light emitting diodes with buried AlN current apertures," *Applied Physics Letters*, 99(4):041101, 2011. `doi:10.1063/1.3617418`.

[144] J. Faist, F. Capasso, D. L. Sivco, C. Sirtori, A. L. Hutchinson, and A. Y. Cho, "Quantum cascade laser," *Science*, 264(5158):553–556, 1994. `doi:10.1126/science.264.5158.553`.

[145] Y. Yao, A. J. Hoffman, and C. F. Gmachl, "Mid-infrared quantum cascade lasers," *Nature Photonics*, 6(7):432–439, 2012.

[146] Y. Bai, S. Slivken, S. Kuboya, S. R. Darvish, and M. Razeghi, "Quantum cascade lasers that emit more light than heat," *Nature Photonics*, 4(2):99–102, 2010.

[147] M. Peters, V. Rossin, M. Everett, and E. Zucker, "High-power, high-efficiency laser diodes at JDSU," In *High-Power Diode Laser Technology and Applications V*, volume 6456 of *Proc. SPIE*, pages 64560G–1–11, 2007. `doi:10.1117/12.701072.`

[148] M. Razeghi, "High-performance InP-based mid-IR quantum cascade lasers," *Selected Topics in Quantum Electronics, IEEE Journal of*, 15(3):941–951, 2009. `doi:10.1109/JSTQE.2008.2006764.`

[149] A. A. Kosterev, F. K. Tittel, C. Gmachl, F. Capasso, D. L. Sivco, J. N. Baillargeon, A. L. Hutchinson, and A. Y. Cho, "Trace-gas detection in ambient air with a thermoelectrically cooled, pulsed quantum-cascade distributed feedback laser," *Applied Optics*, 39(36):6866–6872, 2000. `doi:10.1364/AO.39.006866.`

[150] C. Nordling and J. Österman. *Physics Handbook for Science and Engineering.* Studentlitteratur, sixth edition, 1999.

[151] R. M. Williams, J. F. Kelly, J. S. Hartman, S. W. Sharpe, M. S. Taubman, J. L. Hall, F. Capasso, C. Gmachl, D. L. Sivco, J. N. Baillargeon, and A. Y. Cho, "Kilohertz linewidth from frequency-stabilized mid-infrared quantum cascade lasers," *Optics Letters*, 24(24):1844–1846, 1999. `doi:10.1364/OL.24.001844.`

[152] D. Cohen and L. Coldren, "Passive temperature compensation of uncooled GaInAsP-InP diode lasers using thermal stress," *Selected Topics in Quantum Electronics, IEEE Journal of*, 3(2):649–658, 1997. `doi:10.1109/2944.605717.`

[153] B. S. Williams, S. Kumar, H. Callebaut, Q. Hu, and J. L. Reno, "Terahertz quantum-cascade laser at $\lambda \approx 100$ μm using metal waveguide for mode confinement," *Applied Physics Letters*, 83(11):2124–2126, 2003. `doi:10.1063/1.1611642.`

[154] M. Razeghi, "Toward realizing high power semiconductor terahertz laser sources at room temperature," In *Terahertz Physics, Devices, and Systems V: Advance Applications in Industry and Defense*, volume 8023 of *Proc. SPIE*, pages 802302–1–7, 2011. `doi:10.1117/12.887986.`

[155] W. Terashima and H. Hirayama, "Terahertz intersubband electroluminescence from GaN/AlGaN quantum cascade laser structure on AlGaN template," In *Infrared, Millimeter and Terahertz Waves (IRMMW-THz), 2011 36th International Conference on*, pages 1–2, 2011. `doi:10.1109/irmmw-THz.2011.6105201.`

[156] N. Bandyopadhyay, Y. Bai, S. Tsao, S. Nida, S. Slivken, and M. Razeghi, "Room temperature continuous wave operation of $\lambda \sim$ 3–3.2 μm quantum cascade lasers," *Applied Physics Letters*, 101(24):241110, 2012. `doi:10.1063/1.4769038`.

[157] C. V.-B. Tribuzy, S. Ohser, S. Winnerl, J. Grenzer, H. Schneider, M. Helm, J. Neuhaus, T. Dekorsy, K. Biermann, and H. Kunzel, "Femtosecond pump-probe spectroscopy of intersubband relaxation dynamics in narrow InGaAs/AlAsSb quantum well structures," *Applied Physics Letters*, 89(17):171104, 2006. `doi:10.1063/1.2360242`.

[158] A. Rubio, J. L. Corkill, M. L. Cohen, E. L. Shirley, and S. G. Louie, "Quasiparticle band structure of AlN and GaN," *Physical Review B*, 48(16):11810–11816, 1993. `doi:10.1103/PhysRevB.48.11810`.

[159] D. Segev, A. Janotti, and C. G. Van de Walle, "Self-consistent band-gap corrections in density functional theory using modified pseudopotentials," *Physical Review B*, 75(3):035201, 2007. `doi:10.1103/PhysRevB.75.035201`.

[160] S. Wu, P. Geiser, J. Jun, J. Karpinski, D. Wang, and R. Sobolewski, "Time-resolved intervalley transitions in GaN single crystals," *Journal of Applied Physics*, 101(4):043701, 2007. `doi:10.1063/1.2496399`.

[161] C.-K. Sun, Y.-L. Huang, S. Keller, U. K. Mishra, and S. P. DenBaars, "Ultrafast electron dynamics study of GaN," *Physical Review B*, 59:13535–13538, 1999. `doi:10.1103/PhysRevB.59.13535`.

[162] M. Semenenko, O. Yilmazoglu, H. L. Hartnagel, and D. Pavlidis, "Determination of satellite valley position in GaN emitter from photoexcited field emission investigations," *Journal of Applied Physics*, 109(2):023703, 2011. `doi:10.1063/1.3533770`.

[163] J. Faist, F. Capasso, C. Sirtori, D. L. Sivco, and A. Y. Cho. *Intersubband Transitions in Quantum Wells: Physics and Device Applications II*, volume 66 of *Semiconductors and Semimetals*, chapter 1 *Quantum Cascade Lasers*, pages 1–83. Academic Press, 2000.

[164] C. Sirtori, P. Kruck, S. Barbieri, P. Collot, J. Nagle, M. Beck, J. Faist, and U. Oesterle, "GaAs/Al$_x$Ga$_{1-x}$As quantum cascade lasers," *Applied Physics Letters*, 73(24):3486–3488, 1998. `doi:10.1063/1.122812`.

[165] J. Devenson, D. Barate, O. Cathabard, R. Teissier, and A. N. Baranov, "Very short wavelength ($\lambda = 3.1 - 3.3$ μm) quantum cascade lasers," *Applied Physics Letters*, 89(19):191115, 2006. `doi:10.1063/1.2387473`.

[166] C. Sirtori, P. Kruck, S. Barbieri, H. Page, J. Nagle, M. Beck, J. Faist, and U. Oesterle, "Low-loss Al-free waveguides for unipolar semiconductor lasers," *Applied Physics Letters*, 75(25):3911–3913, 1999. `doi:10.1063/1.125491`.

[167] P. Holmström, "Electroabsorption modulator using intersubband transitions in GaN-AlGaN-AlN step quantum wells," *Quantum Electronics, IEEE Journal of*, 42(8):810 –819, 2006. `doi:10.1109/JQE.2006.877297`.

[168] E. D. Palik, editor. *Handbook of Optical Constants of Solids III*. Academic Press, 1998.

[169] P. T. B. Shaffer, "Refractive index, dispersion, and birefringence of silicon carbide polytypes," *Applied Optics*, 10(5):1034–1036, 1971. `doi:10.1364/AO.10.001034`.

[170] M. Scherer, V. Schwegler, M. Seyboth, F. Eberhard, C. Kirchner, M. Kamp, G. Ulu, M. Ünlü, R. Gruhler, and O. Hollricher, "Characterization of etched facets for GaN-based lasers," *Journal of Crystal Growth*, 230(3-4):554 – 557, 2001. Proceedings of the Fourth European Workshop on Gallium Nitride. `doi:10.1016/S0022-0248(01)01296-9`.

[171] F. Eberhard, M. Schauler, E. Deichsel, C. Kirchner, and P. Unger, "Comparison of the etching behavior of GaAs and GaN in a chemically-assisted ion-beam etching system," *Microelectronic Engineering*, 46(1-4):323 – 326, 1999. International Conference on Micro- and Nanofabrication. `doi:10.1016/S0167-9317(99)00095-7`.

[172] I. Chyr and A. J. Steckl, "GaN focused ion beam micromachining with gas-assisted etching," *The 45th international conference on electron, ion, and photon beam technology and nanofabrication*, 19(6):2547–2550, 2001. `doi:10.1116/1.1417550`.

[173] D. A. Stocker, E. F. Schubert, and J. M. Redwing, "Crystallographic wet chemical etching of GaN," *Applied Physics Letters*, 73:2654–2656, 1998. `doi:doi:10.1063/1.122543`.

[174] W. Yim, E. Stofko, P. Zanzucchi, J. Pankove, M. Ettenberg, and S. Gilbert, "Epitaxially grown AlN and its optical band gap," *Journal of Applied Physics*, 44(1):292–296, 1973. `doi:10.1063/1.1661876`.

[175] D. S. Kamber, Y. Wu, B. A. Haskell, S. Newman, S. P. DenBaars, J. S. Speck, and S. Nakamura, "Direct heteroepitaxial growth of thick AlN layers on sapphire substrates by hydride vapor phase epitaxy," *Journal of Crystal Growth*, 297(2):321 – 325, 2006. `doi:10.1016/j.jcrysgro.2006.10.097`.

[176] W. Zhang and B. K. Meyer, "Growth of GaN quasi-substrates by hydride vapor phase epitaxy," *Physica Status Solidi (c)*, 0(6):1571–1582, 2003. `doi:10.1002/pssc.200303136`.

[177] A. Usui, H. Sunakawa, A. Sakai, and A. A. Yamaguchi, "Thick GaN epitaxial growth with low dislocation density by hydride vapor phase epitaxy," *Japanese Journal of Applied Physics*, 36(Part 2, No. 7B):L899–L902, 1997. `doi:10.1143/JJAP.36.L899`.

[178] H. Aida, K. K. Martin, K. Ikejiri, T. Aoyagi, M. Takeuchi, S. Kim, H. Takeda, N. Aota, and N. Grandjean, "Growth of thick GaN layers by hydride vapor phase epitaxy on sapphire substrate with internally focused laser processing," *Applied Physics Express*, 6(3):035502, 2013. `doi:10.1143/APEX.6.035502`.

[179] K. Tsujisawa, S. Kishino, D.-B. Li, H. Miyake, K. Hiramatsu, T. Shibata, and M. Tanaka, "Suppression of crack generation using high-compressive-strain AlN/sapphire template for hydride vapor phase epitaxy of thick AlN film," *Japanese Journal of Applied Physics*, 46(23):L552–L555, 2007. `doi:10.1143/JJAP.46.L552`.

[180] T. Paskova, D. Hanser, and K. Evans, "GaN substrates for III-nitride devices," *Proceedings of the IEEE*, 98(7):1324–1338, 2010. `doi:10.1109/JPROC.2009.2030699`.

[181] V. Noveski, R. Schlesser, S. Mahajan, S. Beaudoin, and Z. Sitar, "Mass transfer in AlN crystal growth at high temperatures," *Journal of Crystal Growth*, 264:369 – 378, 2004. `doi:10.1016/j.jcrysgro.2004.01.028`.

[182] Aixtron, "Close coupled showerhead® CRIUS® II-XL," `http://www.aixtron.com/fileadmin/documents/matrix/production_systems/CCS_CRIUS_II-XL.pdf`, 2011. Last checked: 2013-03-10.

[183] A. Kakanakova-Georgieva, U. Forsberg, I. Ivanov, and E. Janzén, "Uniform hot-wall MOCVD epitaxial growth of 2 inch AlGaN/GaN HEMT structures," *Journal of Crystal Growth*, 300(1):100–103, 2007. `doi:10.1016/j.jcrysgro.2006.10.242`.

[184] A. Lundskog. *Controlled grwoth of hexagonal GaN pyramids and InGaN QDs*. PhD thesis, Linköping University, 2012.

[185] M. A. Hermann and H. Sitter. *Molecular Beam Epitaxy*. Springer-Verlag, 1989.

[186] A. J. Ptak, T. H. Myers, L. T. Romano, C. G. V. de Walle, and J. E. Northrup, "Magnesium incorporation in GaN grown by molecular-beam epitaxy," *Applied Physics Letters*, 78(3):285–287, 2001. `doi:10.1063/1.1339255`.

[187] O. Ambacher, H. Angerer, R. Dimitrov, W. Rieger, M. Stutzmann, G. Dollinger, and A. Bergmaier, "Hydrogen in gallium nitride grown by MOCVD," *Physica Status Solidi (a)*, 159(1):105–119, 1997. `doi:10.1002/1521-396X(199701)159:1<105::AID-PSSA105>3.0.CO;2-H`.

[188] O. Ambacher, F. Freudenberg, R. Dimitrov, H. Angerer, and M. Stutzmann, "Nitrogen effusion and self-diffusion in $Ga^{14}N/Ga^{15}N$ isotope heterostructures," *Japanese Journal of Applied Physics*, 37(Part 1, No. 5A):2416–2421, 1998. `doi:10.1143/JJAP.37.2416`.

[189] S. Porowski, I. Grzegory, D. Kolesnikov, W. Lojkowski, V. Jager, W. Jager, V. Bogdanov, T. Suski, and S. Krukowski, "Annealing of GaN under high pressure of nitrogen," *Journal of Physics: Condensed Matter*, 14(44):11097, 2002. `doi:10.1088/0953-8984/14/44/433`.

[190] R. Williams. *Modern GaAs processing methods*. Artech House, second edition, 1990.

[191] M. DeVre, R. Westerman, G. Muir, and L. Bellon, "Recent advances in GaN dry etching process capabilities," `http://www.plasma-therm.com/pdfs/papers/7.%20Advances%20in%20GaN%20Dry%20Etching%20Process%20Capabilities.pdf`, Unaxis Wafer Processing, 2004. Last checked: 2011-01-01.

[192] J. A. Amick, G. L. Schnable, and J. L. Vossen, "Deposition techniques for dielectric films on semiconductor devices," *Journal of Vacuum Science and Technology*, 14(5):1053–1063, 1977. `doi:10.1116/1.569412`.

[193] A. Motayed, R. Bathe, M. C. Wood, O. S. Diouf, R. D. Vispute, and S. N. Mohammad, "Electrical, thermal, and microstructural characteristics of Ti/Al/Ti/Au multilayer ohmic contacts to n-type GaN," *Journal of Applied Physics*, 93(2):1087–1094, 2003. `doi:10.1063/1.1528294`.

[194] S. Fernandez, R. Pena, M. T. Rodrigo, J. Plaza, M. Verdu, F. J. Sanchez, and M. T. Montojo, "Low resistance Ti/Al/Ti–W/Au ohmic contact to n-GaN for high temperature applications," *Applied Physics Letters*, 90(8):083504–3, 2007. `doi:10.1063/1.2539670`.

[195] J. K. Kim, H. W. Jang, and J.-L. Lee, "Mechanism for ohmic contact formation of Ti on n-type GaN investigated using synchrotron radiation photoemission spectroscopy," *Journal of Applied Physics*, 91(11):9214–9217, 2002. `doi:10.1063/1.1476085`.

[196] Z. Fan, S. N. Mohammad, W. Kim, O. Aktas, A. E. Botchkarev, and H. Morkoç, "Very low resistance multilayer ohmic contact to n-GaN," *Applied Physics Letters*, 68(12):1672–1674, 1996. `doi:10.1063/1.115901`.

[197] K. O. Schweitz, P. K. Wang, S. E. Mohney, and D. Gotthold, "V/Al/Pt/Au ohmic contact to n-AlGaN/GaN heterostructures," *Applied Physics Letters*, 80(11):1954–1956, 2002. `doi:10.1063/1.1459768`.

[198] M. A. Miller, S.-K. Lin, and S. E. Mohney, "V/Al/V/Ag contacts to n-GaN and n-AlGaN," *Journal of Applied Physics*, 104(6):064508–4, 2008. `doi:10.1063/1.2980038`.

[199] M. W. Cole and P. C. Joshi. *III-Nitride Semiconductors Applications and Devices*, volume 16 of *Optoelectronic Properties of Semiconductors and Superlattices*, chapter 1 Ohmic Contacts to GaN, pages 1–105. Taylor and Francis Books, 2003.

[200] S. Arulkumaran, T. Egawa, H. Ishikawa, T. Jimbo, and M. Umeno, "Investigations of SiO_2/n-GaN and Si_3N_4/n-GaN insulator–semiconductor interfaces with low interface state density," *Applied Physics Letters*, 73(6):809–811, 1998. `doi:10.1063/1.122009`.

[201] H. W. Jang, S. Y. Kim, and J.-L. Lee, "Mechanism for Ohmic contact formation of oxidized Ni/Au on p-type GaN," *Journal of Applied Physics*, 94(3):1748–1752, 2003. `doi:10.1063/1.1586983`.

[202] J. Liday, I. Hotový, H. Sitter, P. Vogrinčič, A. Vincze, I. Vávra, A. Šatka, G. Ecke, A. Bonanni, J. Breza, C. Simbrunner, and B. Plochberger, "Investigation of NiO_x-based contacts on p-GaN," *Journal of Materials Science: Materials in Electronics*, 19:855–862, 2008. `doi:10.1007/s10854-007-9520-1`.

[203] S. P. Lee, H. W. Jang, D. Y. Noh, and H. C. Kang, "Connected Au network in annealed Ni/Au thin films on p-GaN," *Applied Physics Letters*, 91(20):201905, 2007. `doi:10.1063/1.2809635`.

[204] V. M. Kaganer, O. Brandt, A. Trampert, and K. H. Ploog, "X-ray diffraction peak profiles from threading dislocations in GaN epitaxial films," *Physical Review B*, 72:045423, 2005. `doi:10.1103/PhysRevB.72.045423`.

[205] V. Srikant, J. S. Speck, and D. R. Clarke, "Mosaic structure in epitaxial thin films having large lattice mismatch," *Journal of Applied Physics*, 82(9):4286–4295, 1997. `doi:10.1063/1.366235`.

[206] C. Kittel. *Introduction to Solid State Physics*. John, eight edition, 2005.

[207] S. Yang, R. Miyagawa, H. Miyake, K. Hiramatsu, and H. Harima, "Raman scattering spectroscopy of residual stresses in epitaxial AlN films," *Applied Physics Express*, 4(3):031001, 2011. `doi:10.1143/APEX.4.031001`.

[208] A. C. Ferrari, J. C. Meyer, V. Scardaci, C. Casiraghi, M. Lazzeri, F. Mauri, S. Piscanec, D. Jiang, K. S. Novoselov, S. Roth, and A. K. Geim, "Raman spectrum of graphene and graphene layers," *Physical Review Letters*, 97:187401, 2006. `doi:10.1103/PhysRevLett.97.187401`.

[209] S. S. Cohen, "Contact resistance and methods for its determination," *Thin Solid Films*, 104(3–4):361–379, 1983. `doi:10.1016/0040-6090(83)90577-1`.

[210] G. S. Marlow and M. B. Das, "The effects of contact size and non-zero metal resistance on the determination of specific contact resistance," *Solid-State Electronics*, 25(2):91 – 94, 1982. `doi:10.1016/0038-1101(82)90036-3`.

[211] N. C. Chen, C. Y. Tseng, A. P. Chiu, C. F. Shih, and P. H. Chang, "Application of modified transmission line model to measure p-type GaN contact," *Applied Physics Letters*, 85(25):6086–6088, 2004. `doi:10.1063/1.1835993`.

[212] Y. Wang, W. Chen, Q. Wei, W. Chen, R. Li, Y. Pan, Z. Yang, G. Zhang, and X. Hu, "Modified transmission line model to investigate non-ohmic contact behavior and its application on GaN," *Journal of Applied Physics*, 101(8):086105, 2007. `doi:10.1063/1.2717142`.

[213] R. Piotrzkowski, E. Litwin-Staszewska, and S. Grzanka, "Towards proper characterization of nonlinear metal-semiconductor contacts. generalization of the transmission line method," *Applied Physics Letters*, 99(5):052101, 2011. `doi:10.1063/1.3619813`.

[214] J. Strong. *Procedures in Experimental Physics*. Prentice-Hall, New York, first edition, 1938.

[215] J. C. Zwinkels, M. Noël, and C. X. Dodd, "Procedures and standards for accurate spectrophotometric measurements of specular reflectance," *Applied Optics*, 33(34):7933–7944, 1994. `doi:10.1364/AO.33.007933`.

[216] J. M. Herbelin, J. A. McKay, M. A. Kwok, R. H. Ueunten, D. S. Urevig, D. J. Spencer, and D. J. Benard, "Sensitive measurement of photon lifetime and true reflectances in an optical cavity by a phase-shift method," *Applied Optics*, 19(1):144–147, 1980. `doi:10.1364/AO.19.000144`.

[217] S. Mogg, N. Chitica, G. Plaine, and M. Hammar, "Absolute reflectance measurements by a modified cavity phase-shift method," *Review of Scientific Instruments*, 73(4):1697–1701, 2002. `doi:10.1063/1.1461872`.

[218] L. C. West and S. J. Eglash, "First observation of an extremely large-dipole infrared transition within the conduction band of a GaAs quantum well," *Applied Physics Letters*, 46(12):1156–1158, 1985. `doi:10.1063/1.95742`.

[219] B. F. Levine, R. J. Malik, J. Walker, K. K. Choi, C. G. Bethea, D. A. Kleinman, and J. M. Vandenberg, "Strong 8.2 μm infrared intersubband absorption in doped GaAs/AlAs quantum well waveguides," *Applied Physics Letters*, 50(5):273–275, 1987. `doi:10.1063/1.98223`.

[220] B. E. A. Saleh and M. C. Teich. *Fundamentals of Photonics*. John Wiley & Sons, Inc., second edition, 2007.

[221] T. Nagashima, Y. Kubota, T. Kinoshita, Y. Kumagai, J. Xie, R. Collazo, H. Murakami, H. Okamoto, A. Koukitu, and Z. Sitar, "Structural and optical properties of carbon-doped AlN substrates grown by hydride vapor phase epitaxy using AlN substrates prepared by physical vapor transport," *Applied Physics Express*, 5(12):125501, 2012. `doi:10.1143/APEX.5.125501`.

[222] P. Kozodoy, Y. P. Smorchkova, M. Hansen, H. Xing, S. P. DenBaars, U. K. Mishra, A. W. Saxler, R. Perrin, and W. C. Mitchel, "Polarization-enhanced Mg doping of AlGaN/GaN superlattices," *Applied Physics Letters*, 75(16):2444–2446, 1999. `doi:10.1063/1.125042`.

[223] J. Simon, V. Protasenko, C. Lian, H. Xing, and D. Jena, "Polarization-induced hole doping in wide-band-gap uniaxial semiconductor heterostructures," *Science*, 327(5961):60–64, 2010. `doi:10.1126/science.1183226`.

[224] S. Li, T. Zhang, J. Wu, Y. Yang, Z. Wang, Z. Wu, Z. Chen, and Y. Jiang, "Polarization induced hole doping in graded $Al_xGa_{1-x}N$ ($x = 0.7 \sim 1$) layer grown by molecular beam epitaxy," *Applied Physics Letters*, 102(6):062108, 2013. `doi:10.1063/1.4792685`.

[225] S. Krishnamoorthy, D. N. Nath, F. Akyol, P. S. Park, M. Esposto, and S. Rajan, "Polarization-engineered GaN/InGaN/GaN tunnel diodes," *Applied Physics Letters*, 97(20):203502, 2010. `doi:10.1063/1.3517481`.

[226] Y. Taniyasu, J.-F. Carlin, A. Castiglia, R. Butté, and N. Grandjean, "Mg doping for p-type AlInN lattice-matched to GaN," *Applied Physics Letters*, 101(8), 2012. `doi:10.1063/1.4747524`.

[227] L. Nevou, M. Tchernycheva, F. H. Julien, F. Guillot, and E. Monroy, "Short wavelength ($\lambda = 2.13$ μm) intersubband luminescence from GaN/AlN quantum wells at room temperature," *Applied Physics Letters*, 90(12):121106, 2007. `doi:10.1063/1.2715001`.

[228] L. Nevou, F. H. Julien, M. Tchernycheva, F. Guillot, E. Sarigiannidou, and E. Monroy, "Near-infrared intersubband emission from GaN/AlN quantum dots and quantum wells," *Physica Status Solidi (c)*, 5(6):2120–2122, 2008.

[229] K. Driscoll, Y. Liao, A. Bhattacharyya, L. Zhou, D. J. Smith, T. D. Moustakas, and R. Paiella, "Optically pumped intersubband emission of short-wave infrared radiation with GaN/AlN quantum wells," *Applied Physics Letters*, 94(8):081120, 2009. `doi:10.1063/1.3089840`.

[230] A. Ishida, K. Matsue, Y. Inoue, H. Fujiyasu, H.-J. Ko, A. Setiawan, J.-J. Kim, H. Makino, and T. Yao, "Design and preparation of AlN/GaN quantum wells for quantum cascade laser applications," *Japanese Journal of Applied Physics*, 44(8):5918–5922, 2005. `doi:10.1143/JJAP.44.5918`.

[231] M. Yamanishi, T. Edamura, K. Fujita, N. Akikusa, and H. Kan, "Theory of the intrinsic linewidth of quantum-cascade lasers: Hidden reason for the narrow linewidth and line-broadening by thermal photons," *Quantum Electronics, IEEE Journal of*, 44(1):12–29, 2008. `doi:10.1109/JQE.2007.907563`.

Papers I–V